Characterization and Simulation of AA7075 Hot Stamping With Subsequent Die Quenching for Automotive Structural Applications

by

Benoit THÉRIAULT

THESIS PRESENTED TO ÉCOLE DE TECHNOLOGIE SUPÉRIEURE
IN PARTIAL FULFILLMENT FOR A MASTER'S DEGREE
WITH THESIS IN MECHANICAL ENGINEERING
M.A.Sc.

MONTREAL, NOVEMBER 23RD, 2018

ÉCOLE DE TECHNOLOGIE SUPÉRIEURE
UNIVERSITÉ DU QUÉBEC

BOARD OF EXAMINERS

THIS THESIS HAS BEEN EVALUATED

BY THE FOLLOWING BOARD OF EXAMINERS:

Mr. Tan Pham, Memorandum Supervisor
Department of Génie mécanique at École de technologie supérieure

Mr. Guillaume D'Amours, Co-supervisor
Aluminium Technology Center, National Research Council Canada

Mr. Van Ngan Lê, President of the Board of Examiners
Department of Génie mécanique at École de technologie supérieure

Mr. Vincent Demers, Member of the jury
Department of Génie mécanique at École de technologie supérieure

THIS THESIS WAS PRESENTED AND DEFENDED

IN THE PRESENCE OF A BOARD OF EXAMINERS AND THE PUBLIC

ON SEPTEMBER 21ST, 2018

AT ÉCOLE DE TECHNOLOGIE SUPÉRIEURE

ACKNOWLEDGEMENTS

I would first like to thank my supervisor, Professor Tan Pham for his help throughout this project. You have provided me with the opportunity to rely on your expertise and had enough confidence to let me learn at my pace. Your scientific rigour have inspired me to give my best throughout this project.

This project wouldn't have been possible without the involvement of my co-supervisor, Mr. Guillaume D'Amours. Your continuous availability despite your immense work load is something I will always remember. Your in-depth knowledge has been a constant source of both awe and motivation for self-improvement.

I would also extend my thanks to the team at the Aluminium Technology Center, who have built a solid community proud of its scientific achievements and its very enjoyable company culture. Thank you especially Alexandre Gariépy for your help. Your professionalism and scientific curiosity have been a hallmark of my time spent here. Thank you also to Alexandre Morin and Myriam Poliquin for providing your assistance, technical knowledge and patience during the test campaigns.

Thank you to my parents, Hélène and Richard, who have always supported me. You have encouraged the values of curiosity, openness and work ethics which has lend me to the path I am on now.

Finally, thank you my dear Lysa for your support through thick and thin. I would not be the person I am today without you.

CARACTÉRISATION ET SIMULATION PAR ÉLÉMENTS FINIS DE L'ESTAMPAGE À CHAUD D'ALUMINIUM AA7075 AVEC TREMPE PAR MATRICE

Benoit THÉRIAULT

RÉSUMÉ

Il est nécessaire de pouvoir modéliser précisément le procédé d'estampage à chaud afin d'obtenir des pièces structurales d'automobile qui sont à la fois plus légères pour réduire leur impact environnemental et améliorer la sécurité des passagers en cas de collisions. Pour satisfaire à de nouvelles normes environnementales, certains manufacturiers automobiles ont jugé nécessaire de laisser de côté les alliages d'acier à haute résistance au profit d'alliages d'aluminium.

L'utilisation d'alliages d'aluminium pouvant être durcis par vieillissement présente à la fois de nouvelles opportunités et de nouveaux défis. Malgré qu'une réduction de poids de 20% soit envisagée par le programme de recherche finançant ce projet, la fenêtre de paramètres est beaucoup plus étroite qu'avec des alliages d'acier.

Ce projet a comme objectif de mieux comprendre le procédé d'estampage à chaud avec trempe par matrices de l'aluminium AA7075. Cela devrait permettre de développer une première itération d'outillage nécessaire au procédé. L'envergure du projet est limitée au comportement mécanique en général en n'incluant pas de modèle d'endommagement, qui serait nécessaire pour assurer le succès du formage pour un ensemble de paramètres donnés. Dans ce travail, il a été nécessaire de caractériser le matériau utilisé et d'autre paramètres importants tels que le coefficient de transfert de chaleur aux interfaces des matrices. Cela est accompli en utilisant des modèles et lois de matériaux existant et un logiciel commercial d'analyse par éléments finis, avec l'objectif de pouvoir exporter les données dans un format pouvant être utilisé par des concepteurs.

Une première itération de l'outillage fut disponible avant la fin du projet, permettant une comparaison entre le modèle numérique et des résultats expérimentaux. Suivant cela, il a été possible de mieux comprendre les mécanismes d'insuccès et suggérer des améliorations au procédé. Ces améliorations ont permis de confirmer la viabilité de l'estampage à chaud et la trempe du AA7075.

Mots clés: Estampage à chaud, aluminium, AA7075, caractérisation, trempe par matrices, analyse par éléments finis

CHARACTERIZATION AND SIMULATION OF AA7075 HOT STAMPING WITH SUBSEQUENT DIE QUENCHING FOR AUTOMOTIVE STRUCTURAL APPLICATIONS

Benoit THÉRIAULT

ABSTRACT

Accurate modelling of the hot stamping forming process is necessary to achieve automotive structural parts that are both lighter for a lower environmental impact and safer in case of collisions. To comply with new environmental norms, some car manufacturers are attempting to replace high strength steel by high grade aluminium.

The use of age hardenable aluminium alloys such as AA7075 present both new opportunities and challenges. Although a weight reduction of 20% is expected by this research program, the forming parameters window for parts made of aluminium alloys is much narrower than for their steel counterparts.

The objective of this project is to better understand the process of hot stamping and quenching of AA7075. This, in turn, should allow a first iteration of tooling to be developed for the process. The scope of this work is limited to the general mechanical behaviour and does not include a damage model, which would be required to ensure the process' success with a given set of parameters. In this work, it was found necessary to characterize the material used and other important process parameters such as interfacial heat transfer coefficients. This is done with material laws and models available in commercial finite element software, with the goal of being able to export the required data into a usable package for designers.

An experimental tooling set was available before the end of this project, enabling a comparison of the numerical model with experimental results. Following this, it was possible to acquire a new understanding of the current failure modes and suggest improvements to the process. These improvements have confirmed the viability of the hot stamping and quenching with AA7075.

Keywords: Hot stamping, aluminium, AA7075, characterization, die quenching, finite element analysis

TABLE OF CONTENTS

LIST OF TABLES

Page

LIST OF FIGURES

LIST OF ABREVIATIONS

AOI	Area Of Interest
BS	Battery support
CAFE	Corporate Average Fuel Economy (standard)
DIC	Digital Image Correlation
ECT	Eddy current testing
ETS	École de Technologie Supérieure
FEA	Finite Element Analysis
FLD	Forming Limit Diagram
GP	Guinier-Preston (zone)
NRC	National Research Council Canada
SHT	Solution Heat Treatment
VH	Vickers Hardness

LIST OF SYMBOLS AND UNITS OF MEASUREMENTS

Symbols	
σ_{xx}, σ_{yy}, σ_{zz}	Stress in the laminating, transverse and normal direction
σ_{11}, σ_{22}, σ_{33}	First, second and third principal stress
$\dot{\sigma}$	Stress rate
ε^E	Elastic strain
ε^P	Plastic strain
$\dot{\varepsilon}^E$	Elastic strain rate
$\dot{\varepsilon}^P$	Plastic strain rate
ε_{xx}, ε_{yy}, ε_{zz}	Strain in the laminating, transverse and normal directions
η'', η', η	Precipitates in AA7075
σ_Y	Yield stress
f	Yield function
K_1, K_2, M	Barlat 89 yield formula parameters
a, c, h, p	Barlat 89 yield formula characterization parameters
F, G, H, L, M, N	Hill 90 yield formula parameters
Γ, Ψ	Stress tensor invariants
R_θ	Anisotropy coefficient at θ degrees from the laminating direction
$\dot{q}$	Heat flux
t	Time

σ	Stefan-Boltzmann constant
F_v	View factor
A	Area
τ	Time constant
k	Linear thermal conductivity

Units of measurements

K	Kelvin
$^{\circ}C$	Degree Celcius
$^{\circ}$	Degree
m	Meter
Pa	Pascal
J	Joule
s	Second
N	Newton
W	Watt
S	Siemens

INTRODUCTION

Major car manufacturers with activities in America have agreed on the Corporate Average Fuel Economy (CAFE) standards for production models for the period years from 2017 to 2025. These include an objective of 5% annual improvement for passenger car's fuel efficiency. Many areas of research are solicited to reach this goal, including materials science and process design as lightweighting tools.

In this research project, it is expected to show that AA7075 can be adequately hot stamped and quench during the same operation. When this alloy reaches its maximal strength following an adequate thermal heat treatment, it should be possible to replace a boron steel automotive structural component by an aluminium one that is 20% lighter.

The alloy used in the current project (AA7075) is expected to reach a yield stress of 425 MPa with adequate solution heat treatment (SHT), quenching and age hardening. To reduce production time and complexity, the hot stamping process studied here relies on the dies to perform the necessary quench during the stamping operation and in the few seconds after when the part is still held inside the dies. This also allows the part to be formed at high temperature and strain rates, both ideal conditions for maximum formability. At room temperature, the maximum strains are between 10% and 15%, while at an elevated temperature strains over 100% are obtained. Currently, the only parts made of aluminium on cars are used for closure applications (exterior body panels) while most of the body-in-white is comprised of steel parts.

To achieve a high degree of accuracy in the simulation of this forming process, many material properties are required but cannot be found in the available literature. Therefore, multiple types of test campaigns will be done to acquire the required information on the material. The most important are the hardening properties as a function of temperature and strain rate, as well as the interfacial heat transfer coefficients. R values are used to describe the material anisotropy in sheet metal and they will also be obtained during the tests.

Chapter 1 will present the current knowledge on aluminium hot stamping, covering different aspects such as metallurgy, constitutive laws and finite element analysis.

Chapter 2 covers the methodology used for the characterization and simulation of the hot stamping process.

Chapter 3 presents the results from the characterization and from the simulation of the whole process.

Finally, Chapter 4 contains some suggestions on improvements to the tooling and process for industrial applications based on the finite element analysis results.

CHAPTER 1

LITERATURE REVIEW

1.1 The Hot Stamping Process

This review of the literature aims to provide the general knowledge necessary for the understanding of the hot stamping process and its simulation.

The process begins with the cutting of the raw material in a shape that is optimized for the later steps. Generally, there is some excess material to allow for material flow as the blank is stretched. Next, the blank is heated to a temperature that allows for maximum formability. The blank is then transferred to the dies and the stamping occurs at a controlled speed. Depending on the process design, the part may be fully cooled inside the dies, adding a simultaneous quench. As illustrated in Figure 1.1, subsequent process operations are done to obtain a functional part.

Figure 1.1 Main steps of the hot stamping process (Futaba Industrial, 2016)

Due to its high initial tooling costs, hot stamping is especially suitable for large production series, as shown by its uses in the automotive industry. This is further evidenced by the production going from 3 million parts per year in 1987 to 107 million parts per year in 2007 (Aspacher, 2008).

Tests carried out on 5XXX aluminium alloy found a ductility peak at strain rates between $10^{-1}s^{-1}$ and $1s^{-1}$ (Bariani *et al.*, 2013) while boron steel's strain rate during forming is increased up to 960 s^{-1}, in order to improve final properties (Bardelcik *et al.*, 2010). Despite this smaller

possible strain rate window, aluminium alloys offer some advantages over steel alloys for automotive structural parts such as lower working temperature which helps with process control, cooling and tooling life. The same part strength is also obtained with a much lower material yield stress, enabling easier part trimming and other finishing operations.

This project focuses on automotive structural parts, of which none are currently made of aluminium. Currently, the only contenders to replace high strength steel are high grade aluminium alloys such as AA7XXX and, in a lesser measure, AA6XXX.

1.2 Material Behavior

1.2.1 Yield Criteria

Mises (1928) developed the first yield criterion in the form of a quadratic function. It requires 21 coefficients for a fully anisotropic material but could be reduced to six in the case of an orthotropic material, as is commonly seen in metals. Such a generalization was proposed by Hill in 1948 as follows:

$$\begin{aligned} 2f(\sigma_{ij}) \equiv & F(\sigma_{22}-\sigma_{33})^2 + G(\sigma_{33}-\sigma_{11})^2 + H(\sigma_{11}-\sigma_{22})^2 + \\ & 2L\sigma_{23}^2 + 2M\sigma_{31}^2 + 2N\sigma_{12}^2 = 1 \end{aligned} \tag{1.1}$$

where f is the yield function and F, G, H, L, M and N are constants dependent upon the material. This formulation however cannot always accurately represent the yield behavior of aluminium alloys (Pearce, 1968) (Woodthorpe & Pearce, 1970). Despite these limitations, it has been used frequently due to the fact that it requires only four parameters for plane stress conditions, as often assumed in sheet forming.

Hill's model was iteratively improved by Hill (1979), Hill (1993) and finally by Chu (1995) to make it possible to represent the behaviours that were previously outside the bounds of the model. It uses the yield stresses in the laminating, transverse and equibiaxial directions (σ_0,

σ_{90}, σ_b), the applied stress (σ_1 and σ_2) and material parameters(p, q and c). For sheet metal represented by shell elements, the resulting function is:

$$\sigma_u^2 = \frac{\sigma_1^2}{\sigma_0^2} - \frac{c\sigma_1\sigma_2}{\sigma_0\sigma_{90}}\sigma_1\sigma_2 + \frac{\sigma_2^2}{\sigma_{90}^2} + \left\{(p+q) - \frac{(p\sigma_1 + q\sigma_2)}{\sigma_b}\right\}\frac{\sigma_1\sigma_2}{\sigma_0\sigma_{90}} \tag{1.2}$$

where:

$$\frac{c}{\sigma_0\sigma_{90}} = \frac{1}{\sigma_0^2} + \frac{1}{\sigma_{90}^2} - \frac{1}{\sigma_b^2} \tag{1.3}$$

A first criterion based on crystal plasticity for anisotropic metals was proposed by Hosford (1972). It is defined as:

$$F|\sigma_{22} - \sigma_{33}|^a + G|\sigma_{33} - \sigma_{11}|^a + H|\sigma_{11} - \sigma_{22}|^a = \sigma^a \tag{1.4}$$

It has three classical material parameters and the exponent "a" which is dependent upon the crystalline structure, with a value of 6 for body centered cubic (BCC) material and 8 for face centered cubic (FCC) materials such as aluminium and its alloys.

Using the notions of crystal plasticity, Barlat *et al* (1989) (1991) (2003) proposed many iterations of models designed to be used in hot stamping. These will be discussed in more details in Chapter 2. He notably created the Barlat 89 model and subsequently, an improvement over his previous work with the use of a twice linearly transformed deviatoric stress tensor (Barlat *et al.*, 2003). The criterion then requires 13 coefficients, or 9 in the case of a plane stress case (Banabic, 2000). It was specifically designed for plane stress states in sheet forming and one of the important improvements was an assured convexity of the function.

The rise in computing power brought the possibility of using an approach of brute force optimization for a set of parameters. This is particularly useful when using a polynomial yield criteria such as those presented by Soare *et al.* (2008). With 6th and 8th order functions that have respectively 16 and 25 coefficients, it is possible to represent a wide array of possible behaviors including the strength-differential effect. Although these formulations are very flexible,

they have the possibility of not being convex in the stress space. They also require extensive testing campaigns that may be too long or expensive in many situations.

One possibility for calibrating the parameters of these material models in this application is to use a digital image correlation system to measure the strain in different regions of a more complex stress state such as a cross-die or Nakazima test, as used by Garcia *et al.* (2002) with success.

Another approach to the yield criteria definition is to use polar coordinates to describe the yield surface. An example of this is the Budiansky yield criterion that can be written as:

$$x = \frac{\sigma_1 + \sigma_2}{2\sigma_b} = g(\alpha)\cos\alpha; y \equiv \frac{\sigma_2 - \sigma_1}{2\sigma_s} = g(\alpha)\sin\alpha \tag{1.5}$$

Following a different strategy, Banabic (2000) proposed a variation of the previous model by adding weighting coefficients. The formulation has the following form:

$$\overline{\sigma} = \left[a(b\Gamma + c\Psi)^{2k} + a(b\Gamma - c\Psi)^{2k} + (1-a)(2c\Psi)^{2k}\right]^{\frac{1}{2k}} \tag{1.6}$$

with Γ and Ψ being functions of the invariants of a transformed stress tensor and a, b, c and k being material parameters. Once simplified, there are 8 material parameters with half being dependent on the crystallographic structure.

One last interesting approach to a constitutive model was taken by Mohamed *et al.* (2012) by using Arrhenius rate equations to form a constitutive model representing the continuous damage and recrystallization that occur at different strain rates. The Arrhenius equations are especially well suited since these phenomena are heavily dependent on temperature. This also provides the opportunity of including an internal state variable that includes the loading path instead of only the final strain and temperature, as seen with the FLD. One of the downsides of

the approach is the high number of required material parameters. These 21 constants require a complex methodology for their calibration.

1.2.2 Plasticity Behavior

Many attempts have been made to accurately describe the hardening behaviour of aluminium alloys under high strains. Some of the most common hardening laws for sheet forming are described in Table 1.1. Material laws account for anisotropy in hardening in different manners and the following laws are adapted as necessary.

Table 1.1 Types of hardening (Livermore Software Technology Corporation , LSTC)

Type	Equation
Bilinear	$\sigma_y = k\varepsilon_p$
Exponential	$\sigma_y = k(\varepsilon_0 + \varepsilon_p)^n$
Voce	$\sigma_y = a - be^{-ce}$
Gosh	$\sigma_y = k(\varepsilon_0 + \varepsilon_p)^n - p$

These are only a few examples amongst those generally available in commercial finite element code, although they prove sufficient in many cases. It is also possible to use experimental data points that are then interpolated. It allows a close representation of reality without being too computationally expensive. The main advantage is that the resulting behaviour is very close to the measured data, without any added mathematical transformation.

1.2.3 Friction

Friction between a high purity aluminium rounded tip and a medium carbon steel plate was investigated by Menezes *et al.* (2009). Some of the results are shown in Figure 1.2.

The value of 0.2 of the friction coefficient with random direction polishing is similar to what is commonly used in simulations with good results (Samekto & Roll, 2003), (Sotirov *et al.*,

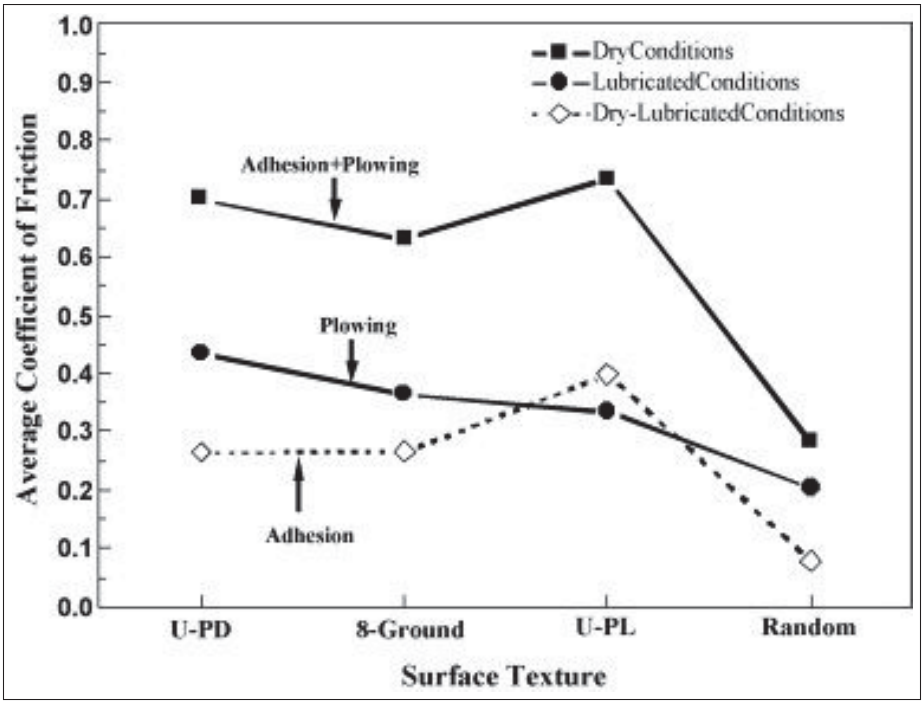

Figure 1.2 Measured coefficients of friction under different conditions, from Menezes *et al.* (2009)

2010). However, multiple experiments done at NRC have shown that a coefficient of 0.08 to 0.12 may accurately represent different process conditions. The coefficient of 0.11 was chosen for best results with the graphite lubricant and the tooling's current general surface finish.

1.3 Material Testing

1.3.1 Uniaxial Tests

The uniaxial tensile test is a very common type of material testing. Due to the nature of the raw material, dog bone shaped specimens are used. These test have the advantage of being simple while also being able to provide information on the anisotropy, which is normally computed with the specimen's dimensions when strained at 20% (Hosford & Caddell, 2011).

Although they were inconclusive for the characterization of the anisotropy, tests using a digital image correlation (DIC) system showed that AA7075 has a serrated pattern of strain evolution

during deformation similar to "type D" as described in (Rodriguez, 1984), which is said to have a "propagation similar to Luders band". However, these effects are small and might not be captured in a macro-scale finite element analysis. This pattern is shown in Figure 1.3.

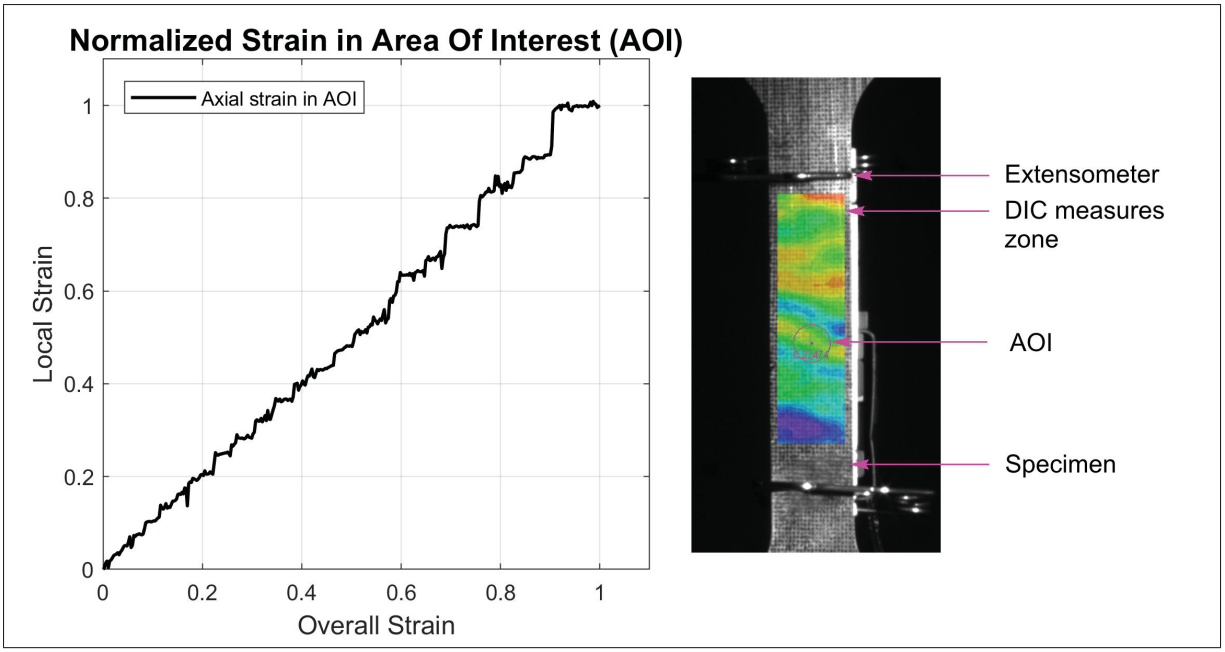

Figure 1.3 Local versus overall strain evolution in a uniaxial AA7075 specimen at a strain rate of $0.1s^{-1}$, at room temperature

1.3.2 Biaxial Tests

The biaxial stress state test is often performed using the Nakajima test setup. Using a blank holder at the circumference as shown in Figure 1.4, the sheet is deformed by a half dome shaped punch.

The forming parameters closely resemble those encountered in industrial hot stamping as they include the friction and possibly the cooling effects of the tools. It is also possible to vary the shape of the blank to obtain different states of stress, allowing for the creation of the forming limit diagram (FLD). Some examples of these shapes are shown in Figure 1.5.

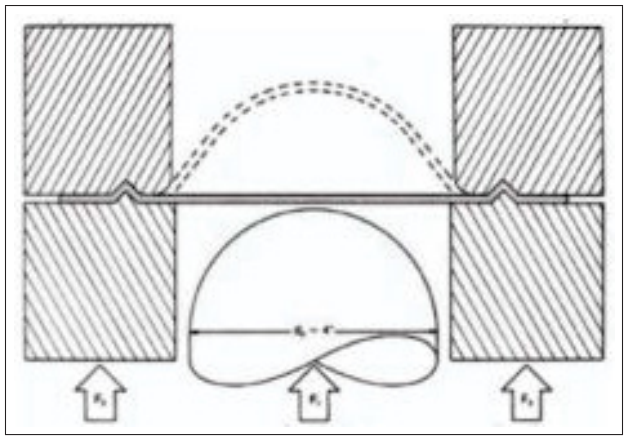

Figure 1.4 Schematic of a Nakazima test setup (Pellegrini, 2011)

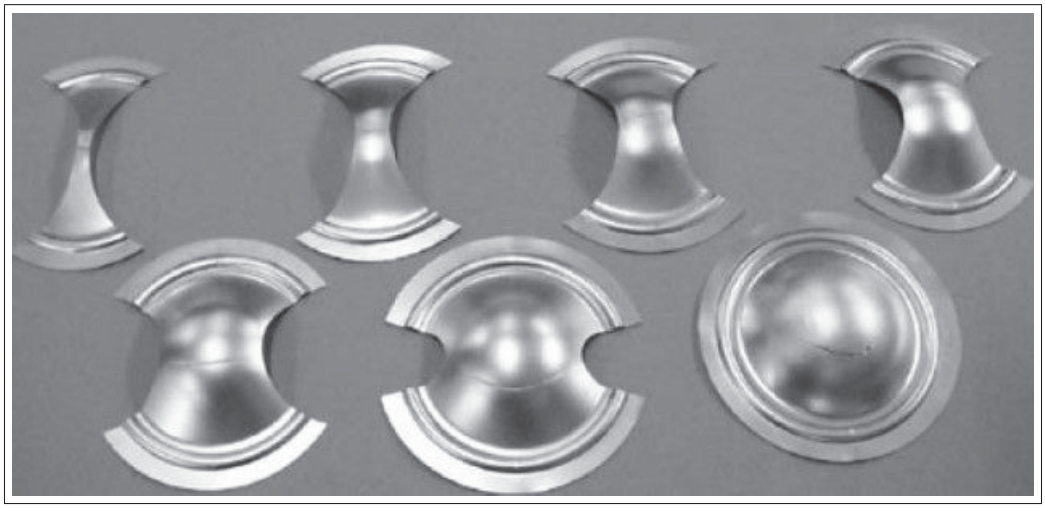

Figure 1.5 Different shapes for Nakazima test (Deformacije, 2016)

The effects of anisotropic behaviors can also be observed in the lower row of specimens in the form of directional necking lines. This anisotropy is usually described with the Lankford coefficients, or R values, which describe the ratio of lateral plastic strain to the normal (through thickness) plastic strain.

Although Nakajima tests are useful for characterization of material, other more-or-less standardized shapes are used for testing the formability of different alloys and calibration of numerical models. For example, the cross-die test is used in the automotive industry (Sotirov

et al., 2010). It uses a setup similar to the Nakajima test but with a plus sign shaped punch with rounded corners. It is useful in that it recreates many loading paths and stress conditions, cooling rates and friction states in the aluminium sheets due to its geometry. It can also be simulated using only a quarter of the shape due to the two plane symmetry.

Also interesting is the use of the cone cup test shown in Figure 1.6, which is generally used for characterization of materials in superplastic forming. An advantage of the cone cup method is the possibility of having a deformation that occurs without any friction with the tooling, thus showing a simpler stress state devoid of friction.

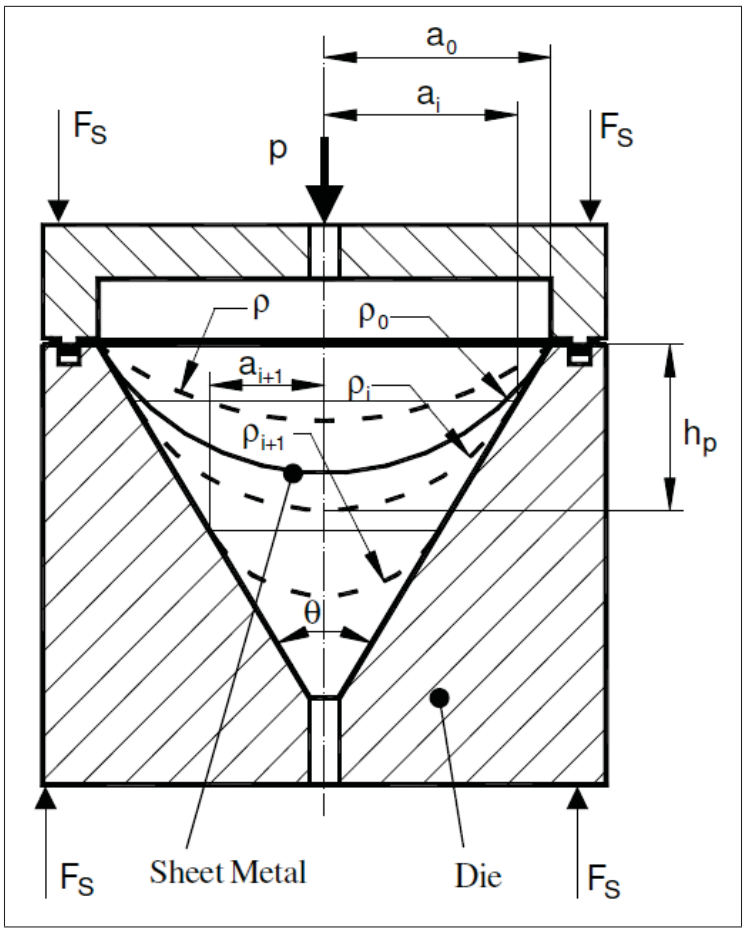

Figure 1.6 Cone cup test rig (Banabic *et al.*, 2005)

As found in (Barlat *et al.*, 2003), Nakajima tests for which the lubrication was insufficient or random yielded unusable data. In the cone cup method it is possible to consider the initial strain as contactless and, when contact is reached between the blank and the dies to consider the material as locked in place by static friction (Samekto & Roll, 2003), enabling a simpler analysis or inverse modelling.

1.3.3 Failure Criteria

A forming limit diagram (FLD) is often used as the mean of predicting the maximum acceptable forming strains according to the minor and major plane strains ratios and amplitude. Such limits are determined with the goal of never reaching failure or internal damage even with the normal variability of the process. An example of FLD for AA5083 is given for a wide range of temperatures, as shown in Figure 1.7.

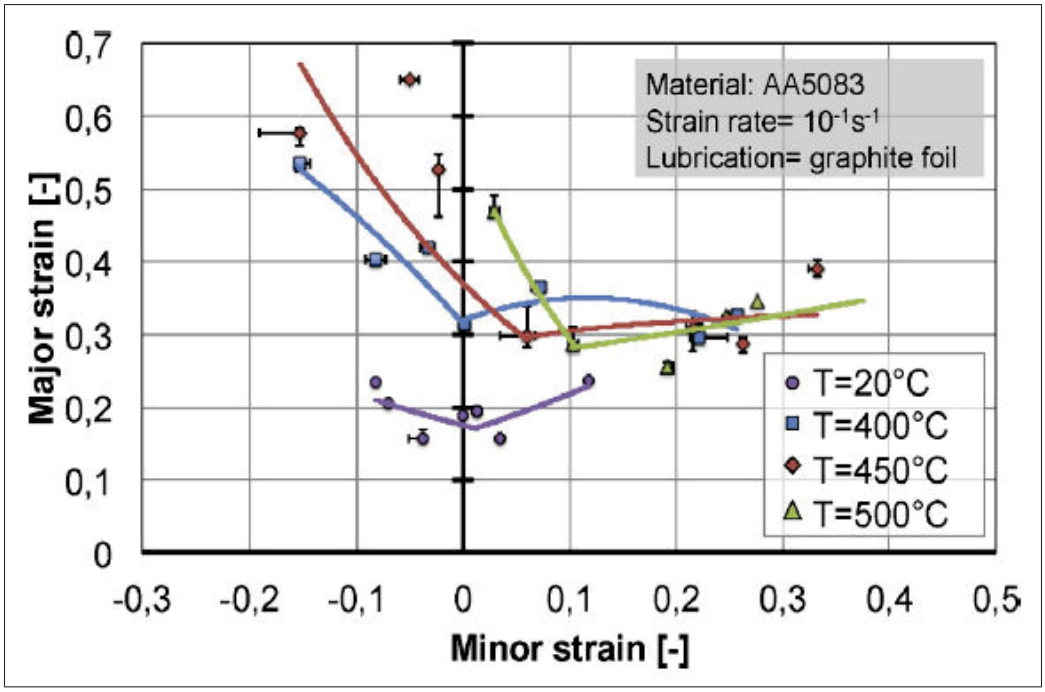

Figure 1.7 Forming limit curves at different temperatures (Bariani *et al.*, 2013)

One of the limitations of a FLD is the impossibility of taking into account the strain path where, for example, damage may begin to occur before reaching a steady temperature. Mohamed *et al.* (2012) proposed a constitutive law that includes an internal variable as a damage criterion. The system used is a combination of Arrhenius rate equations and the damage mechanism. The void nucleation and growth constitute the forward reaction and the recrystallisation is the backward reaction, with rates being dependent on temperature.

The mechanical properties also greatly much within the temperatures at which the forming is done, as seen in Figure 1.8 where the yield stress of AA5083 is a function of temperature. It is possible to see that the scaling of the properties are different from the Material Properties Database software (MPDB) and the MatWeb database. This is due in part by the fact that MPDB's data were made using machined round specimens while Matweb's data were obtained from laminated sheet, with possibly a slightly different composition of AA7075 and with different sources. The higher strength in the -O state can be explained by work hardening of the sheets while the lower properties in the hardened state may be explained by suboptimal quench and ageing in the core of the round specimen.

The current state of the art in damage modelling for hot stamping are cumulative models based on strain history in each directions. Onset of instability is also used as a criterion, as in (Elfakir, 2015). In his thesis, a fully decoupled model was used in parallel to the FEA to evaluate necking risk at key locations, allowing for a computationally inexpensive implementation.

1.4 Metallurgy of Al-Zn Alloys

1.4.1 AA7075 Alloy Composition

AA7075 is one of the few aluminium alloys that has a strength to weight ratio comparable to the current high strength steel used by the automotive industry. Its chemical composition was retrieved in the MatWeb (2016) and is shown in Table 1.2.

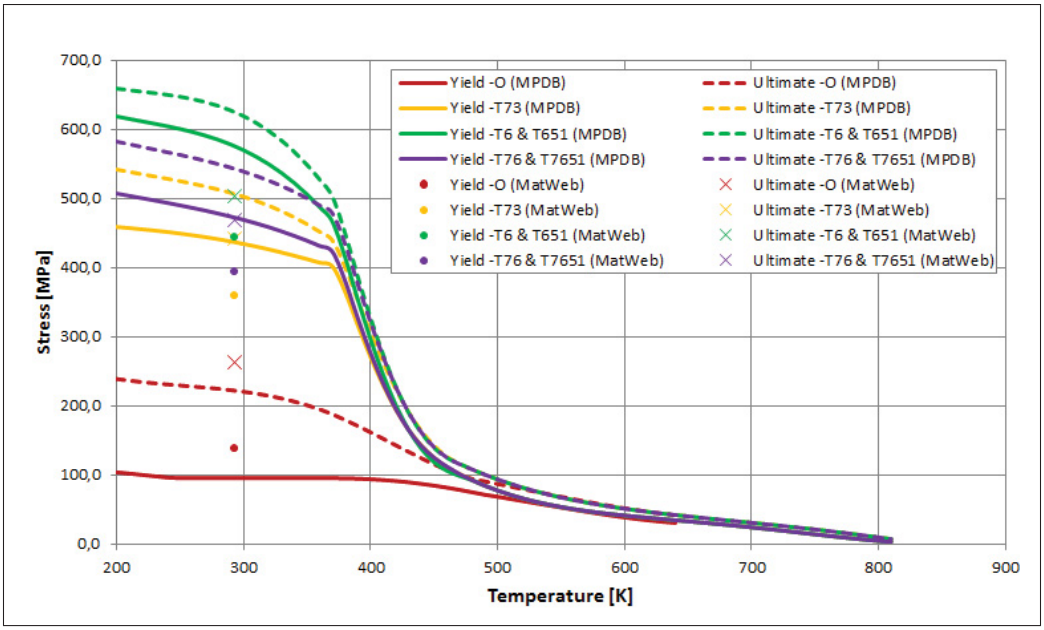

Figure 1.8 Yield and ultimate stresses of AA7075 at different heat treatment stages and temperature, from MPDB (1999) and MatWeb (2016)

Table 1.2 AA7075 composition (MatWeb, 2016)

Element	Concentration	Element	Concentration
Al	87.1 - 91.4 %	Fe	<= 0.50 %
Zn	5.1 - 6.1 %	Si	<= 0.40 %
Mg	2.1 - 2.9 %	Mn	<= 0.30 %
Cu	1.2 - 2.0 %	Ti	<= 0.20 %
Cr	0.2 - 0.3 %	Other	<= 0.15 %

1.4.2 Microstructure

Strain hardening of aluminium begins with the formation of Guinier-Preston (GP) zones, which are high in solutes from the alloying elements, as shown in Figure 1.9.

As the name implies, the solution heat treatment causes the alloying elements to dissolve and creates a homogenous alpha phase. During quenching, a supersaturated solid solution is formed, enabling the formation of GP zones. When ageing is done, the η'' phases then begin to form and changes to η', which has a significant impact on the hardening. However, the

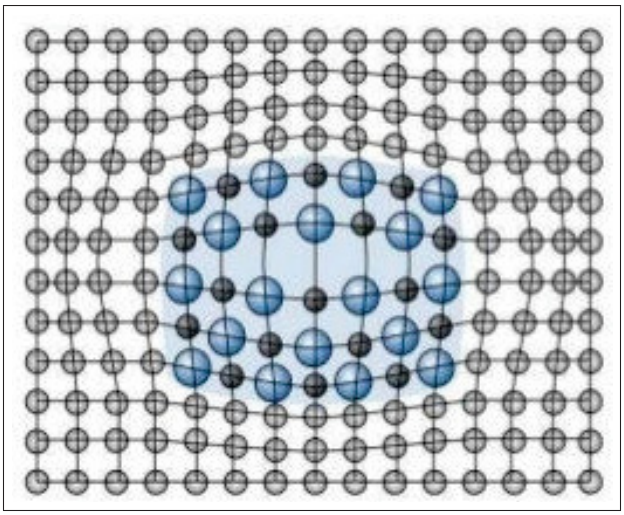

Figure 1.9 Guinier-Preston zone
(Callister *et al.*, 2007)

η' phases are only metastable and will eventually form η phases. These last phases do not have a significant impact on the mechanical properties and are fully stable, allowing them to live long and prosper in the aluminium matrix. The ideal treatment for maximum strength of the alloy is therefore a solution heat treatment followed by a quench and appropriate ageing. The changes in ageing time at $150°C$ and the resulting hardness is heavily dependent on the alloying elements that are present, as shown in Figure 1.10.

Due to the different possibilities of interactions between the different alloying elements, other precipitates may be found in AA7075. The T phase ($Mg_3Zn_3Al_2$ or $Mg_{32}((Zn,Al)_{49})$ (Watanabe *et al.*, 2015) and S phase (Al_2CuMg) (Lim *et al.*, 2003) were identified.

1.4.3 Phase Diagrams

Figure 1.11 shows the phase diagram of aluminium and zinc while Figure 1.12 shows the phase diagram for the two main alloying elements of AA7075, namely zinc and magnesium. The presence of these alloying elements prevents the material from being heated above 500 $°C$ without irreversible damage on its surface thought to be due to liquefaction of zinc and possibily a Mg-Zn binary system.

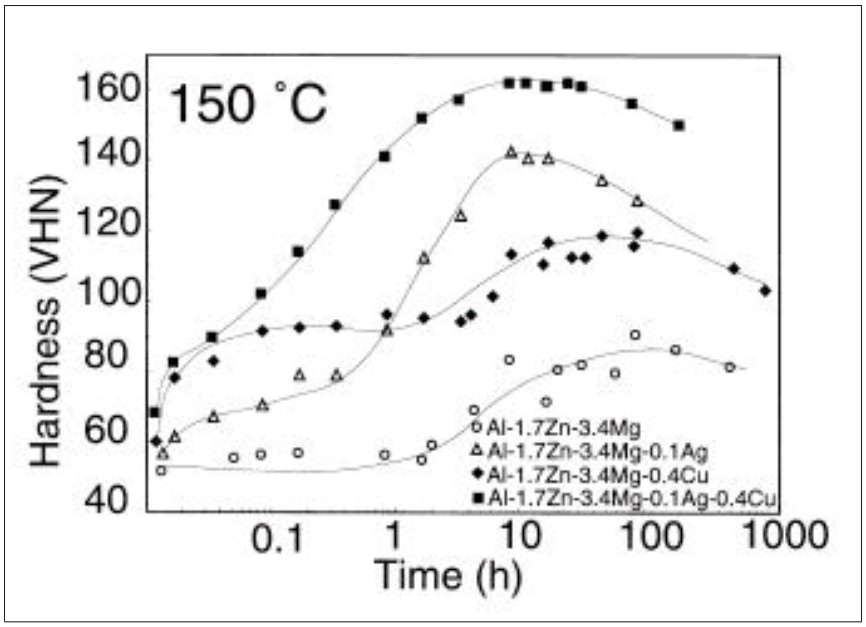

Figure 1.10 Hardening curves of different Al alloys
(Caraher *et al.*, 1998)

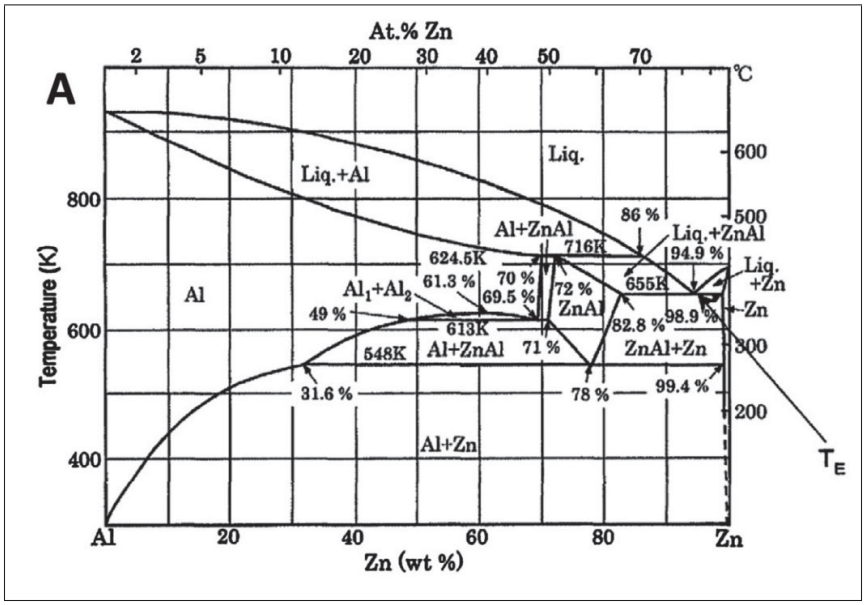

Figure 1.11 Phase diagram of Aluminium and Zinc
(Miyamoto K, 2011)

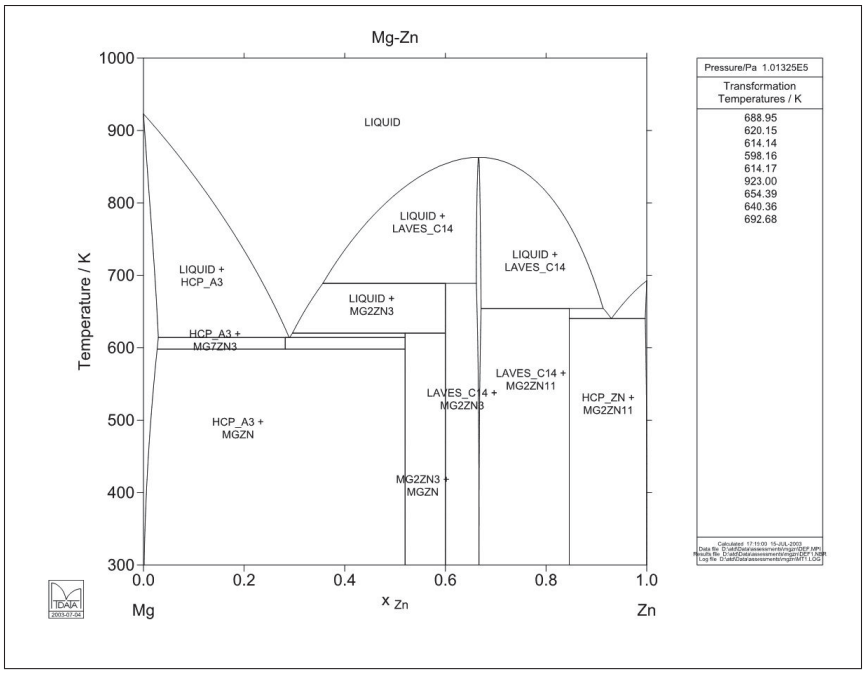

Figure 1.12 Phase diagram of Magnesium and Zinc (National Physical Laboratory, 2010).

1.4.4 Other considerations

Tests on microstructure during compressive deformation by Gourdet & Montheillet (2000) were carried at temperatures between $333°C$ and $380°C$. As stated in the experimental procedure, graphite was used to lubricate the surfaces of the specimens. The friction was still present and caused strain inhomogeneities in the specimen. To compensate, a mechanical model was used to compute the local strains.

There was confirmation of the augmentation of subgrain misorientation with increasing strain. The newly formed high boundary angle causes a diminution of the matter density due to the lattice's discontinuities, which in turn becomes the void nucleation and growth that is the observed damage mechanism in specimens by Mohamed *et al.* (2012). However, these observations should be further analysed since the deformation mode was different for the two compared articles. In (Mohamed *et al.*, 2012), the loading was biaxial while in (Gourdet & Montheillet, 2000), the loading was uniaxial compression.

CHAPTER 2

METHODOLOGY

2.1 Strain and Strain Rate Effects

The main driving factors in the formability of aluminium in hot stamping are the temperature, strain rate and anisotropy. Only the material models including these three parameters are considered for the current project. Although more recent and precise formulations are available, limitations in time and characterization equipment have helped narrow down the possible models to the Barlat 89 (Barlat & Lian, 1989) and the Hill 90 (Hill, 1990) model. In the commercial FEA software used, these models require only the definition of strain hardening data tables and the anisotropy coefficients of the material. However, to ensure the characterization process is reliable, it is necessary to go through the steps for at least one combination of parameters. This also allows for a more in-depth analysis of what the use of each model entails.

The general formulation for the Barlat 89 model, described in (Barlat & Lian, 1989) is:

$$\phi = a|K_1 + K_2|^M + a|K_1 - K_2|^M + c|2K_2|^M = 0 \tag{2.1}$$

where:

$$K_1 = \frac{\sigma_{xx} + h\sigma_{yy}}{2} \quad and \quad K_2 = \sqrt{\left(\frac{\sigma_{xx} - h\sigma_{yy}}{2}\right)^2 + p^2\sigma_{xy}^2} \tag{2.2}$$

The material parameters $a,\ c,\ h$ and p may be defined from the yield stresses at 0°, 45° and 90° from the laminating direction or from the R values. The current approach will use the R values at the laminating direction (R_0) and at the transverse direction (R_{90}) since these are the same ones used in the simulation solver deck later on. They also result in a higher strain anisotropy. The values of $a,\ c$ and h are calculated with the equations:

$$a = 2 - c = 2 - 2\sqrt{\frac{R_0}{1+R_0}\frac{R_{90}}{1+R_{90}}} \quad and \quad h = \sqrt{\frac{R_0}{1+R_0}\frac{1+R_{90}}{R_{90}}} \tag{2.3}$$

In this case of uniaxial stress, it is possible to simplify K_1 and K_2 to:

$$K_1 = K_2 = \frac{\sigma_{xx}}{2} \tag{2.4}$$

Also, due to the definition of a and c, we obtain:

$$\phi = 2\sigma_{xx}^M - 2\sigma_Y^M \tag{2.5}$$

Therefore, in a uniaxial tensile test:

$$\phi = \sigma_Y \tag{2.6}$$

The Hill 90 model (Hill, 1990) was designed for the same use cases as the Barlat 89 model, i.e. anisotropic sheet metal. The formulation is:

$$\phi = K_1^M + K_3 K_2^{(M/2)-1} + c^M K_4^{M/2} = (1 + c^M - 2a + b)\sigma_Y^M = 0 \tag{2.7}$$

where:

$$K_1 = |\sigma_{xx} + \sigma_{yy}| \tag{2.8}$$

$$K_2 = |\sigma_{xx}^2 + \sigma_{yy}^2 + 2\sigma_{xy}^2| \tag{2.9}$$

$$K_3 = -2a\left(\sigma_{xx}^2 - \sigma_{yy}^2\right) + b(\sigma_{xx} - \sigma_{yy})^2 \tag{2.10}$$

$$K_4 = |(\sigma_{xx} - \sigma_{yy})^2 + 4\sigma_{xy}^2| \tag{2.11}$$

The three coefficients found in the above equations are defined as:

$$1+2R_0 = \frac{c^M - a + ((M+2)/2M)b}{1-a+((M-2)/2M)b} \tag{2.12}$$

$$1+2R_{45} = c^M \tag{2.13}$$

$$1+2R_{90} = \frac{c^M + a + ((M+2)/2M)b}{1+a+((M-2)/2M)b} \tag{2.14}$$

For many of the physical properties of 2 mm laminated sheets of AA7075 evaluated hereafter, the most straightforward method is the uniaxial tensile test. To accurately recreate the microstructural state in which the hot stamping is performed, it is necessary to begin with a solution heat treatment of the sample. However, the cooling of the specimen from the solution heat treatment temperature ($490°C$) cannot be done fast enough to accommodate the extensive test campaign to characterize the material at all temperatures and strain rates required.

The proposed strategy is to heat the specimens at the solution heat treatment temperature beforehand in a separate oven. The duration of this step is 18 minutes, identified as the minimum time required for the current T6 temper to achieve the temperature long enough for the dispersion of alloying elements to occur. Specimens are then quenched, thus preventing most of the formation of precipitates from the elements dissolved in the alumnium matrix for the duration necessary to perform the test. They are then transferred to a climatic chamber (Figure 2.1) around the traction apparatus and heated to within $3°C$ of the nominal test temperature. All traction specimens mentioned in this section have been submitted to these steps.

Hardening behaviour was defined with a campaign of uniaxial tests at different combinations strain rates and temperatures, as shown in Table 2.1. Additional tests were made for the R values.

Each parameter set was tested with 3 specimens to ensure repeatability and the average of the resulting loading curves were used. The following procedure is used for each specimen:

1. Place the sample in the convection oven for 18 minutes;

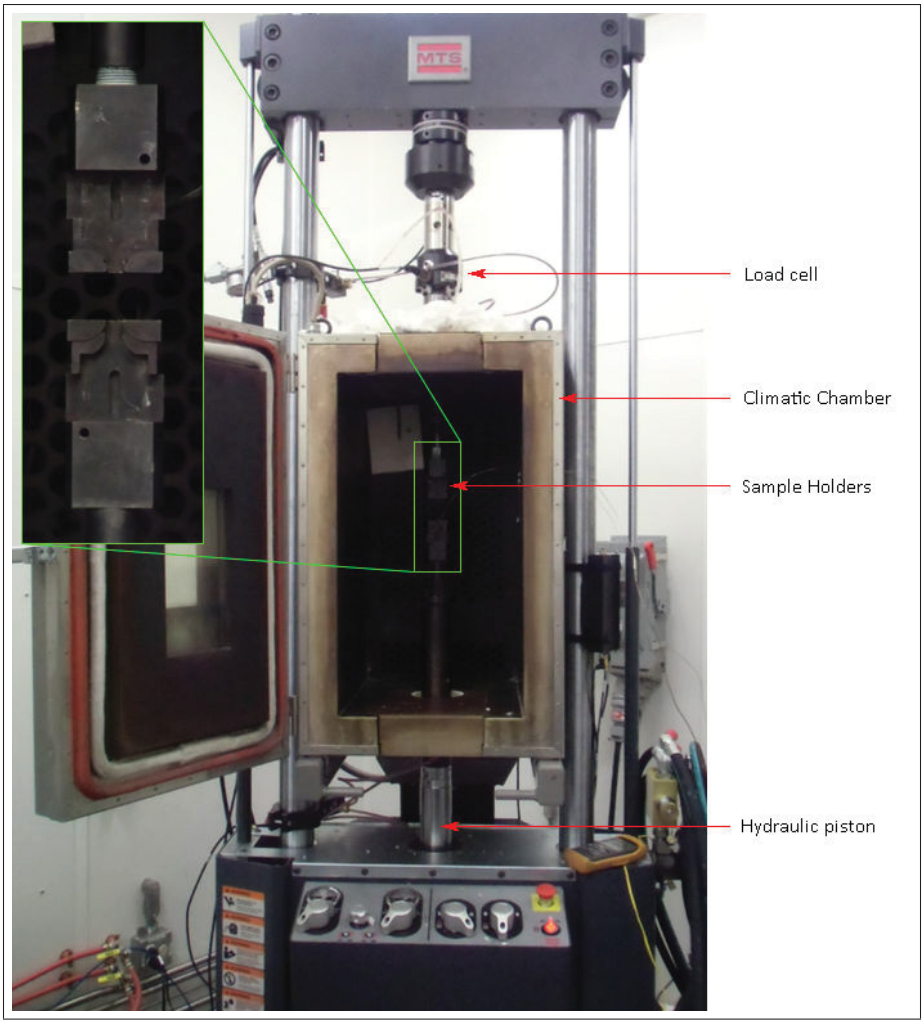

Figure 2.1 Tensile test apparatus with climatic chamber at NRC

2. Quickly transfer the specimen in a room temperature water bath and agitate until completely cooled;
3. Place the specimen in the holder, inside the climatic chamber;
4. Wait 5 minutes to achieve homogeneous temperature in the specimen and holder;
5. Start traction at the required strain rate;
6. End displacement when fracture has occured;
7. Remove specimen from holder.

Table 2.1 Directions from laminating angle for tests done at different sets of parameters

Temperature [$^{\circ}C$]	**Strain Rate [m/m/s]**		
	0,1	**0,3**	**1,0**
20		0° 45° 90°	
200	0°	0° 45° 90°	0°
300	0°	0° 45° 90°	0°
350	0°	0° 45° 90°	0°
400	0°	0° 45° 90°	0°
440	0°	0° 45° 90°	0°
490	0°	0° 45° 90°	0°

According to the additive deformation formulation, i.e. large displacements but small strains, the elastic component of each strain increment was removed by using the additive strain equation, where the total measured strain (ε^T) is divised in its elastic (ε^E) and plastic (ε^P) components. The formulation is:

$$\varepsilon^T = \varepsilon^E + \varepsilon^P \tag{2.15}$$

It was done with the Young's modulus computed from another series of tests with an extensometer (see Section 2.4). The extraction of plastic strain is done by removal of the elastic strain, which is computed by dividing the total stress increment ($\dot{\sigma}^T$) by the Young's modulus (E).

$$\dot{\varepsilon}^P = \dot{\varepsilon}^T - (\dot{\sigma}^T/E) \tag{2.16}$$

2.2 Anisotropy

The anisotropy caused by the sheet's laminating is also characterized via a campaign of uniaxial tensile tests at limited strain.

The same kind of dog bone shaped specimens were first measured on a CMM, stretched at 15%, and then measured again at the same location after unloading. Exept for the premature stop, the procedure used was the same as for the uniaxial tensile tests. The stop at 15% ensured that only the plastic deformation was measured, although with the caveat that internal stresses may prevent a full return to the wanted configuration. This effect is negligible and not considered in future calculations.

For specimens stretched at higher temperature, a strain of 20% was chosen. These strains correspond to the point slightly before the onset of geometrical instabilities as observed in the uniaxial tensile tests. This provides the desired level of precision in the most critical window of material deformation while not being influenced by the instabilities.

Measurements were exported as four series of points in space, each series being a set of measures at an interval of 0.1 mm along each face of the specimen. An example of the analysis is shown in Figure 2.2. A line was traced as a best fit through the points on one side with the least R^2 method to create a reference side. Subsequently, the shortest distance from each point on the other side is computed and averaged with the following equation:

$$\sum_{i=1}^{n} |A * x_i - y_i + \frac{B}{(A^2+1)^{1/2}}| \tag{2.17}$$

This method has the advantage of eliminating any error due to misalignment along the global machine axis. Each specimen could also be checked by displaying the measured points in a graph to ensure no necking was discernible, which would indicate that the strain was more than 20% in this area.

2.3 Damage Model

As seen in the specimens' stress-strain curve in figure 3.1, there are two phenomena that occur after the maximum stress has been reached. First, an instability (necking) appears and the following deformation occurs mainly around this section. This instability depends on geom-

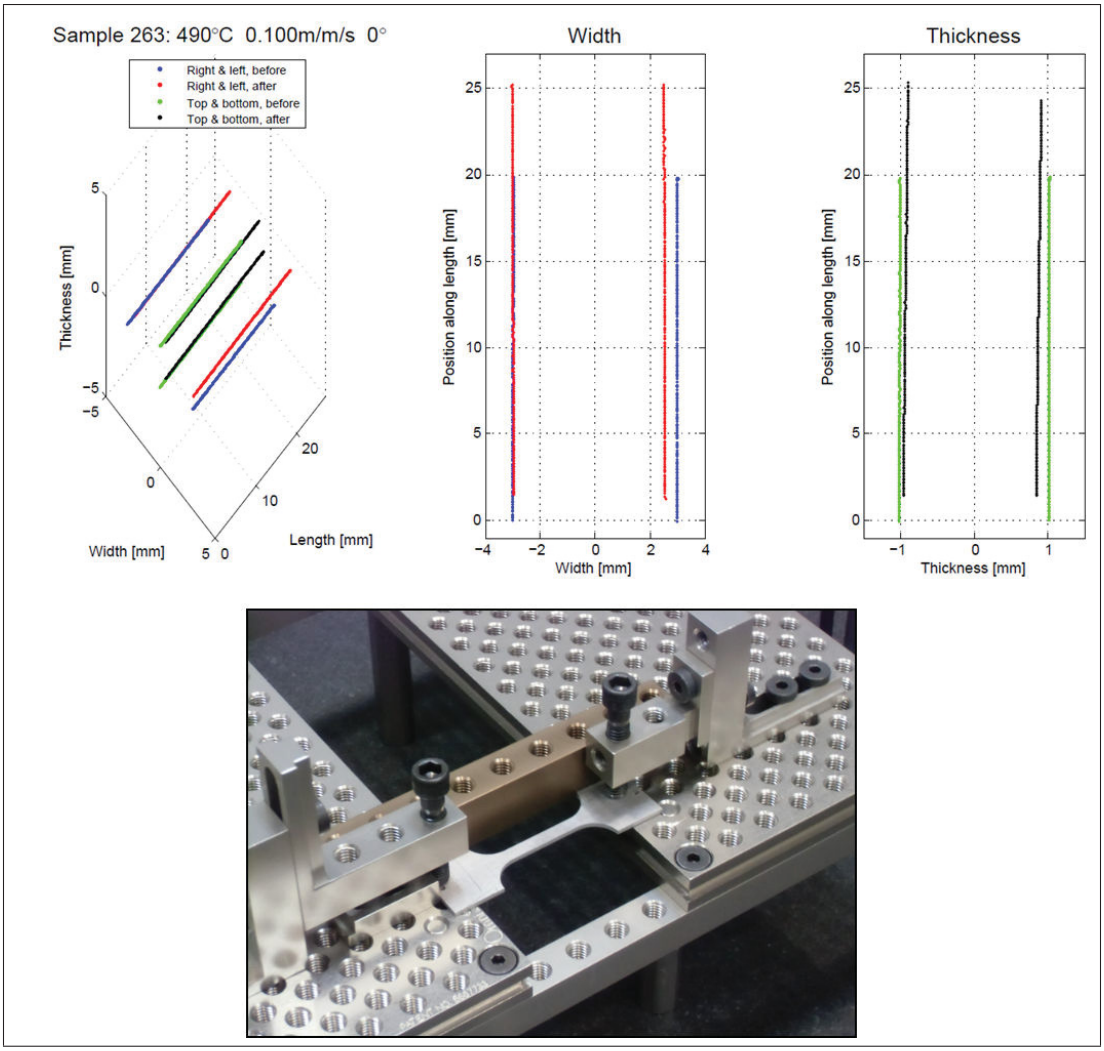

Figure 2.2 Illustrated process for R values measurements

etry, material, loading path, strain rate and temperature. Secondly, there is void nucleation and growth as identified by Mohamed *et al.* (2012) that reaches its critical point, causing the specimen to break.

Due to the highly localized necking (see Figure 3.9) on the specimens, is it clear that the real maximum local stress is obscured in these tests by a change in the section area. However, the elements in future simulations are larger than the necked section, meaning there will be no way to accurately recreate this phenomenon. For example, elements cannot be deformed in a way that recreates a necking on a section shorter than itself. The approach should then be to

recreate the macroscopic stress and strain as observed on a segment of at least the length of the element. Special attention should be given, for example, to any 2 mm element that stretches beyond the failure point of the strain as measured on a 2 mm section centered on the fracture plane of the specimen.

The typical criterion used in hot stamping for a feasibility study is a forming limit diagram but it requires extensive testing that was out of scope for this project. A single plastic strain limit will be used instead for a fracture analysis and is based on the uniaxial specimen's strains measured near the fracture surface.

Broken specimens from the uniaxial tests campaign were recovered and measured near their fracture surface. Although it would be best to measure the dimensions of the fracture surface directly, the measure of the dimensions at 1 mm from the extremity is more repeatable and has other advantages as mentioned in the preceding section.

The computation of the local strain relies on the assumption of no volumetric change in the necked section. The final cross-sectional area is compared to the initial dimensions with the relation:

$$\varepsilon_{true} = ln\left(\frac{l}{l_0}\right) \equiv ln\left(\frac{A_0}{A}\right) \tag{2.18}$$

2.4 Young's Modulus

Additional uniaxial tests were made to measure the Young's modulus with the help of a high temperature rated extensometer. These additional tests were made to help correct for the gage length in previous test results and ensure the precision of position data obtained by the testing apparatus. Good agreement was found between strain when comparing the extensometer's reading with the strains with the corrected gage length of 36 mm.

2.5 Thermal Contact Conductance

Accurate thermal contact conductance parameters are necessary to correctly predict the heat transfer, and consequently material stresses and ductility as well as the final metallurgy of the stamped part.

Contact pressure is the main driving factor behind variations in contact conductance. Other factors such as surface finish, lubrication and the nature of the materials themselves are neglected in favour of an average $h_{contact}$ that encompasses all the variations. Also, due to the movements of the blanks and wear on the dies, these conditions change during the forming process and throughout the life of the tooling. Indeed, many different surface finishes of the blank are observed during hot stamping due to the plowing effects as described by Menezes *et al.* (2009). Moreover, the lubrication is also displaced when this phenomenon is seen.

A series of experiments from Lewis & Perkins (1968) showed that heat conductance at the interface between stainless steel and aluminium, as encountered in hot stamping, varied from 450 $\frac{W}{m^2K}$ to almost 5000 $\frac{W}{m^2K}$ at contact pressures around 4 MPa. These values were found to depend mainly on contact pressure and surface finish.

Another study by Ying *et al.* (2017) showed heat transfer coefficients under hot stamping conditions with AA707 of approximately 50 $\frac{W}{m^2K}$ to 5000 $\frac{W}{m^2K}$. This study used a similar design as the current project both in material and in technique.

The experimental setup presented in Figure 2.3 was used as a simplified case of unidirectional heat transfer during hot stamping.

The dies are 100 mm in diameter at the contact interface, made of D2 steel as is commonly used in hot stamping of aluminium. At a height of 16 mm, the section is reduced to be adapted to existing equipment. The surface that comes in contact with the specimen is initially rough (as machined) for the first half of the tests and then polished before the second half of the tests to explore the differences between the two. Cooling channels with flowing water at constant

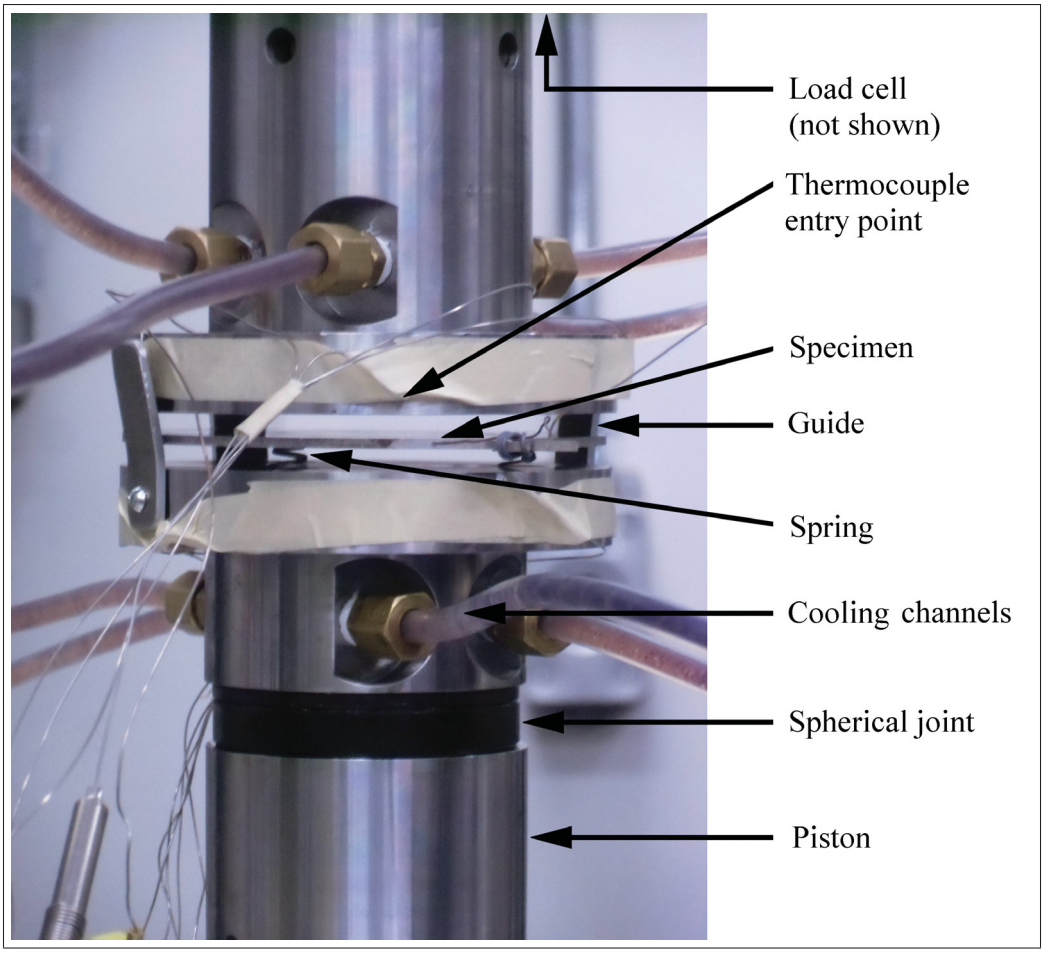

Figure 2.3 Experimental apparatus for the contact conductance

temperature were used as heat sinks during the tests, once again to reproduce conditions seen in hot stamping.

The procedure is as follows:

1. Heat the specimen to 490°*C* in an electric convection oven;
2. Transfer the specimen on the springs;
3. Close the dies;
   3.1. First movement is at 50 mm/s until the gap left is 1 mm;
   3.2. Second movement is at 1 mm/s until contact pressure is reached.
4. Wait for complete cooling of the specimen;
5. Remove specimen from dies.

he strategy to find the values of $h_{contact}$ under different conditions is to perform the test and then find a value of $h_{contact}$ that allows a simulation to reproduce the cooling rate of the specimen.

The first step is to accurately recreate the test in a full three dimensional model to ensure that the heat flow is as expected. At the center axis, the heat flow should be mostly unidirectional, with few radial losses. This test showed that at most, only 1% of the heat flux is radial and the rest flows directly from the contact surface to the heat sink. Due to the high computational cost of such a model and the number of iterations required to precisely calibrate the values of $h_{contact}$ as a function of contact pressure, a unidimensional finite-difference methodology is used.

A simplified flowchart (Figure 2.4) shows the general steps used to reach a thermal conductance versus pressure contact curve that yields results as similar as possible to the experimental data.

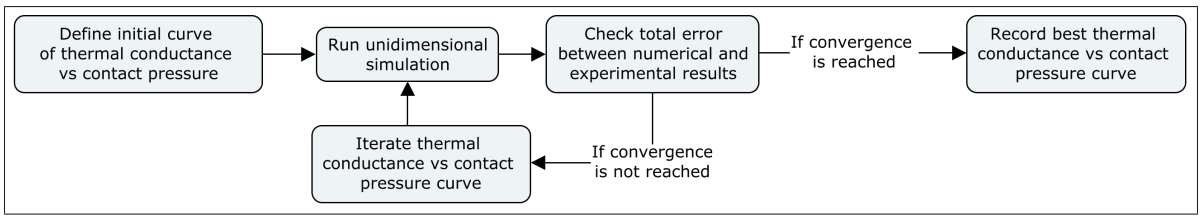

Figure 2.4 Overview of optimization process for thermal conductance definition as a function of contact pressure

The finite-difference method with explicit time integration was chosen due to the possibility of a straightforward implementation in commercial coding software. The test is first divided in three phases where the contact between the specimen and the dies are different, as shown in Figure 2.5.

The material is discretized along the central axis. Each node represents a cylinder of material that follows the lumped capacitance basic assumptions. The space interval for the nodes inside a material is Δx while the time is discretized through the equation:

$$t = p\Delta t \tag{2.19}$$

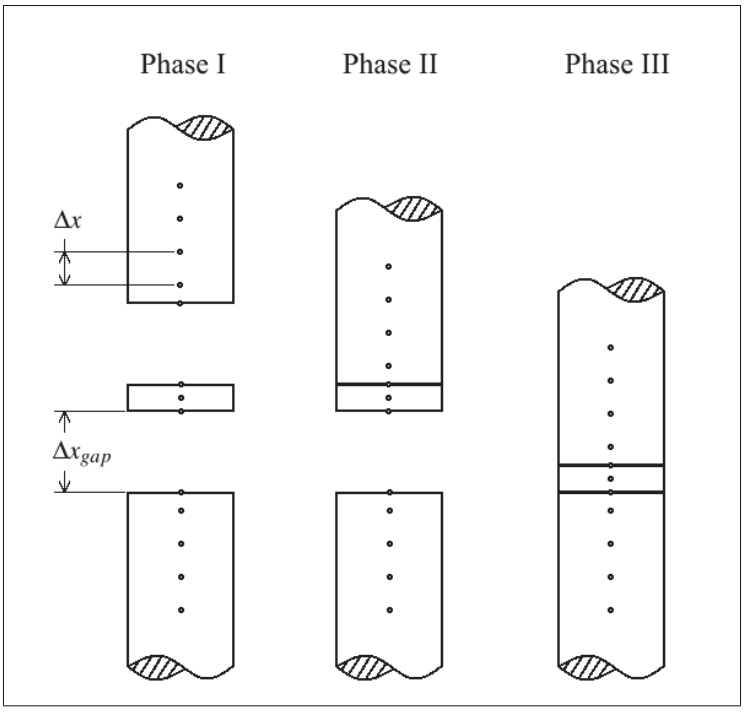

Figure 2.5 Three phases of the test with different contact conditions

Where p is an integer and Δt is a time interval. In this case, the interval is also used as the timestep size for the numerical model. Assuming that for a brief moment in time (at p) the material properties are constant, the general heat rate can be approximated as:

$$\left.\frac{\delta T}{\delta t}\right|_n \approx \frac{T_n^{P+1} - T_n^P}{\Delta t} \tag{2.20}$$

The only terms needed from the general heat rate equation are:

$$\dot{E}_{in} = \dot{E}_{stored} \tag{2.21}$$

From which we can construct the general equation for an interior node 2, between the node 1 and 3:

$$\frac{kA}{\Delta x}(T_1^P - T_2^P) + \frac{kA}{\Delta x}(T_3^P - T_2^P) = \rho c A \Delta x \frac{T_2^{P+1} - T_2^P}{\Delta t} \tag{2.22}$$

$$T_2^{P+1} = \left(\frac{k\Delta t}{\rho c \Delta x^2}\right) T_1^P + \left(\frac{k\Delta t}{\rho c \Delta x^2}\right) T_3^P + \left(1 - 2\frac{k\Delta t}{\rho c \Delta x^2}\right) T_2^P \tag{2.23}$$

Since the boundary condition is assumed to be a perfect heat sink at the cooling channels, we can simply use $T_{n,\,cooling\,channel}^{P+1} = T_{n,\,cooling\,channel}^{P}$.

Surface nodes require the consideration of both the radiation and convection. It is necessary to have surface nodes to compute the heat transfer that is dependent on said surface temperatures. Each node represent half of other discretized sections ($\frac{\Delta x}{2}$). Moreover, the radiation must be linearized in order to be able to compute the stability criterion for explicit time integration. The general formula for radiation flux on the surface i from surface j, assuming the absorptivity is equal to the emissivity, is:

$$\dot{E}_{in,rad} = \varepsilon \sigma F_v A (T_i^4 - T_j^4) \tag{2.24}$$

By defining:

$$h_r \equiv \varepsilon \sigma F_v (T_j - T_j)(T_i^2 - T_j^2) \tag{2.25}$$

It follows that:

$$\dot{E}_{in,rad} = h_r A (T_i - T_j) \tag{2.26}$$

The view factor F_v is a simplification of Figure 13.5 in (Bergman *et al.*, 2011) where both discs are the same diameter and only the distance L varies as the dies close.

$$F_v = \frac{L^2 - \sqrt{L^2(L^2 + 10000)} + 5000}{5000} \tag{2.27}$$

The value of F_v varies from 0.8 to 1 as the dies close, which means its effect is non negligible. With that information, we can build the equation for a surface node with conduction in the material, conduction to the ambient air and radiation. This equation requires the temperature of the opposing surface (T_1), the current node on the surface (T_2) and the adjacent node inside

the material (T_3).

$$\frac{kA}{\Delta x}(T_3^P - T_2^P) + \frac{k_{air}A}{\Delta x_{gap}}(T_1^P - T_2^P) + \frac{h_r^P A}{\Delta x_{gap}}(T_1^P - T_2^P) = \rho cA\Delta x\frac{T_2^{P+1} - T_2^P}{\Delta t} \tag{2.28}$$

Which is solved for T_2^{P+1}:

$$T_2^{P+1} = \left(\frac{2k_{air}\Delta t}{\rho c\Delta x\Delta x_{gap}} + \frac{2h_r^P\Delta t}{\rho c\Delta x}\right)T_1^P + \left(\frac{2k\Delta t}{\rho c\Delta x^2}\right)T_3^P + \left(1 - \frac{2k_{air}\Delta t}{\rho c\Delta x\Delta x_{gap}} - \frac{2h_r^P\Delta t}{\rho c\Delta x} - \frac{2k\Delta t}{\rho c\Delta x^2}\right)T_2^P \tag{2.29}$$

The last equation to build is the case of contact between two surfaces. Since it is dependent upon the contact pressure, the value of $h_{contact}$ is interpolated in a table of values provided by the optimization algorithm. It is presented with the same node numbering convention as the previous equation:

$$\frac{kA}{\Delta x}(T_3^P - T_2^P) + h_{contact}^P A(T_1^P - T_2^P) = \rho cA\Delta x\frac{T_2^{P+1} - T_2^P}{\Delta t} \tag{2.30}$$

Once again solved for T_2^{P+1}:

$$T_2^{P+1} = \left(\frac{2h_{contact}^P\Delta t}{\rho c\Delta x}\right)T_1^P + \left(\frac{2k\Delta t}{\rho c\Delta x^2}\right)T_3^P + \left(1 - \frac{2h_{contact}^P\Delta t}{\rho c\Delta x} - \frac{2k\Delta t}{\rho c\Delta x^2}\right)T_2^P \tag{2.31}$$

Equations 2.31, 2.29 and 2.23 require that the term multiplying the current node temperature be positive, otherwise there are induced instabilities that are clearly recognizable by their non-obedience to the law of conservation of energy. For example, in 2.31 the criterion is:

$$1 - \frac{2h_{cond}^P\Delta t}{\rho c\Delta x} - \frac{2k\Delta t}{\rho c\Delta x^2} \geqslant 0 \tag{2.32}$$

For a fixed node spacing, the only way to make sure this criterion is met is to reduce the time step size Δt.

Due to the fact that a thermocouple inherently measures its own temperature and not the specimen itself, it is necessary to include the latency and offset between those two temperatures. The manufacturer of the chosen thermocouple documented a time constant τ of 0.16 s in water. An arbitrary increase of 50% of this value accounts for the lesser conductivity of the current setup versus these experimental conditions. This value seemed to best recreate the overall shape of the recorded temperature curves.

The temperature read by the thermocouples are modelled by nodes located orthogonally to the uniaxial grid representing the problem. The general equation for the thermocouple's heat flux is:

$$h_{eq}A(T^P_{real} - T^P_{TC}) = \rho cA\Delta x \frac{T^{P+1}_{TC} - T^P_{TC}}{\Delta t} \tag{2.33}$$

Which, when the next thermocouple's temperature (T^{P+1}_{TC}) is isolated, becomes:

$$T^{P+1}_{TC} = \left(\frac{h\Delta t}{\rho c\Delta x}\right) T^P_{real} + \left(1 - \frac{h\Delta t}{\rho c\Delta x}\right) T^P_{TC} \tag{2.34}$$

Moreover, we know that when $\Delta t = \tau$, $T^P_{TC} = 0$ and $T^P_{real} = 1$ that $T^{P+1}_{TC} = 0.63$ from the documentation.

$$0.63 = \frac{h\tau}{\rho c\Delta x} \tag{2.35}$$

$$h = 0.63\frac{\rho c\Delta x}{\tau} \tag{2.36}$$

Which, when entered in 2.34, gives us:

$$T^{P+1}_{TC} = \left(0.63\frac{\Delta t}{\tau}\right) T^P_{real} + \left(1 - 0.63\frac{\Delta t}{\tau}\right) T^P_{TC} \tag{2.37}$$

This result is logical, since the evaluation of the time constant already encompasses the geometrical and material parameters of the thermocouple itself. It is also interesting to note that the stability criterion, $1 - 0.63\frac{\Delta t}{\tau} \geqslant 0$, is much looser than for other nodes in the model.

These equations are entered in different functions that recreate the three phases of the test and control the time step to keep the simulation stable.

Finally, several iterations of a prospective conductance over pressure curve are made using a simple pattern (or black box) search. These curves are defined with only three data points and are interpolated linearly. The coordinates are at pressure 0, at the nominal pressure of the test and at the maximum pressure recorded in the data. This distribution enables the simulation to take into account any initial "bumping" of the tooling on the specimen during a critical moment of the test, i.e. when the heat flux is near its maximum, at contact and immediately after.

2.6 Finite Element Analysis of the Stamping Operation

2.6.1 Part Description

The part's CAD is supplied by a member of ALTec, a consortium of companies financing research in aluminium transformation. A set of dies were already machined for previous research on that part and their CAD models were remeshed specifically for the purpose of the following simulations.

The part is a prototype for a battery support (BS) part in a Telsa car. The BS part was chosen because it represented a forming challenge due mainly to its 3D corner, located at the lower left in Figure 2.6. It also required high material strength due to being an integral part of the car's structure. The success parameters for forming were similar to those of other structural applications such as the A, B and C pillars commonly found in cars.

It is made of AA7075 that was solution heat treated by having spent 18 minutes in an electrical convection oven prior to its insertion in the dies. The forming procedure is described in Table

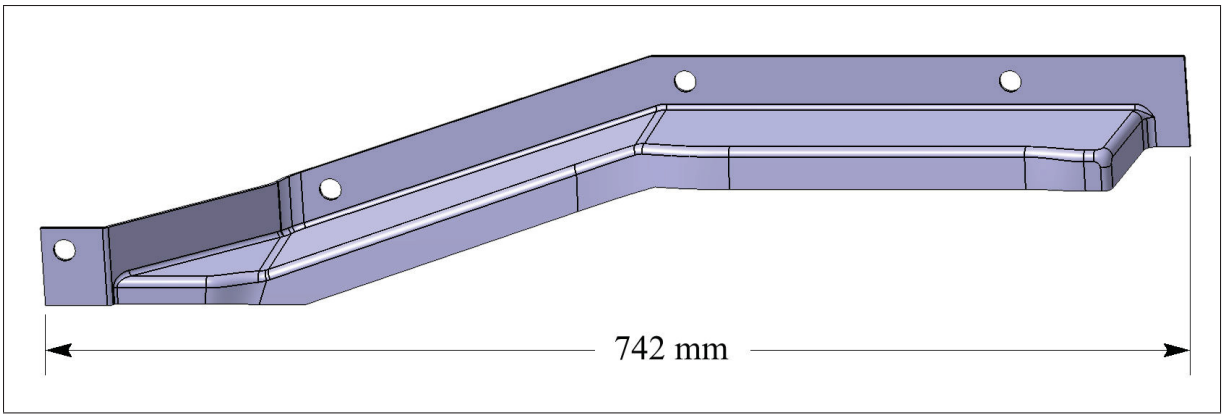

Figure 2.6 CAD model of the battery holder

2.2. There were some variations from these averages but videos from the stamping campaign showed generally less than 2 seconds variation due to human manipulation. The hydraulic press used to control the dies' movements was given a position command for the whole cycle.

Table 2.2 Steps for a BS part forming under laboratory conditions

Step	**Duration [s]**	**Part temperature at end of step [$^{\circ}C$]**	**Included in FEA**
Heating	1080	480	No
Transfer to the dies	8	440	Yes
Forming	4	200	Yes
Die quenching	20	50	Yes
Dies opening and part extraction	20	40	No
Air cooling	600	20	No

Dies are designed around the part from the nominal 2.0 mm thickness. The assembly for the lower die is shown in Figure 2.7 and the upper die is a mirror of this design, not shown here to maintain visibility of the surface's details. It features sliding rods at each corner and an insulating panel as a resting surface for previous cooled and heated die experiments. There is no contact with the dies from any metallic part that could form a heat bridge.

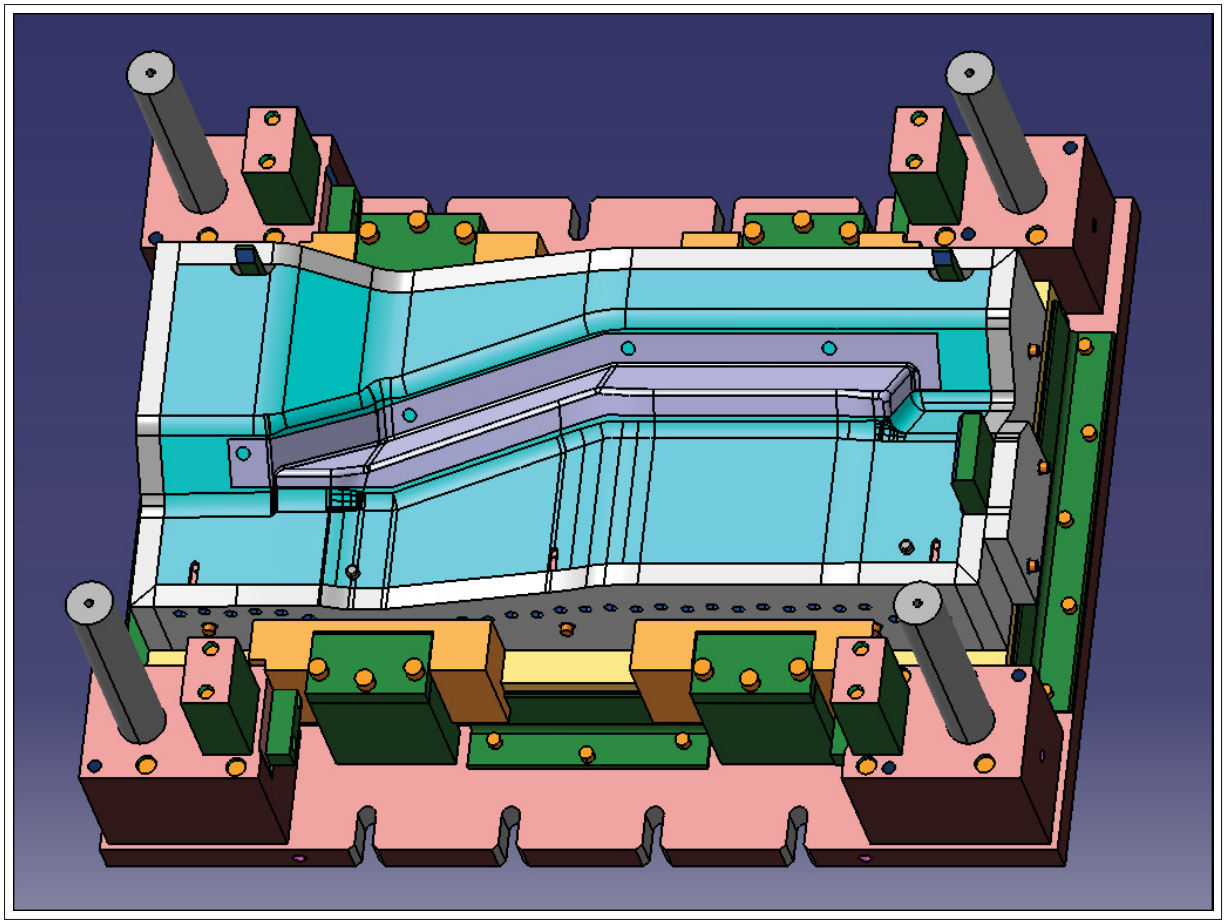

Figure 2.7 CAD model of the lower die

There was minimal instrumentation on the tooling. The upper die position was recorded as well as the vertical reaction force caused by the stamping operation. Oven temperature was maintained between 2 $^{\circ}C$ and the evolution of blank temperature during heating and positioning was recorded with a dummy blank that had a thermocouple riveted in. This dummy could not be stamped as the thermocouple and rivet would have damaged the dies. This test allowed the confirmation that the blank was sufficiently heated in the 18 minutes it spent inside the oven and that the heat loss due to convection is as expected. Finally, coolant temperature was recorded and provided a rough idea of the dies' temperature prior to forming.

2.6.2 Numerical Model

A generic solver deck for all following simulations is included in Appendix I, and should be read in conjunction with the LS-DYNA user manual for an in-depth analysis. To improve readability, the main features are summarized here.

The simulation relies on an implicit solver with a time step that is adjusted between 1E-08 and 1 second by the software. It runs nominally for 20 seconds in order to reach a sufficient temperature equilibrium. Initial temperature of the dies is $18°C$ and the sheet is around $460°C$. The lower die is fixed in place and the upper die has its position controlled by a displacement versus time curve obtained from the experimental data. The nodes located at the cooling channels' location are maintained at the cooling fluid's temperature throughout the duration of the simulation. The contact is defined as a penalty formulation applied on the segments at the surfaces of the blank and dies, whose amplitude is based on the material's stiffness. The thermal contact is as described in Section 3.7.

Elements are simply defined as rigid for the dies while the blank uses fully integrated shells, a formulation derived from the Hu-Washizu three-field principle. The material model is the same as described in Section 2.1, except that the changes in heat capacity and thermal conductivity due to temperature changes are taken into account.

Mechanical contacts are resolved via a penalty applied on nodes when a penetration of mesh surface is detected. Thickness with effects of temperature dilation and thinning is taken into account. Thermal contact is designed to recreate the behaviour proposed in Table 3.4.

Initial blank temperature at oven exit was recreated by applying a uniform temperature on the blank's nodes. The transfer from the oven to the dies lowered general temperature but the distribution was assumed to remain homogenous since the there was very little effect of the edges due to the proportions of the sheet, approximately 820 mm by 230 mm with a thickness of 2 mm. There was a convection of 25 $W.m^{-2}.K^{-1}$ when no other part was in range for heat exchange. At a spacing 10 mm, the equation for gap in Table 3.4 entered into function and

convection towards fixed temperature air was stopped. Dies were set with an initial temperature applied at all nodes. The only exeption were all nodes representing the cooling channels that had a fixed temperature for all the duration of the FEA.

Initial positioning of the blank in the dies in the FEA was made by trial and error until the final part was positioned similarly from its physical counterpart. Measurements for this were taken at the four corners and a variation of less than 2 mm at each corner was considered adequate. At the beginning of the FEA, gravity was applied to the blank, making it fall on the dies to recreate local cooling at contact locations. No translational or rotational degrees of freedom constraints were used for the blank.

Upper die movement was recreated by using the position versus time data from the experiment on the Z axis of translation. All other linear and rotational degrees of freedom were locked. The lower die was entirely locked into place. These constraints were applied on all nodes via the material definition.

CHAPTER 3

RESULTS

3.1 Strain and Strain Rate Effects

Resulting curves of stress versus plastic strain were then sampled at 1% strain intervals between their yield point (at 0.2% strain offset) and their ultimate stresses. This allowed for standardized data to be used for the simulations. Figure 3.1 shows a graphical example from a test at 200°C.

It also shows multiple points after the ultimate stress is reached that follow a small slope of 2 MPa per unit of strain to aid in convergence. Indeed, if a force constraint that makes an element exceed the maximum stress is imposed, the element would stretch to infinity. Inversely, a boundary condition of strain increase would yield no stress increase and the solver's tolerance on convergence would only see numerical noise due to variable's precision. This effect is reduced by the correct implementation of the absolute (by opposition to the other relative) convergence tolerance in the solver. Instability and damage are handled by a different set of inputs in the solver deck.

It is interesting to note that at higher temperatures and especially at lower strain rates, the near ultimate stress was reached early on. However, the behaviour was perfectly plastic for a strain of up to 50% before the onset of necking was visible.

An overview of all obtained data is shown in Figure 3.2. A first important point to discuss is the fact that yield stress at 20°C is lower than at 200°C. Traction tests at 20°C were done immediately after a SHT and quenching, resulting in a -W heat treatment. In other tests at higher temperatures such as at 200°C, re-heating caused hardening to start in an ageing phenomenon, giving it a temper that may begin to enter the -T4 category. At a strain of approximately 5%, hardening at 20°C finally overtakes that of 200°C, which was subjected to continuous recovery.

Anisotropy has an effect on yield strength that gradually lowers as temperature increases and become nearly indistinguishable at 350°C. This change also occurs as the hardening becomes

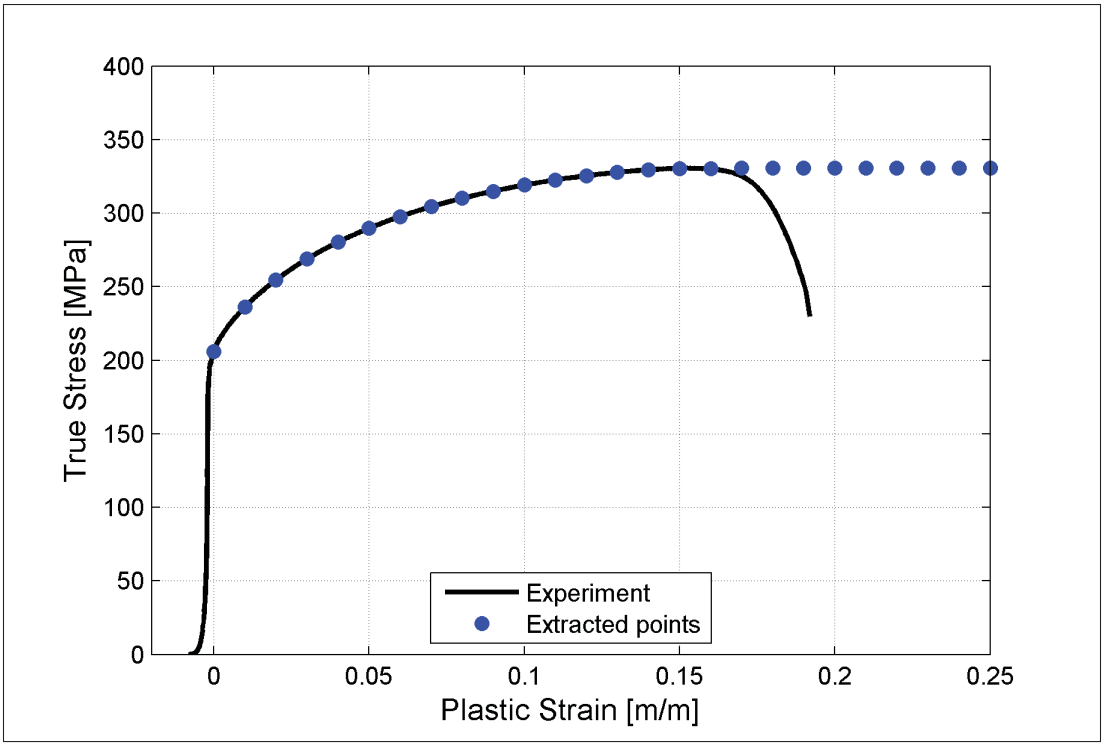

Figure 3.1 Data extraction from experiments

linear. The only difference between temperatures is the location of the instability and the strain at break, not visible on this picture due to the 2 MPa per unit of strain extrapolation mentioned earlier.

To confirm the adequate functioning of this critical characterization step, a simple uniaxial test was modelled. The test was limited to the strain at which the maximum stress is reached. A good agreement was found between the datasets, as shown in Figure 3.3. The comparison was made with the raw data from the test, i.e. the load and displacement values, to weed out the possible biasing effects of data post treatment.

The small curvature in the beginning of the experimental curves in Figure 3.1 are assumed to be due to the apparatus settling in place and not representative of a particular material behaviour.

Another effect to take into consideration is the material flow within the shouldered section, as shown in Figure 3.4. All true strains were calculated with the adjusted gage length that takes

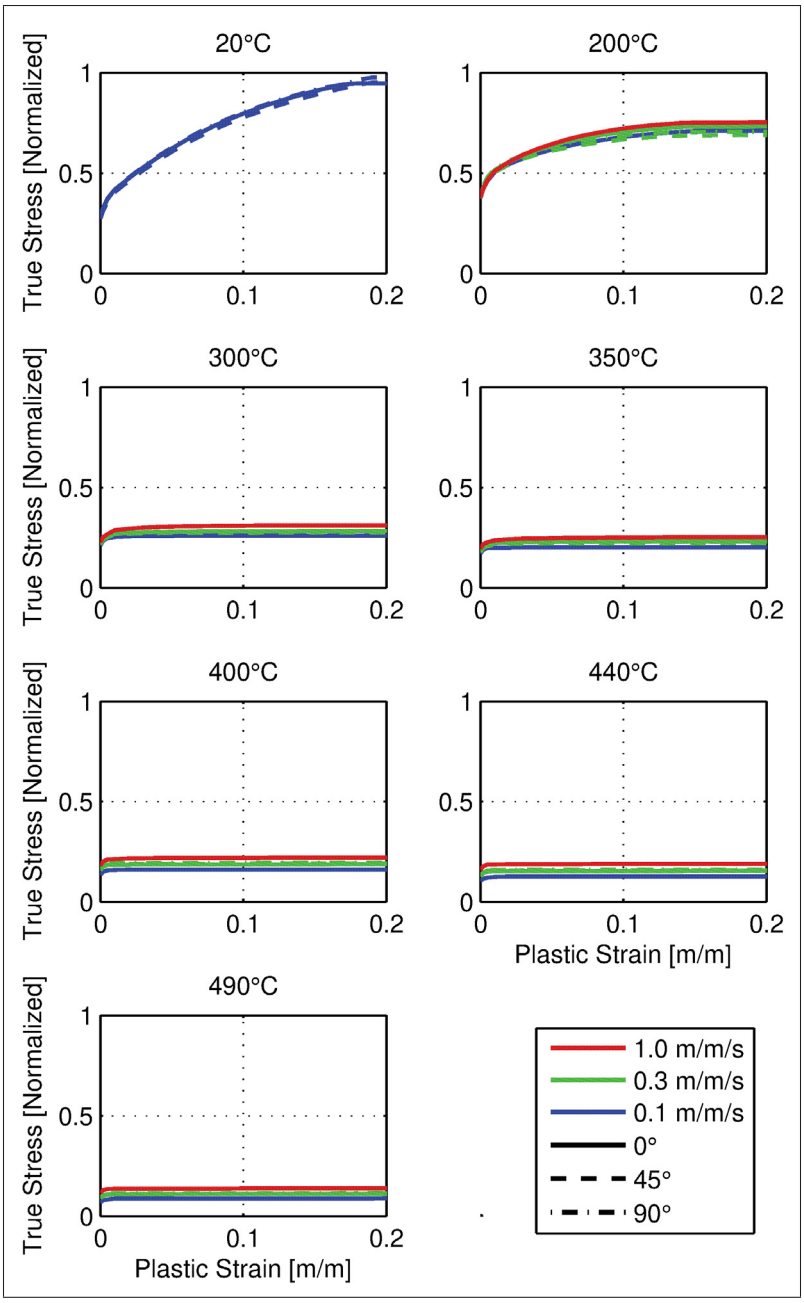

Figure 3.2 Overview of adjusted strain hardening as used for FEA

into consideration two influencing factors. First, there is a small axial stretch in the beginning of the rounded section as the stresses are only gradually diminishing. Also, the FEA shows that there is a small but significant flow of material from the extremities essentially feeding the section being stretched.

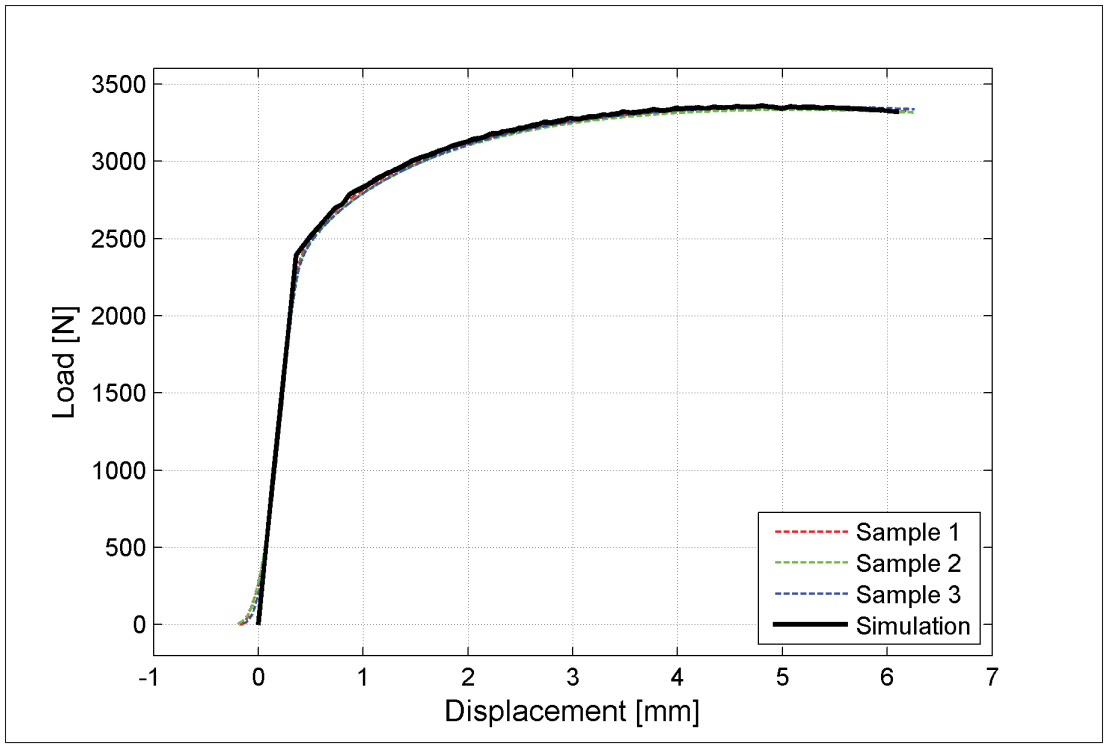

Figure 3.3 Comparison of experimental data and simulation for an uniaxial specimen

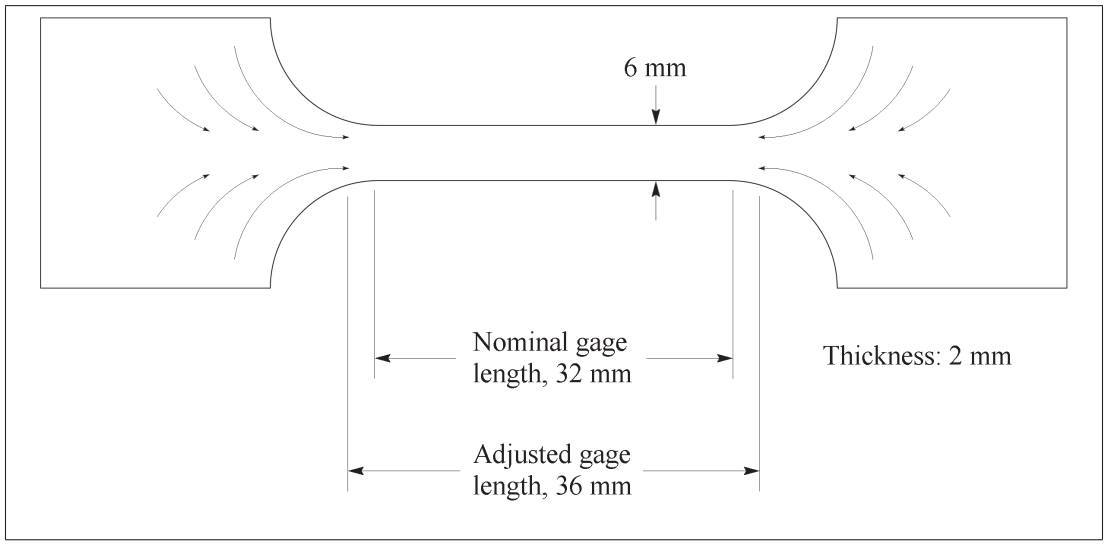

Figure 3.4 Adjusted gage length from material flow

Although chamber temperature was closely monitored, there was sometimes a small difference between the top and bottom jaw. When the top was as little as $5°C$ higher than the bottom one,

necking was invariably observed in the upper half of the specimen's section. Some tests where the temperature difference seemed to have a noticeable impact were repeated.

Finally, the Bauschinger effect is also neglected as the process take place in a single loading phase. Its characterization would only be of use in the springback analysis and would also have a negligible effect in this case.

A set of material properties are chosen for the example of material characterization. Table 3.1 shows the known variables and the resulting material parameters for the Barlat 89 model.

Table 3.1 Example of characterization for the Barlat 89 model at 350°C on AA7075 following SHT

Input Parameters	**Value**	**Resulting Material Model Parameters**	**Value**
R_0	0.658	a	1.17
R_{45}	0.748	c	0.833
R_{90}	0.777	h	0.953
M	8	p	1.06

Material properties at 350°C are used for the example. The correspondig R values are chosen with the exponent $M = 8$ suggested by Barlat & Lian (1989) for FCC materials. The value of p may only be found via an implicit method. This is quite easily performed with a MATLAB script that iterates between values of p in equation 2.1 using a black box search scheme. The convergence to 0.1% of the final value is attained in approximately 15 steps and less than a hundredth of a second, suggesting this does not represent a significant computational burden during the FEA.

The same was done for the Hill 90 model using the same R values and an exponent $M = 1.5$, as advised by the author for FCC material. The results are shown in Table 3.2.

Both yield functions are defined at first using the R values which should allow for the best representation of the strains in the simulation but, as seen in Section 3.5, they also lead to a

Table 3.2 Example of characterization for the Hill 90 model at 350°C on AA7075 following SHT

Input Parameters	**Value**	**Resulting Material Model Parameters**	**Value**
R_0	0.658	a	-0.0832
R_{45}	0.748	b	-0.0444
R_{90}	0.777	c	1.84
M	1.5		

stress anisotropy that is not accurate. Both cause an overestimation of the yield stresses at an orientation of 90° and at 45° in the case of Hill's model. The yields stresses as a function of orientation in uniaxial stress conditions are compared to their experimental equivalent in Figure 3.5.

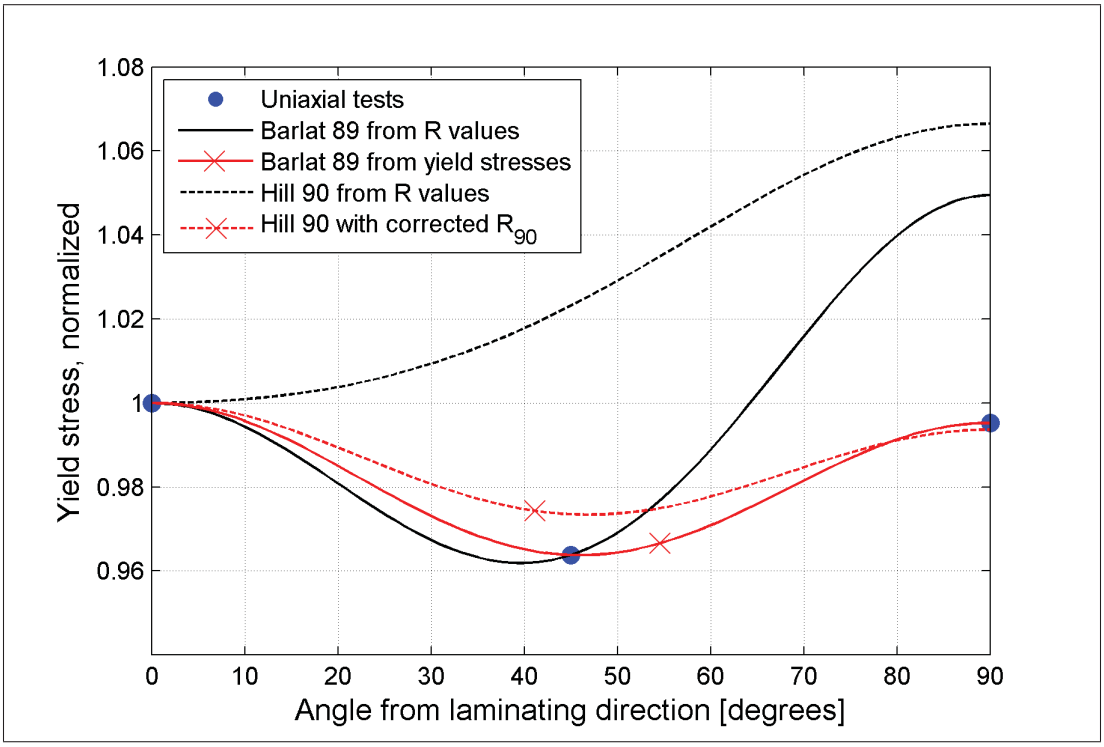

Figure 3.5 Comparison between the Barlat and Hill yield stress at different traction orientations

Barlat proposes another method to characterize the parameters in his equation starting from the yield stresses. This does make the uniaxial yield stresses more representative of the reality but leads to a value of $R_{90} = 0.648$ instead of $R_{90} = 0.777$. The use of this new R value also makes for a much better estimation of the yield surface in the Hill 90 law. The effects of these changes are shown in Figure 3.6.

The choice between a more precise yield surface or a better anisotropic strain behavior is settled by considering the objective of the current project. In this case, the final part's thickness is an important parameter and its total plastic strain is used in the damage model. Therefore, the constitutive law based on the R values is used in the following simulations.

The yield surfaces for cases of biaxial stress show a significant difference at the equibiaxial stress state, suggesting special care on elements subjected to this kind of loading when comparing the models in the parameters study later on.

It is important to note that both models are included in the commercial FEA software used for this project. They allow the input of hardening curves at different strain rates and temperature. The R values may be also entered for different temperatures and strain rates, although that latest feature was not used. An important limitation in these models is the Young modulus that can only be a constant value for all temperatures, which is shown to be dissimilar from reality. A study of the effect of the exponent in both functions with comparisons of biaxial yield stress could lead to a more precise formulation.

3.2 Anisotropy

The reliability of the tests was more than adequate, showing a standard deviation of 0.005 of the R-value coefficient amongst all the specimens. Figure 3.7 shows the evolution of the coefficients as temperature increases.

It is expected to see a diminuation of the R values spread at temperatures nearing the recrystallization point. The crossover of R_{45} and R_{90} between $350°C$ and $490°C$ seen in Figure 3.7

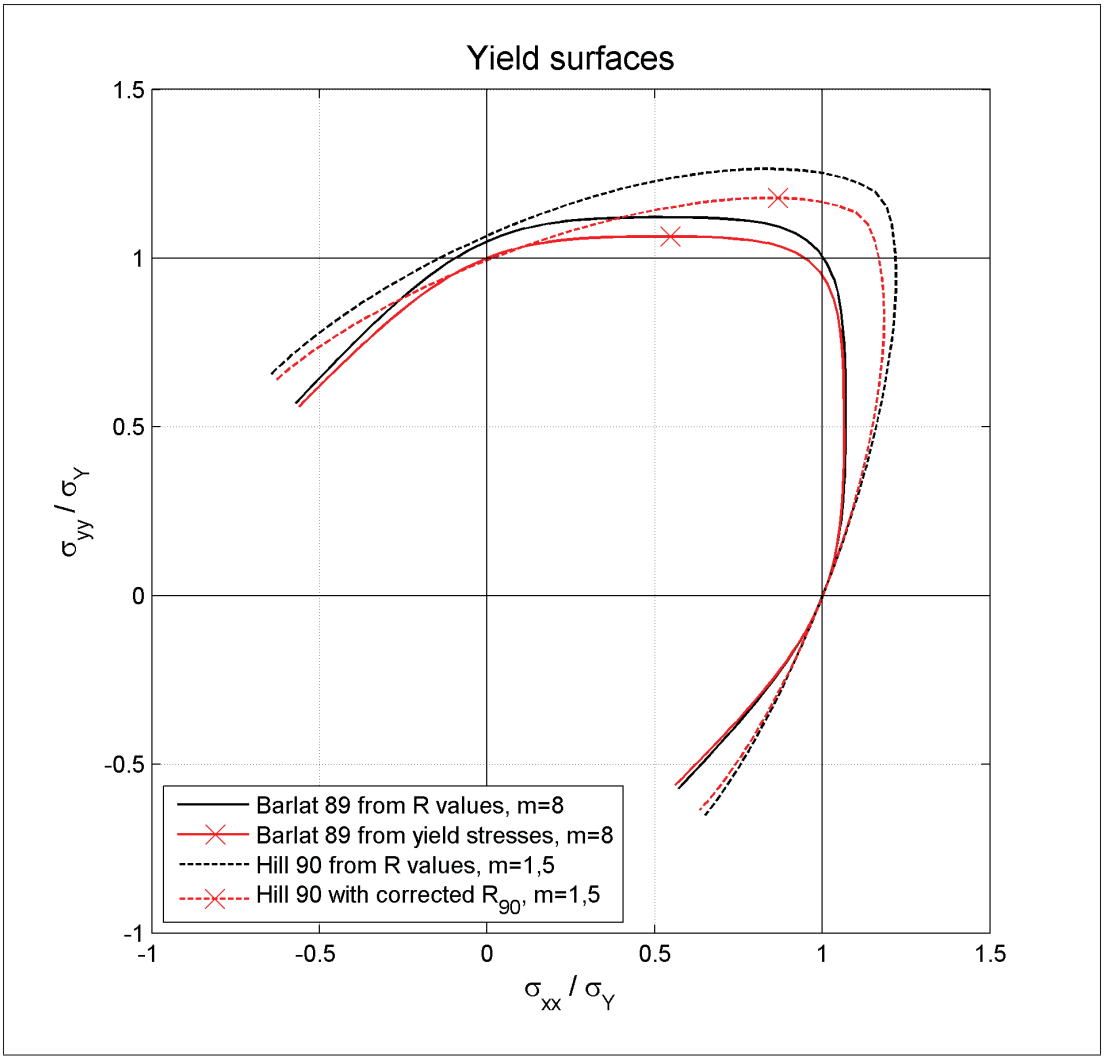

Figure 3.6 Comparison between the Barlat and Hill yield surfaces

seems like a minor imprecision of the measures, especially when taking into account the possibility of a void nucleation and growth already beginning at a strain of 20%. This would have the effect of invalidating the assumption of no volumetric changes that is used in the calculation of the R values and could therefore explain the variation.

Another aspect to be observed with more scrutiny is the general lowering of the R values at 200°*C*. A comparison with Abedrabbo *et al.* (2006) shows that this phenomenon is not something unheard of, as tests on AA3003 aluminium showed somewhat similar non-linearities in the evolution of R values near the 150°*C* mark.

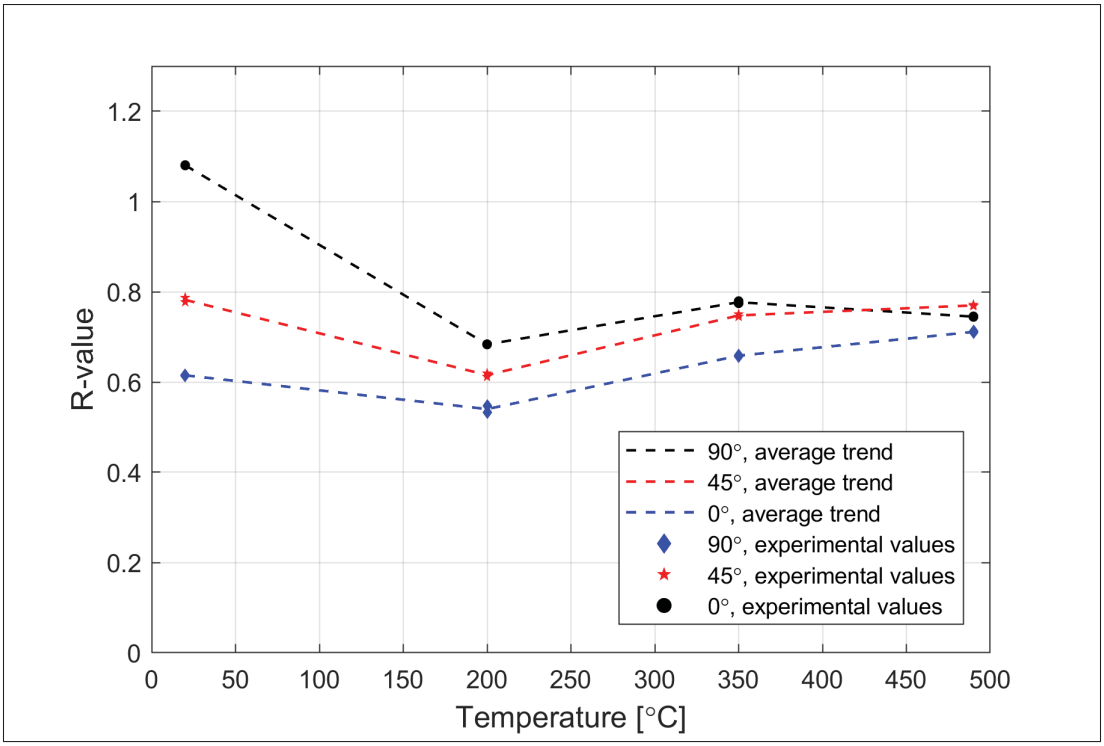

Figure 3.7 R values, average trends and data points

3.3 Damage Model

For each temperature, six random specimens each at an orientation of 0° from the laminating angle, were measured resulting in the graph presented in Figure 3.8.

Lowering of the maximal elongation observed from 400°C and up can be explained by the fact that the initial assumption of constant volume isn't true at those temperatures. This is visible on the fracture surface presenting themselves with different surface finishes indicative of a more porous structure. Furthermore, angles of fracture at temperatures between 20°C and 200°C are approximately 45°, indicating a different damage mechanism than at temperatures of 350°C and higher. In Figure 3.9, it is also possible to see that the geometric instability behaviour changes between 300°C and 400°C and, in a lesser measure, up to 440°C.

These figures show the possible limitations of the proposed damage model due to the diverse mechanisms at play. Also not taken into account are the viscoplasticity effects, where there is

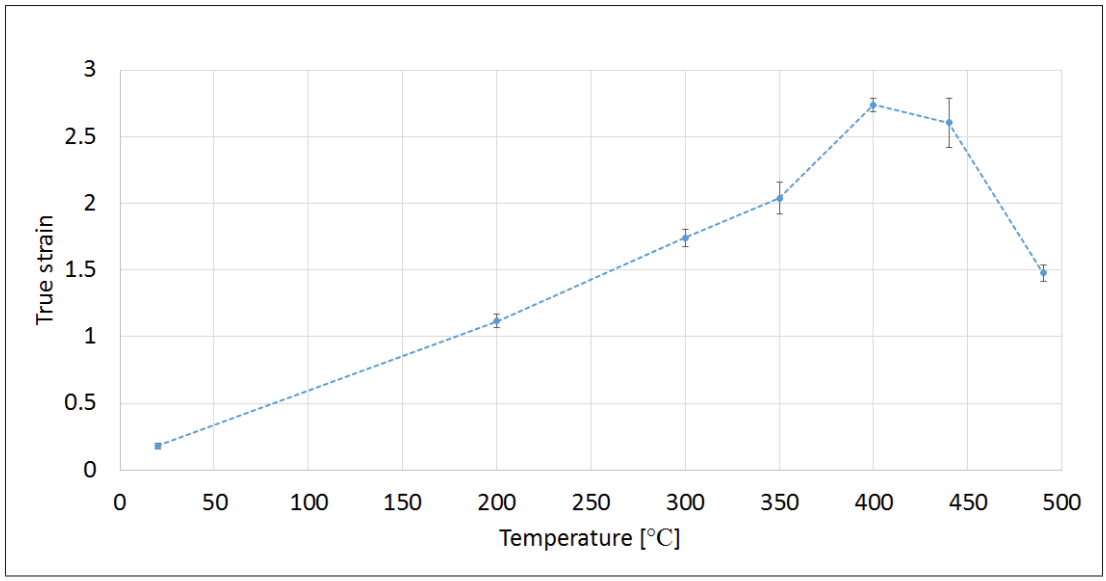

Figure 3.8 Measured strains in the necked sections of the uniaxial specimens

a continuous stress relaxation due to the constant recovery of the aluminium. This relaxation is hard to detect on specimens subjected to constant strain rates but would be more visible on a hot stamping operations where the strain rate is not constant. For the process currently studied, which is more akin to "crash forming", this is not a concern in so far as this phenomenon is already included in the hardening curves at different strain rates.

An effect worthy of mention is the consistency of the strain at which instability begins to appear. As demonstrated in Figure 3.10, it all occurs at a strain of around 25% while the strain at break varies from 40% to 52%.

3.4 Young's Modulus

Since all the components were heated before the tests, no corrections for the initial gage length were necessary. Only the measured cross-sectional area was corrected using the same equations as for the other uniaxial tests. The resulting modulus, taken near the inflection points in the elastic section of the true stress versus true strains are shown in Table 3.3.

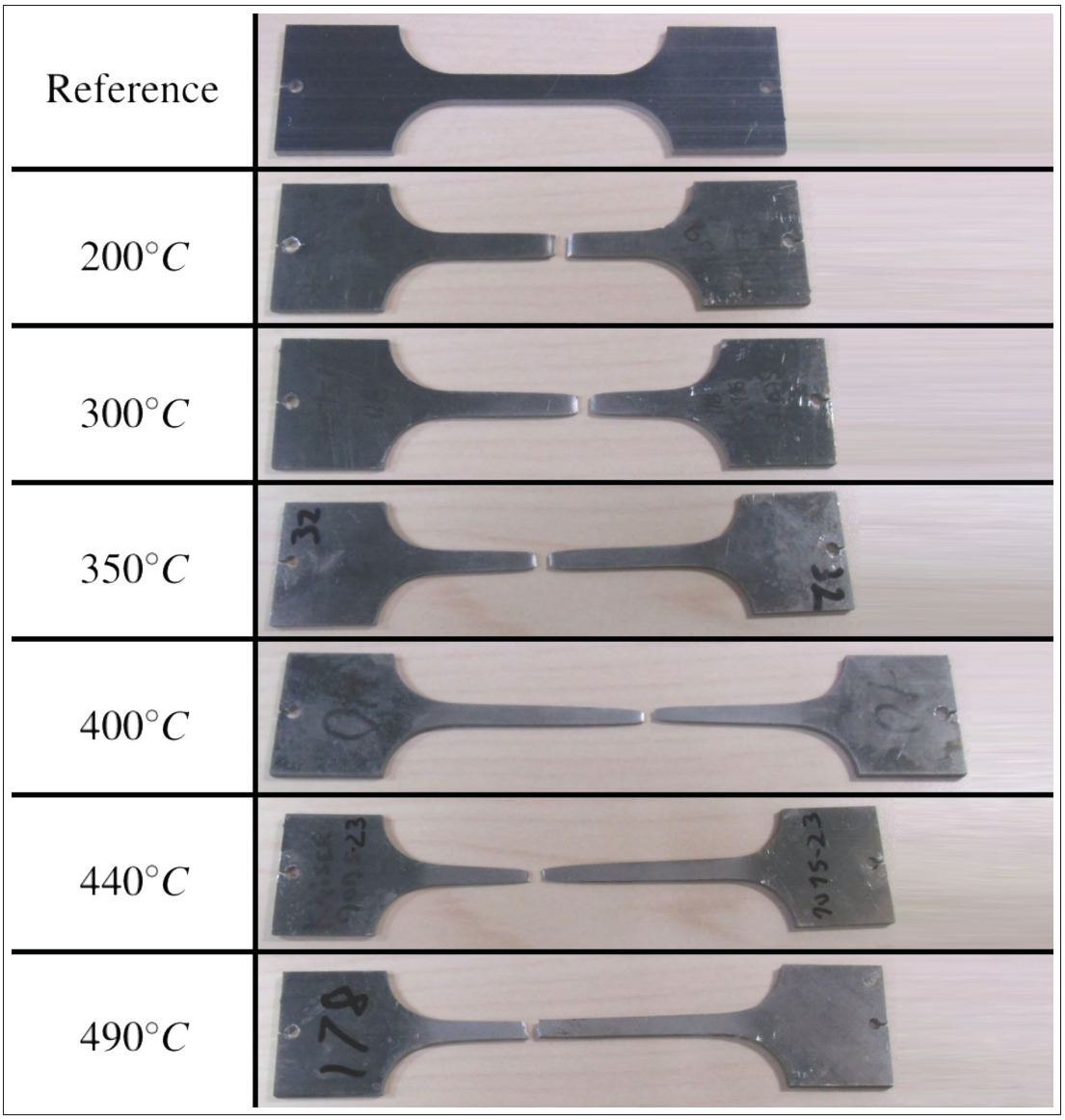

Figure 3.9 Necking of uniaxial specimens at different temperatures

Young's modulus has a limited effect at high temperatures owing to the fact that the yield stresses are much lower. It causes the elements to quickly enter the plastic deformation behaviour governed by the hardening curves. Towards the end of the forming process where the part is much colder, the inverse is true for the yield stresses. As a consequence, the chosen Young's modulus for the simulation errs on the side of a higher value.

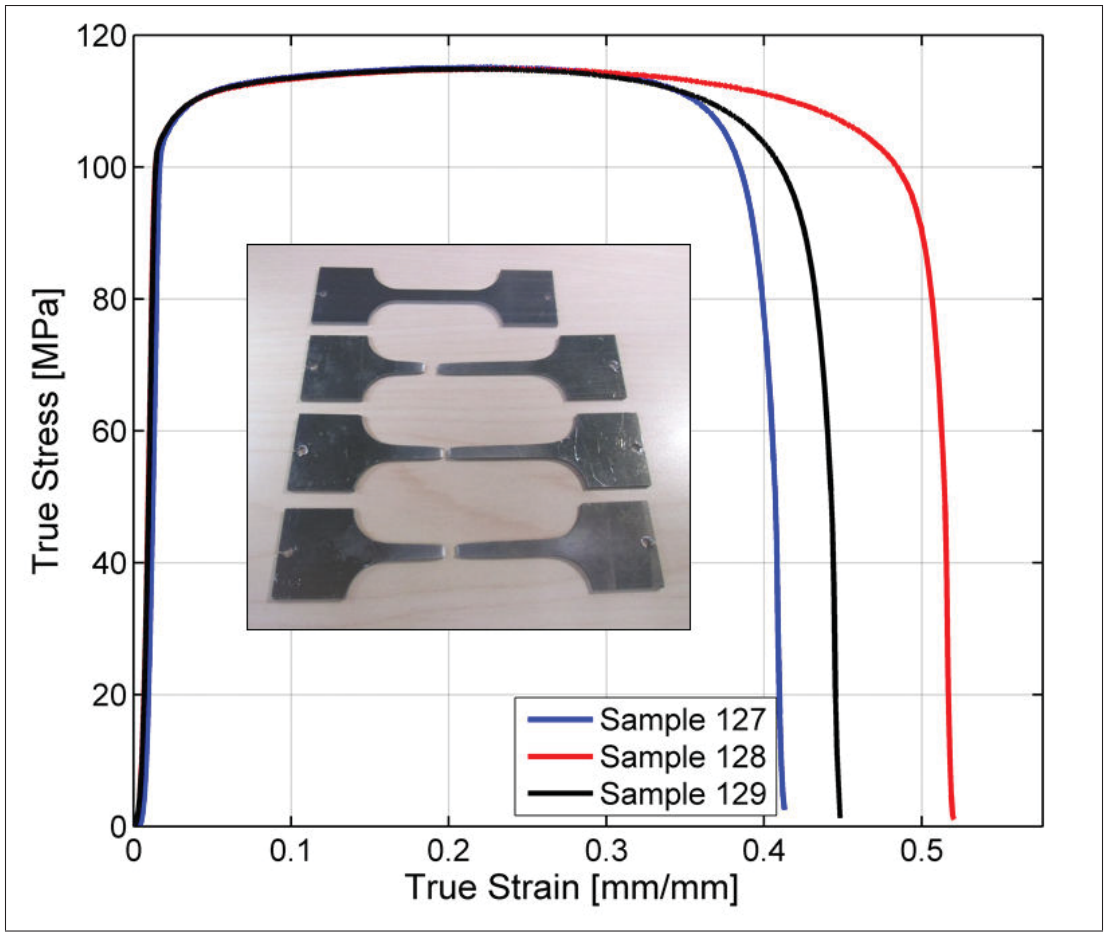

Figure 3.10 True stress versus true strains at 350°*C* showing geometrical instability

3.5 Conductivity and Emissivity

Evolution of thermal properties of AA7075 due to temperature are presented in Figure 3.11.

Changes in emissivity at different temperatures are significant enough to require care if some of these values are used during simulation. It is important to note that these changes are easily obscured when the sheet is sprayed with lubricant. A coat of graphite, for example, yields to an emissivity of around 0.9. Changes in conductivity, however, are not very significant at the forming temperatures. Furthermore, we can observe that as the material reaches temperatures close to the solution heat treatment, the differences between the conductivity of annealed and "as received" material becomes insignificant.

Table 3.3 Young's modulus at different temperatures in laminating direction

Temperatures [$^{\circ}C$]	**Young's Modulus [GPa]**
20	66.9
200	19.3
300	14.3
350	10.6
400	9.85
440	7.81
490	3.67

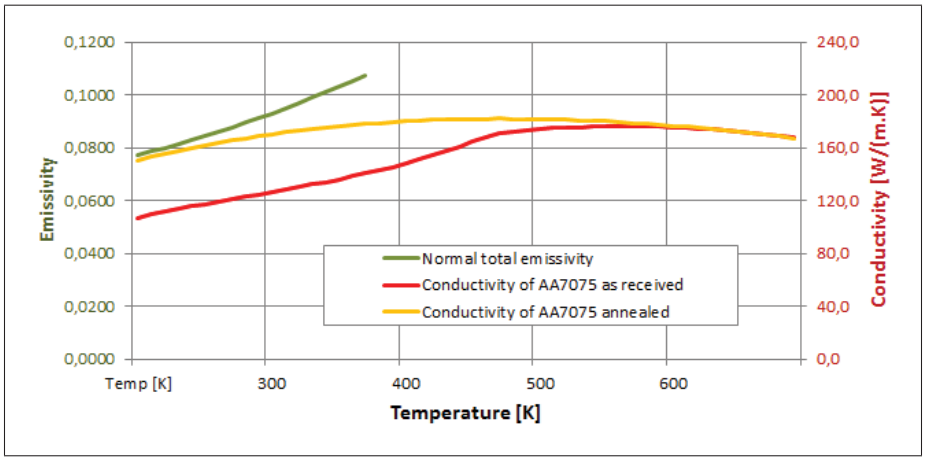

Figure 3.11 Thermal properties of AA7075 at different temperatures (MPDB, 1999)

3.6 Free Convection

As shown by Bergman *et al.* (2011), the coefficient of heat convection is highly variable in gases, ranging from as low as $2\frac{W}{m^2*K}$ in free convection up to $250\frac{W}{m^2*K}$ when forced. During the simulation where a surface is exposed to air, heat flux is calculated by $\dot{q}'' = h_{air}(T_s - T_\infty)$.

To characterise this parameter, a simple simulation of the blank was launched with varying value of h_{air} until the temperature decrease was in concordance with experimental data. This data was obtained via a thermal camera pointing at the aluminium surface coated with graphite.

The observed decrease of approximately $5\frac{^{\circ}C}{s}$ was consistent with the data from other local sources and required a h_{air} of $38\frac{W}{m^2*K}$.

3.7 Thermal Contact Conductance

The finite-difference simulation was able to very accurately reproduce the cooling curve of each specimen. As shown in 3.12, it was of utmost importance to include the time constant of the thermocouple in the simulation. The same time constant that was incremented by 50% earlier was able to reproduce the correct second derivative (curvature radius) of the temperature curve seen at the beginning of the cooling.

Working with specimens subjected to such high temperature variations presented many repeatibility issues. Every slight variation in the course of the test made a great impact on the cooling rates. In the case of the specimen sliding an edge along the surface of the dies during the positioning, the thermocouple closest to the die surface saw an increase in temperature not representative of the whole surface while a section of the specimen was cooler, invalidating the uniaxial simplification in the simulation.

Three improvements are proposed to achieve better results. First, the shoulder should be removed to provide a constant section that could be insulated, correcting the estimated 1% radial heat flux. Secondly, the apparatus should be fitted with and inline piston, allowing the hydraulic press to be controlled by its position at fast speeds while reaching an adequately precise force applied by the piston's compression. This change would help prevent variations in force during the first seconds of contact and reduce the time during which the sample is in contact with only the upper cylinder. Thirdly, the apparatus should be subjected to a better quality control, as a profilometry made after the campaign showed a surface that was not flat. A depression near the center axis, where all thermocouples were located, is likely to have influenced heat flow behaviour. Figure 3.13 shows this defect as well as the changes surface finish at the annular defect mentioned earlier around the 15 mm mark.

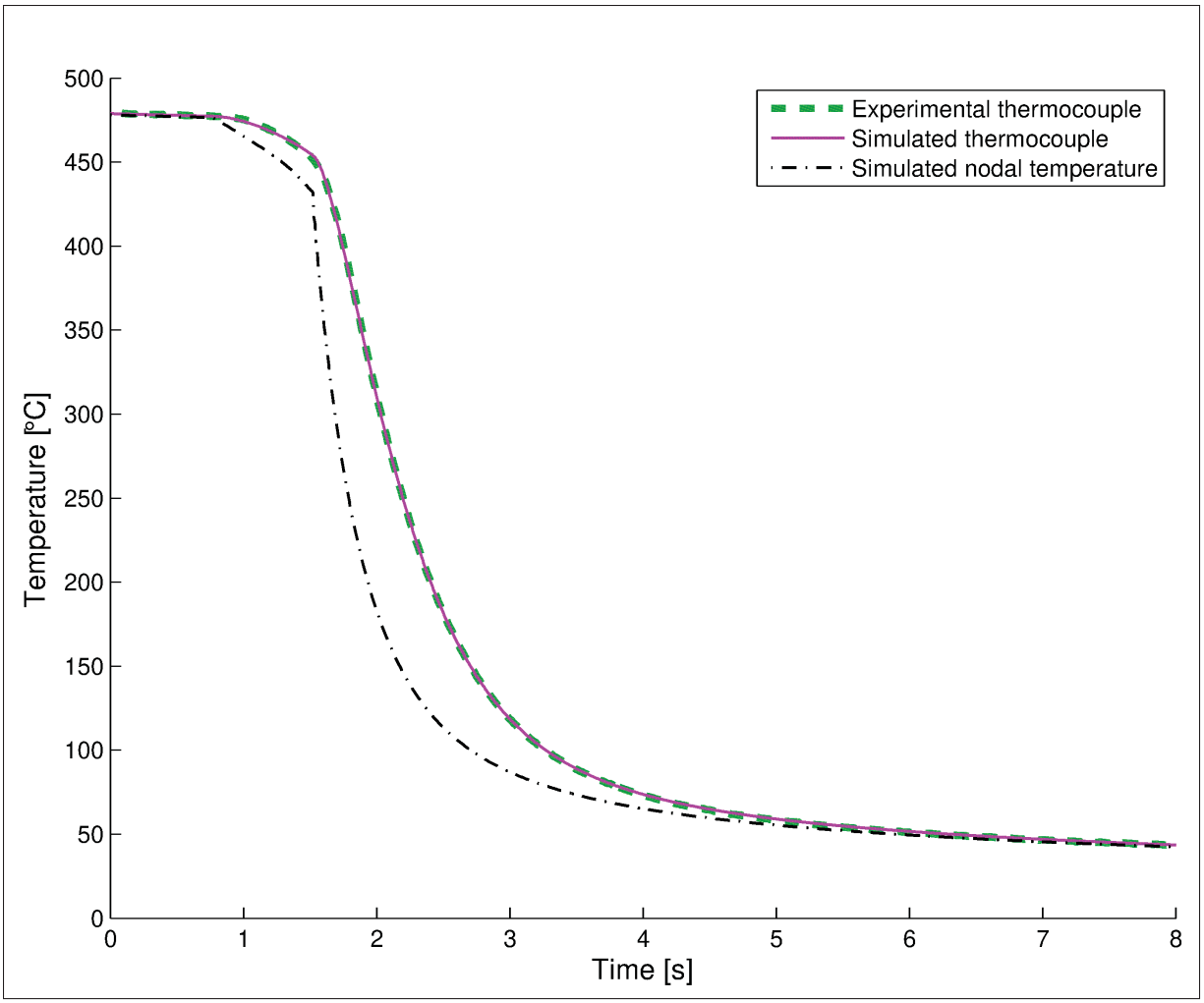

Figure 3.12 Comparison between experimental and theoretical specimen temperatures

The wide variations in the results obfuscated many of the more subtle variations in the results that should have been seen in the different test cases, such as different lubrication and surface finish. The as-machined finish was Ra 0.964 μm while the polished finish was 0.186 μm.

Also, the specimen sometimes developed a visible curvature, making first contact with the dies either near its edges or at its center. Added to that is a some annular deformation on the tools. In Figure 3.14, this is visible both on the tool itself and by the mark it left on the specimen.

A sensitivity analysis of the whole simulation shows that as the contact pressure gets higher, the conductance becomes high enough to have little to no effect on the heat transfer. The relatively

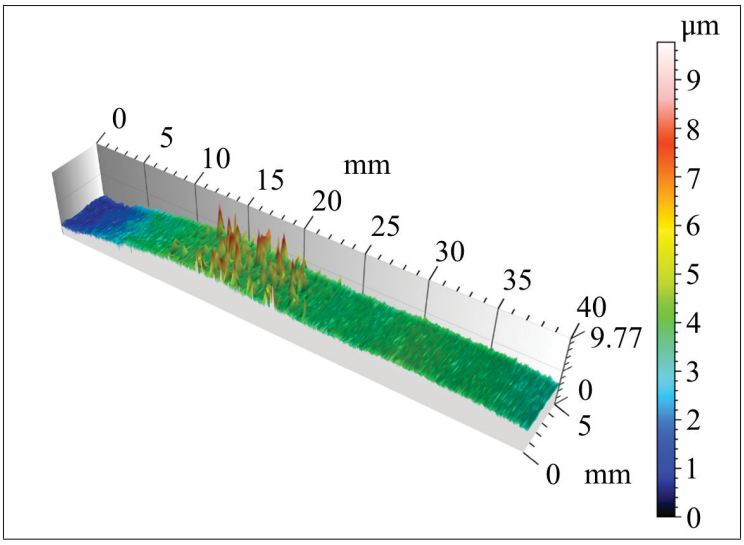

Figure 3.13 Profilometry spanning from 5 mm from the center axis extending radially on the surface of the heat transfer apparatus

low diffusivity of the steel then becomes the main driving factor of the heat propagation. For this reason, the curve fitting was done with a linear function from 0 MPa to 1 MPa and another line was traced for all values above. The results are shown in Figure 3.15.

Contact algorithms in the FEA software use two thresholds at which the thermal exchange definition changes. Above the first distance, L_{max}, there is no heat flux between the surfaces. When closing in, between L_{max} and L_{min}, the heat flux is calculated with:

$$h = \frac{k_{air}}{\Delta x_{gap}} \quad \forall \quad L_{min} \leqslant \Delta x_{gap} \leqslant L_{max} \tag{3.1}$$

Seeing as the value of h could tend toward infinity for very small values of L_{min}, it is important to cautiously choose this value. Moreover, a value too large would induce a full contact conduction where the surfaces are still apart. This is especially important in hot stamping simulation where the surfaces may be arranged in a similar fashion as presented in Figure 3.16 below. This will also be of importance in future sections comparing the cooling rate of the flat sections measured by Eddy Current Testing (ECT) on the part.

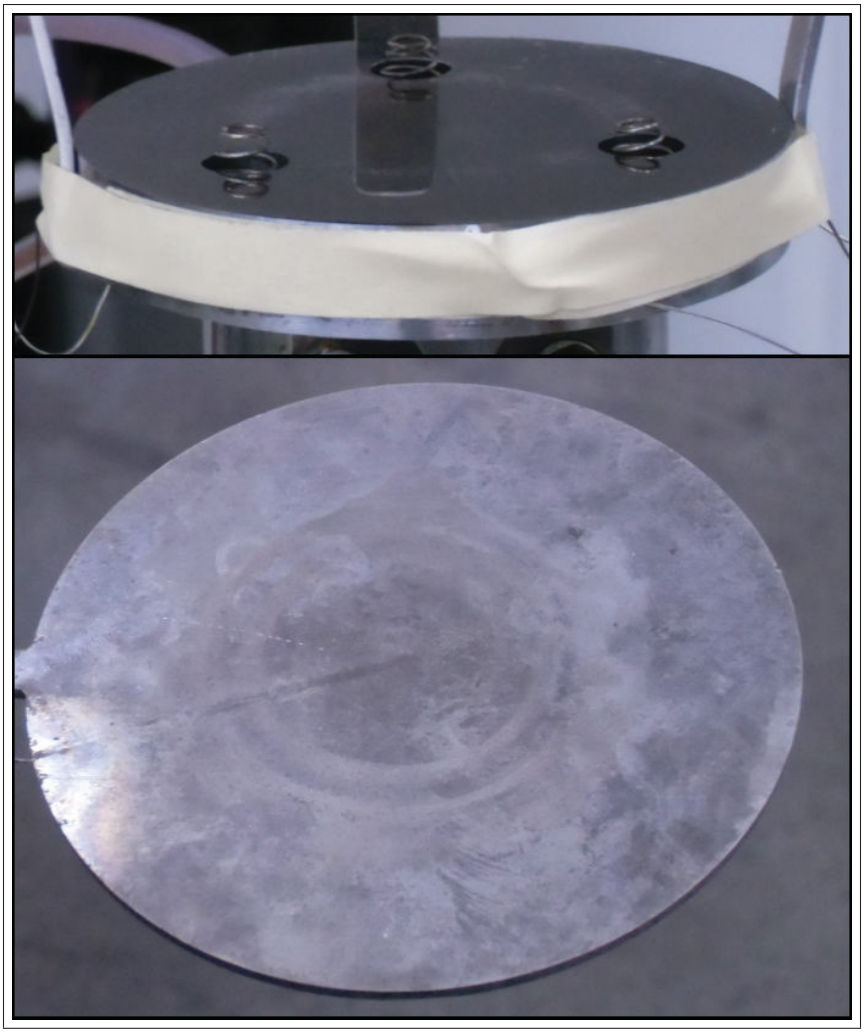

Figure 3.14 Annular wear and corresponding marks on the specimen

The value of k_{air} goes from 0.025 $\frac{W}{m.K}$ at 20°C to 0.055 $\frac{W}{m.K}$ at 490°C (Pardee, 1987). However, due to the effects of local convection and radiation, a value of 0.075 $\frac{W}{m^2.K}$ encompassing all phenomena was found to give the best results. To ensure continuity in the $h_{contact}(P)$ function, the value of $h_{contact}(0)$ is set to 400 $\frac{W}{m.K}$ and the L_{min} is set to 0.188 mm. All the inverse modelling described in the methodology section is made with this fixed initial value. A summary of this is shown in Table 3.4.

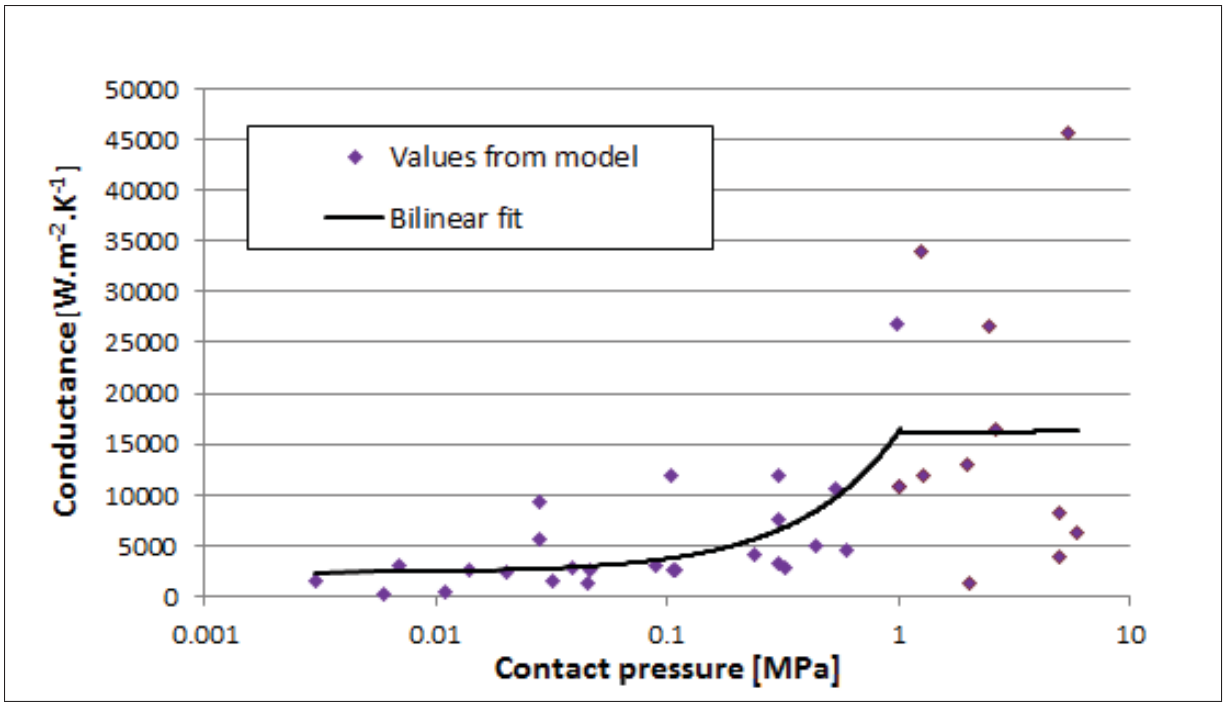

Figure 3.15 Contact conductance values obtained from inverse modelling

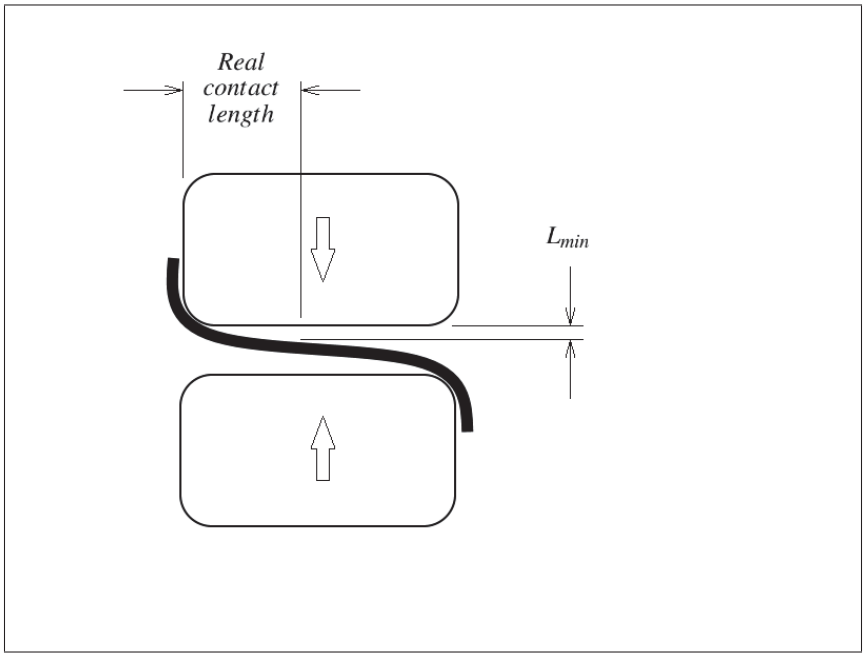

Figure 3.16 Effect of L_{min} on thermal contact behaviour

Table 3.4 Contact thermal conductance summary

Contact Pressure [**MPa**]	**h** $\left[\frac{\mathbf{W}}{\mathbf{m.K}}\right]$
Gap	$\frac{k_{air}}{\Delta x_{gap}}$
0.0	400
1.0	16 000
1.0e+06	16 000

3.8 Microstructure

Verification of the microstructure in aluminium requires special equipment since the η precipitates and its precursors (η' and η'') are too small to be distinguished with conventional microscopy. An alternate method, Eddy Current Testing (ECT), will be used. As the precipitates change, there is a corresponding change in electrical conductivity that is measurable. It was identified in AA7075 by Staley (1974), albeit more in the context of ageing time and changes in yield strength. These measurements are still relevant as the changes in yield stresses are mostly due to changes in precipitates. Readings are made by a calibrated instrument that measures the material's response in phase and amplitude to a magnetic field oscillating at 60 kHz. According to the equipment's manufacturer, this should give a depth of reading at approximately 0.33 mm. The use of this instrument requires a flat surface of a diameter of at least 10 mm to have repeatable results as the probe would otherwise include the measurements of the air gaps in the reading.

Due to the comparative nature of these kind of measurements, is it necessary to establish benchmark values. Each value in Figure 3.17 was obtained by a minimum of 10 readings on at least 5 different specimens. They were heated to SHT for 18 minutes, removed from the oven, held in still air and quenched in water after a specific delay.

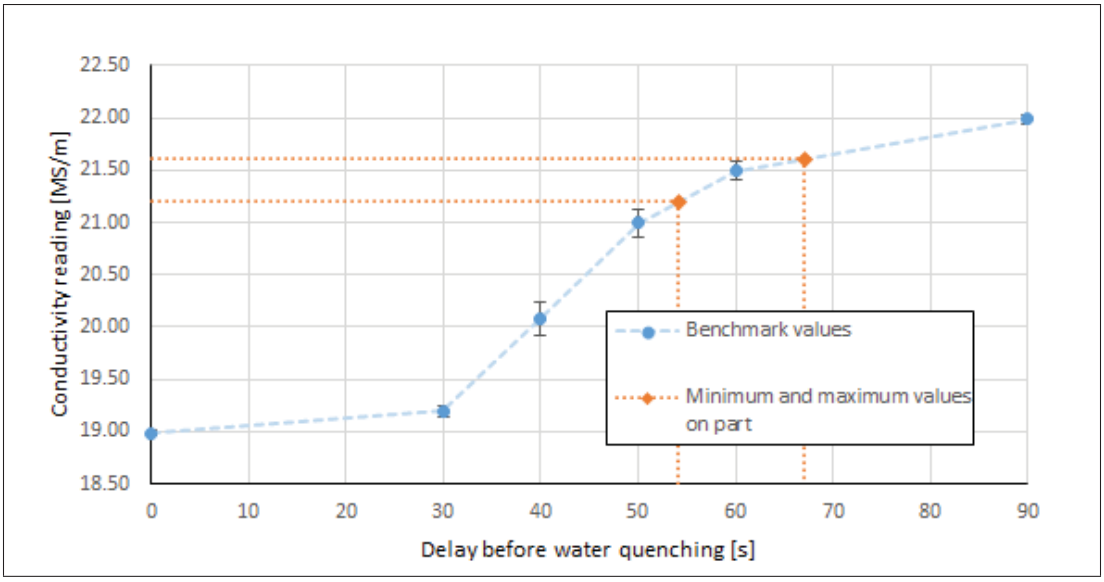

Figure 3.17 Comparison of electrical conductance readings in megasiemens for specimens and experimental part

It is likely that most of the unwanted precipitate formation happens mostly between 30 s and 60 s of the removal of the specimen from the oven. This is somewhat supported by the fact that the norm MIL-H-6088G (US , 1991) requests a delay of no more than 20 s.

3.9 Commparison of prototype and FEA

The success of a hot stamping operation in the present case is determined by the part geometry being inside the tolerances and the resulting metallurgy being adequate for the following artificial ageing heat treatment. Verification of the simulation will focus on these two parameters.

3.9.1 Geometry

Presence of a crack makes the evaluation of the final thickness at the 3D corner a challenge, especially without an adequate damage model.

For this reason, an uncracked part is presented even if it was failed. An offset in initial positioning of the blank of about 2 cm to the left allowed better material feed to the 3D corner.

However, with this positioning the forming step also caused two folds to appear, preventing full closure of the dies. The FEA was able to recreate these folds but stopped when the elements in the fold were too distorted or caused issues in contact handling.

Figure 3.18 shows the aforementioned specimen that was cut to allow for the measures to be taken with a point micrometer. Significant veiling is also visible and was also due to too much space remaining between the dies. Figure 3.19 shows the thickness along the measured profile with some different FEA results.

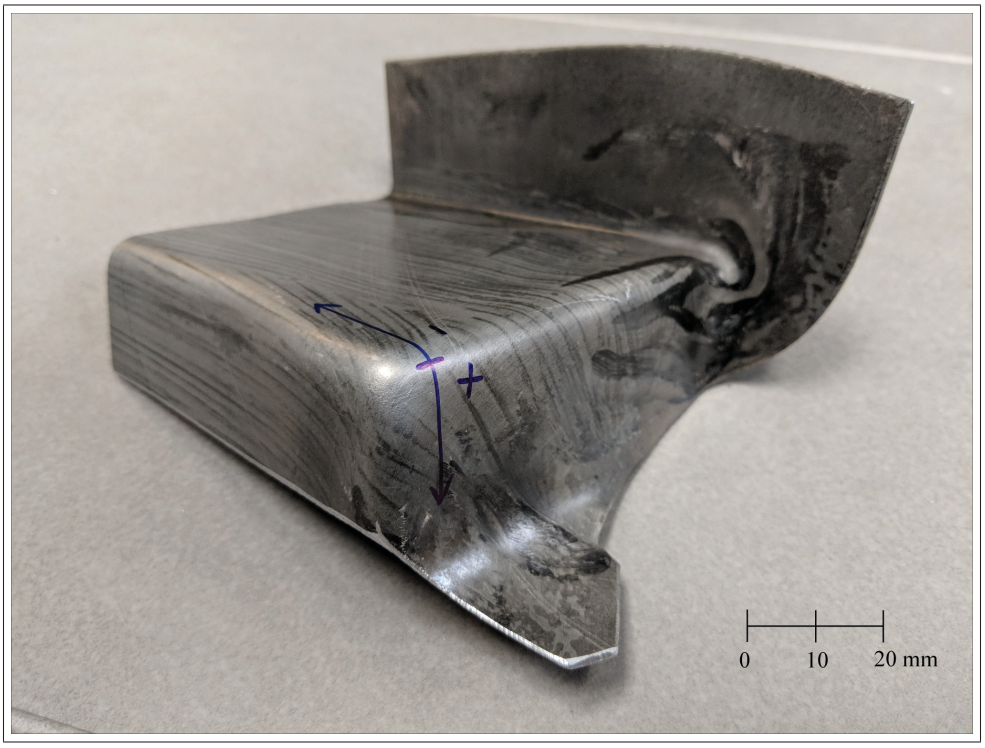

Figure 3.18 Measured profile along the corner of an undamaged part, material from a different manufacturer

A quick look at FEA results show that it was not able to recreate real thinning behaviour. Shell elements have a tendency for strain localization, which is the main problem observed.

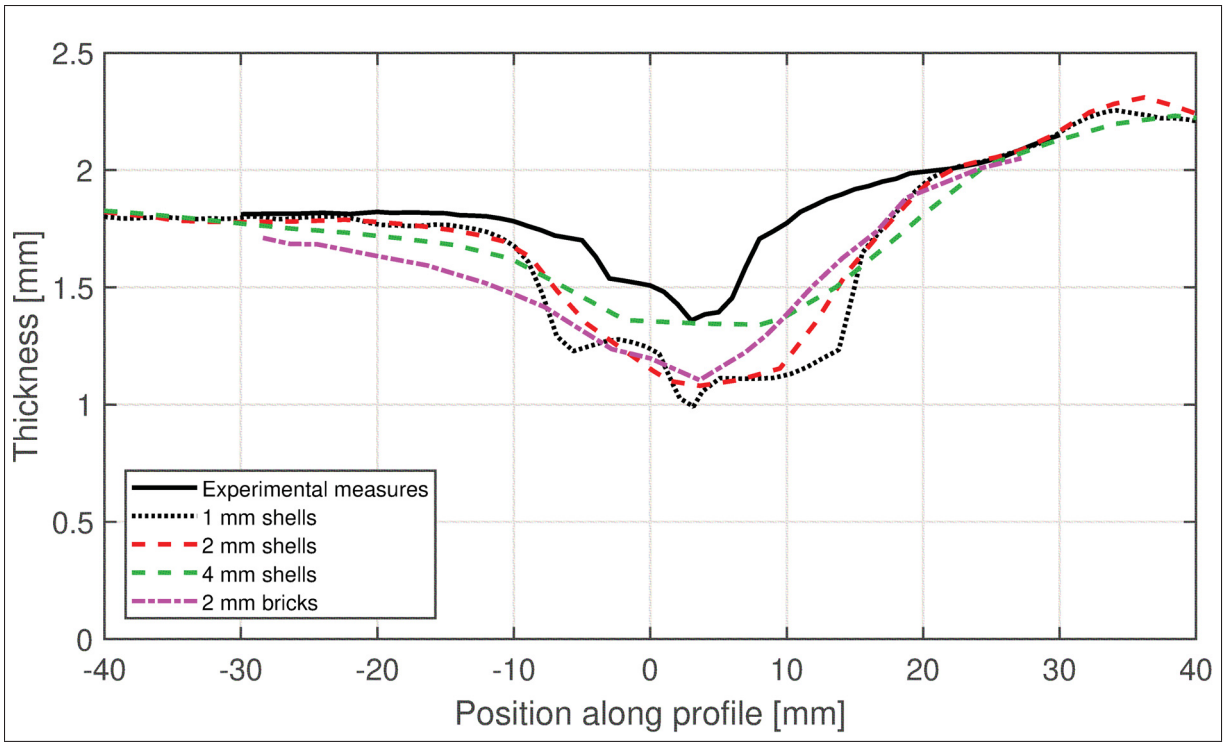

Figure 3.19 Comparison of thickness profile at 3D corner with different FEA approaches

Brick elements showed a maximum thinning similar to the other 2 mm and 1 mm shells but a lack of anisotropic behaviour probably explains the imprecision in thinning around the corner, as in position -28 mm to -10 mm.

Only one of the 2 folds was recreated with the 4 mm mesh, the one near the corner being too small for the size of the element for a correct representation of the behaviour. These larger shells allowed for less localization of thinning but also caused an issue in die closing, being unable to conform to the dies' geometry on small radii.

Although the scale was off, the 1 mm mesh showed a very similar thinning distribution to the real part. As seen in Figure 3.18, there is an orange peel-like finish on the corner showing that damage had occurred. This could explain the difference in thickness if the real part had an apparent volume gain due to voids appearing in the material whereas the FEA elements had a constant volume.

Finally, the 2 mm mesh showed an average thinning very similar to that of the 1 mm mesh with a very significant reduction in calculation time. It is hypothesized that overall behaviour is best represented by a 2 mm mesh and refinement should be used for difficult locations, if necessary.

Overprediction of thinning might also have been caused by the fact that the friction behaviour might not be perfectly recreated at this location. Samples show signs of abrasion by the dies' surface, suggesting higher contact force and less lubrication. However, in the FEA, friction is constant over all surfaces. Areas further out from the center show a better agreement between FEA and experiments, especially with the 2 mm and 1 mm mesh. This good agreement extended to all other areas on the part that could be measured.

An error on this profile may also have been caused by the installation of the dies in the hydraulic press. They were held tightly against an insulating panel but there were still small lateral degrees of freedom. This may have caused the dies to not be perfectly aligned thus creating a gap at the vertical sections, where thinning was observed. In this scenario, thinning would have also been aided by a lesser diminution of temperature at this location due to lack of contact.

On simulations with and without the folds, veiling patterns in the experimental specimens were all faithfully recreated in the FEA. Peaks and valleys amplitude were dependent only on final closure of the dies, in both the FEA and in experimental parts. To recreate the results, it was necessary to iterate between different final closure gaps followed by springback analyses.

3.9.2 Temperature history

At the time of writing, the dies were not instrumented to adequately measure the blank's temperature during the stamping operation. Since the goal of measuring the temperature is ultimately to ensure that the part has been quenched by the end of the process, an indirect verification of the microstructure may, in this case, replace this step. This is done by ECT measures that are compared to benchmark values obtained earlier during the thermal characterization steps. The locations at which the measures were taken are shown in Figure 3.20.

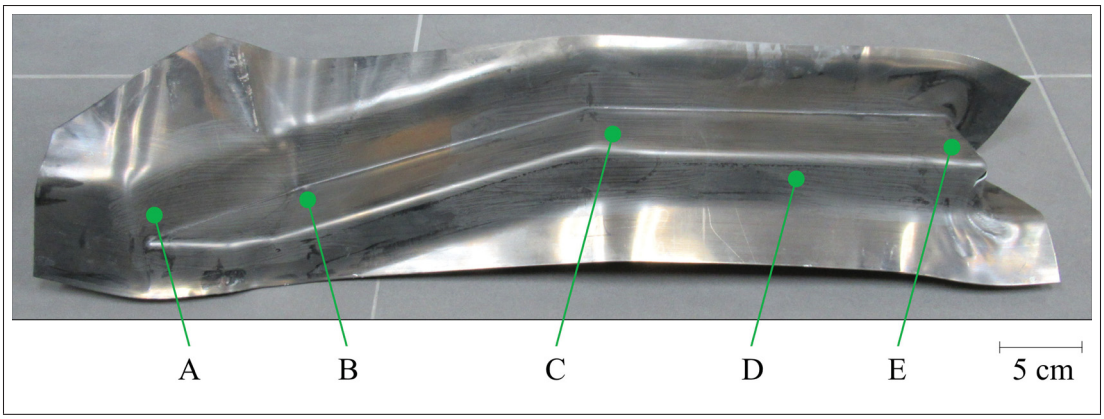

Figure 3.20 Locations of conductivity measures

Measurements were taken on the top side (visible in the figure) and on the underside. There were small but sometimes significant differences in the measurements, likely caused by a difference in an initial contact on only one side or a simultaneous contact on both sides. Table 3.5 relays the data.

Table 3.5 Electrical conductivity measures on formed part

Location	**Top side [S/m]**	**Underside [S/m]**
A	21.1	21.4
B	21.5	21.5
C	21.4	21.5
D	21.5	21.1
E	21.6	21.6

When compared to measurements taken in Figure 3.17, we see that these values show a heat treatment equivalent to a wait time of approximately 60 seconds before the quench. This would indicate an inadequate microstructure since it exceeds the maximum time specified by the standard ASTM B918-01 AST (2001), namely 10 seconds. Further investigation is deemed necessary. An inadequate SHT and quench results in η precipitates instead of the required η'' or η'. Normaly, η' precipitates allow for maximum strength and η'' can be converted to η' via

an artificial ageing treatment. The temperature history of those same points in the simulation are shown in Figure 3.21.

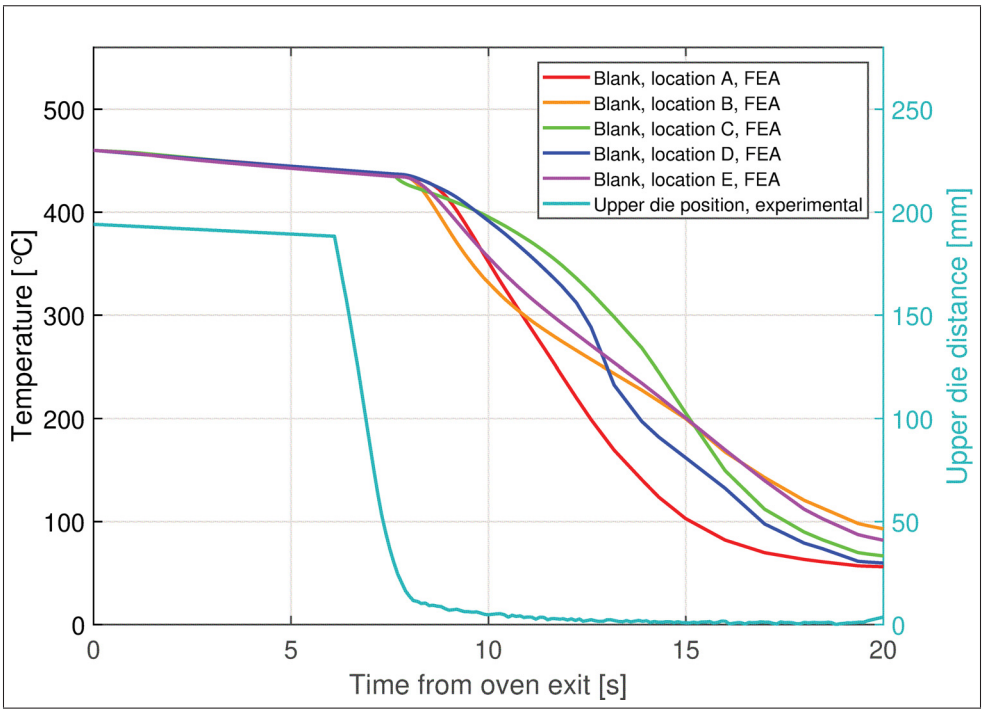

Figure 3.21 Temperature profiles at locations A to E

Differences in the expected and real measures might have been caused by residual stresses in the part. An increase in conductivity was observed by Chang *et al.* (1996) after a shot peening treatment on AA7075. This phenomenon could explain at least part of the variation. Samples measured for comparison had no residual stresses. It is also possible for the temperature profiles to have been negatively influenced in the simulation by the thermal contact definition, as shown in Figure 3.16. Since the η phases and their precursors (η' and η'') are still evolving at the temperatures at which the part is removed from the dies, it may also be that some artificial ageing has begun and also influenced the conductivity.

Compliance to norm ASTM B918-01 AST (2001) requires a maximum delay before quenching of 10 s for a 2 mm thick aluminium sheet and it should be submerged in a fluid at a temperature

lower than 43 $^{\circ}C$. The current part's cooling cycle should not result in a successful SHT and quench according to this norm.

For the reasons mentioned above, the cooling seen in the simulation is considered valid within the error range expected from ECT measures.

3.10 Parameters Studies

3.10.1 Effects of a Full Die Mesh Versus a Thickened Surface

A simple extruded surface mesh to represent the dies is often used as a way to simplify and accelerate the FEA. In the present case, the temperature distribution throughout all the die is important and will also be used for an analysis of the production cycle.

It was first necessary to ensure that a geometrical simplification of the cooling channels would not affect the results. Since it is mush easier to mesh a flat surface than around the channels, the following section will investigate the effect of replacing the real channels' geometry by a flat surface.

With this goal in mind, a comparison was made between two simulations of steady state heat transfer. Although a transient heat transfer case would have been interesting, the many different cases seen in the dies would have made for a difficult comparison. An arbitrary temperature difference of $100^{\circ}C$ was chosen for easy visualization. Any other number would have yielded the same results since only the gradient is important in this case.

Temperature inside the cooling channels was assumed to be at a constant temperature. A simple calculation tells us that this assumption is fair since the energy that needs to be evacuated to completely cool the blank from its initial temperature is easily evacuated by the cooling unit.

The total energy to dissipate is:

$$E = \rho V C_p \Delta T = 2700\,[\frac{kg}{m^3}] \cdot 0.00101\,[m^3] \cdot 1.03\,[\frac{kJ}{kg}] \cdot (490\,[^\circ C] - 20\,[^\circ C]) = 1320\,[kJ] \tag{3.2}$$

The cooling unit has a capacity of 160 kW which should allow it to cool the blank in approximately 8 seconds with perfect heat transfer, as shown in:

$$1320\,[kJ] \,/\, 160\,[kW] = 8.25\,[s] \tag{3.3}$$

We know that most of the blank's cooling happens in the first second of the contact however this effect is mitigated by the much slower diffusion of the heat through the steel.

Two FEA looked at the heat transfer in a 50 mm wide section of H13 steel similar to the one shown in Figure 3.22. The first one has ø 9.5 mm cooling channels with their center axis at the 50 mm mark from the heated edge. The second one is only a square sample 50 mm wide with edges temperatures set to the same $100^\circ C$ and $0^\circ C$. The temperature profile was extracted as the node temperature versus their distance from the left heated edge. The second line in Figure 3.23 shows the straight surface at the 50 mm mark. From 45 mm to 50 mm, the temperature values from the test with cooling channels are somewhat less representative due to the decreasing number of nodes used for the average temperature profile.

The simplified surface, with its constant temperature gradient, showed a heat flux of 38 W constant throughtout all its width. In Figure 3.22, we can look at the heat flux from the heated surface to the cooling channels. We can see that the simplified geometry should be an adequate replacement for the full channels' geometry if the cooling channels are at least 15 mm from the surface, which is the case for the dies used in this project.

Figure 3.24 shows the difference between the extruded and full volume meshes for the dies. Both begin with brick elements successively 1 mm, 2 mm, 3 mm and 4 mm thick. The full volume mesh has a surface that links the center axis of all the cooling channels.

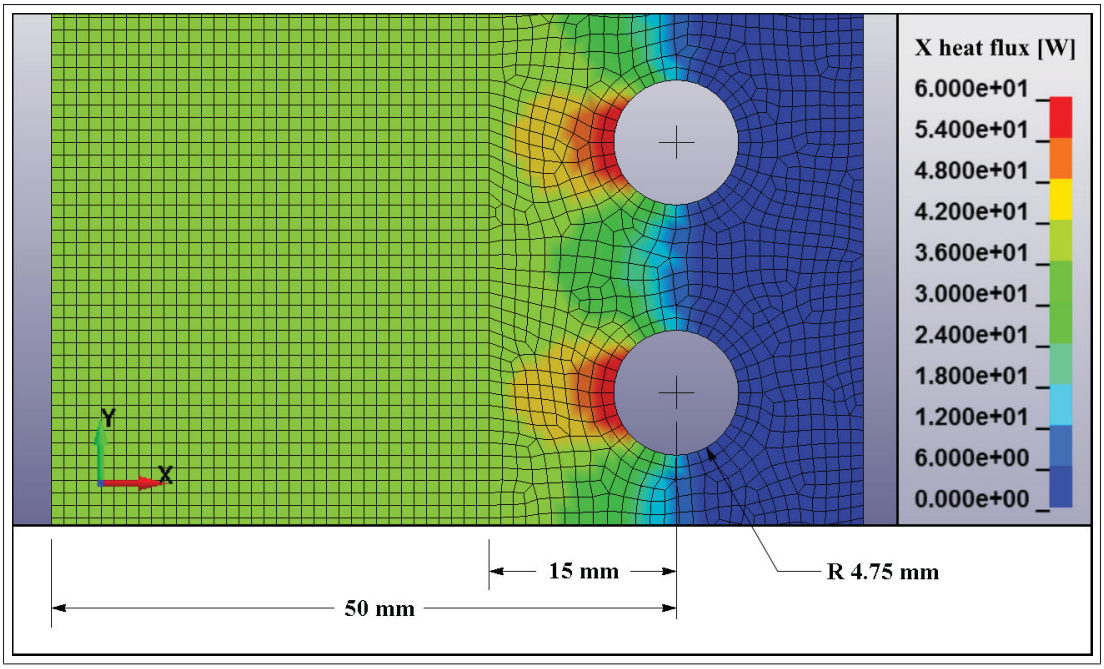

Figure 3.22 X heat flux around the cooling channels

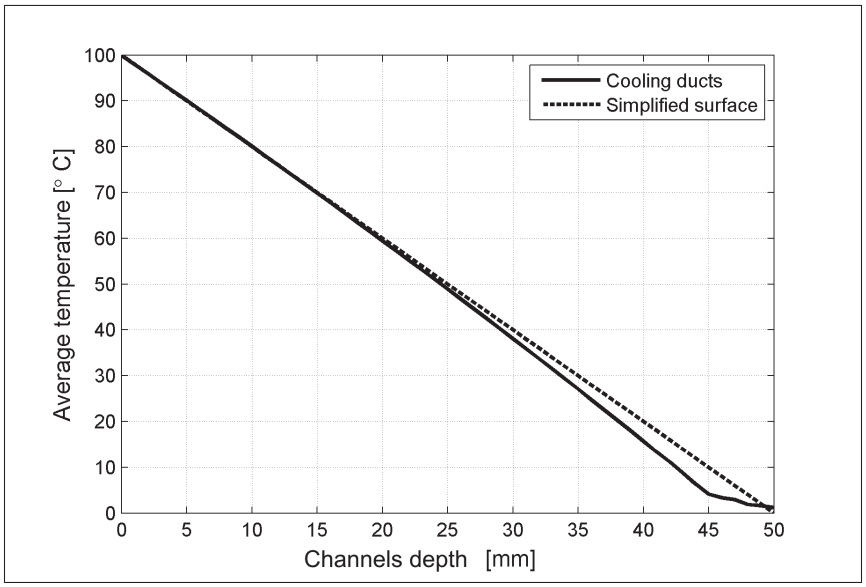

Figure 3.23 Comparison of temperature profiles for 50 mm section with cooling channels or simplified surface

A simulation was made to determine if results diverge between the two strategies and if so, under which conditions it does happen. Figure 3.25 compares the temperature distribution of the sample at 10 seconds after the beginning of the dies' movement.

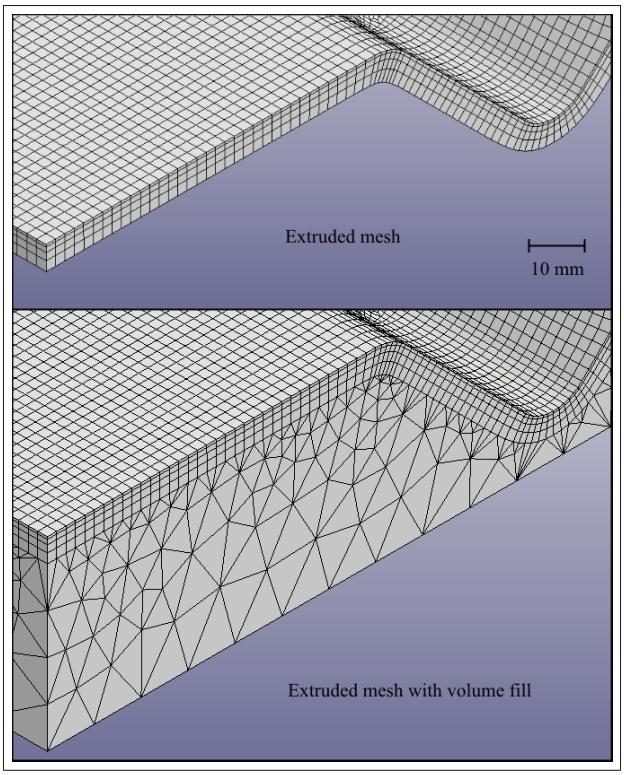

Figure 3.24 Comparison of mesh types for die cooling study

At that time, there is already a difference of 25°C to 45°C at the locations with the highest temperature. Despite that, the added cooling did not seem to have particularly affected the distribution of cold and hot regions.

A second investigation is made to determine at what point there is a divergence between the two models. Figure 3.26 shows the temperature history at different depths during the forming process while Figure 3.27 shows where those measures were taken.

Differences between the two models happen mostly at greater depths. At location A, there is approximately 29 mm from the surface to the cooling channels. At location B, this distance is 67 mm. The fact that the divergence is roughly similar at both location shows that this difference is more likely caused by the added heat diffusion through the added material than losses towards the cooling channels. Later in the cycle, the cooling channels are expected to have a more appreciable impact, as the heat finally reaches them and is evacuated

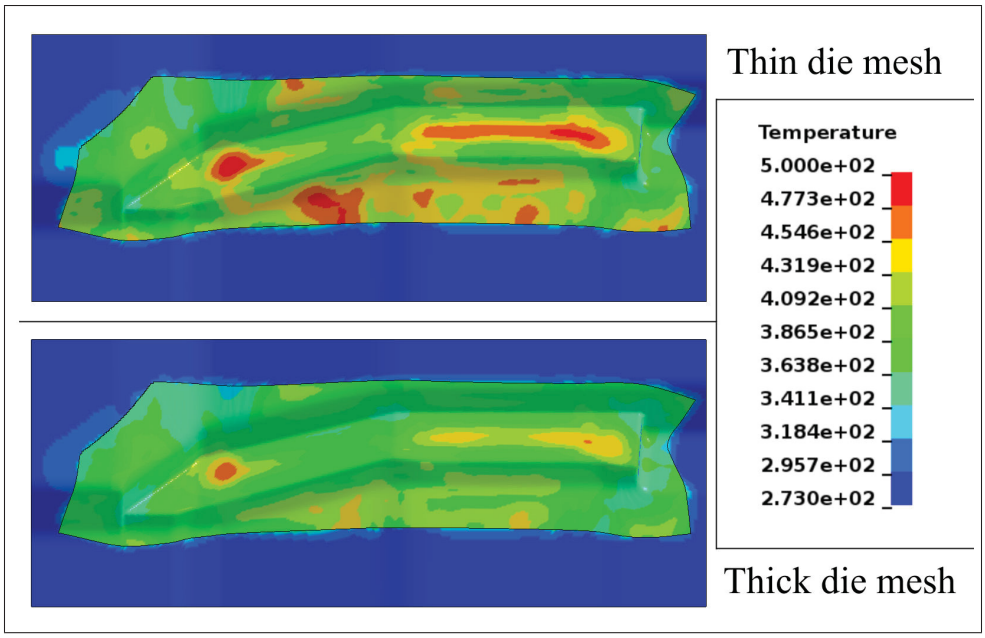

Figure 3.25 Comparison of mesh types for die cooling study

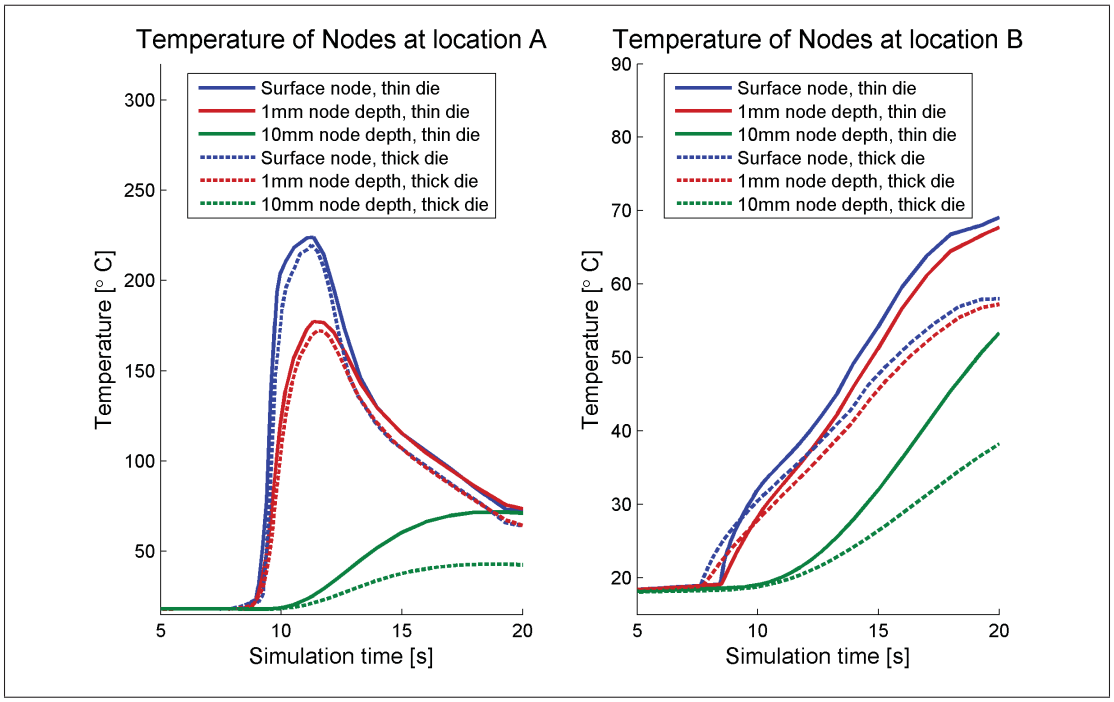

Figure 3.26 Comparison of temperatures at varied depths in different die meshes

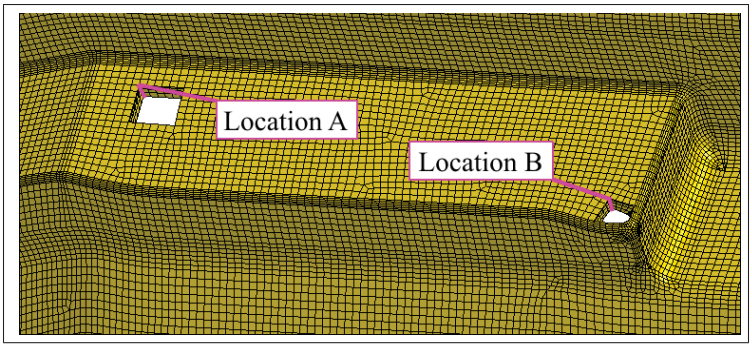

Figure 3.27 Location of measures in Figure 3.26

3.10.2 Effects of Changes in Initial Blank Temperature

Initial temperature of the blank was only estimated from the delays and the cooling rate observed on aluminium sheets in similar conditions. It is important to see if an under- or over-estimation of this value could significantly affect the simulation. For this purpose, the same simulation was launched with the blank at -20°C and +20°C from the best estimation of temperature.

The blank's temperature is considered constant in all of the blank's volume at the time of insertion in the blank. Indeed, the very small thickness to area ratio ensures that the edges have no significant impact on the heat distribution. This is the temperature that is changed in the trials below. Once the part is inserted in the dies and waiting for them to close on one another, however, there is local cooling at the edges and in the center of the 3D corner where the blank touches the dies. This is unfortunate since it cools the blank where the highest formability is required. This issue is discussed in more detail in Chapter 5, where improvements to the existing tooling are discussed.

When most of the strain happens, corresponding to seconds 7.5 up to 8.5 s on Figure 3.28, the difference in initial temperature is still visible at location E. At the crack location, this difference is less evident due to the very high initial cooling rate.

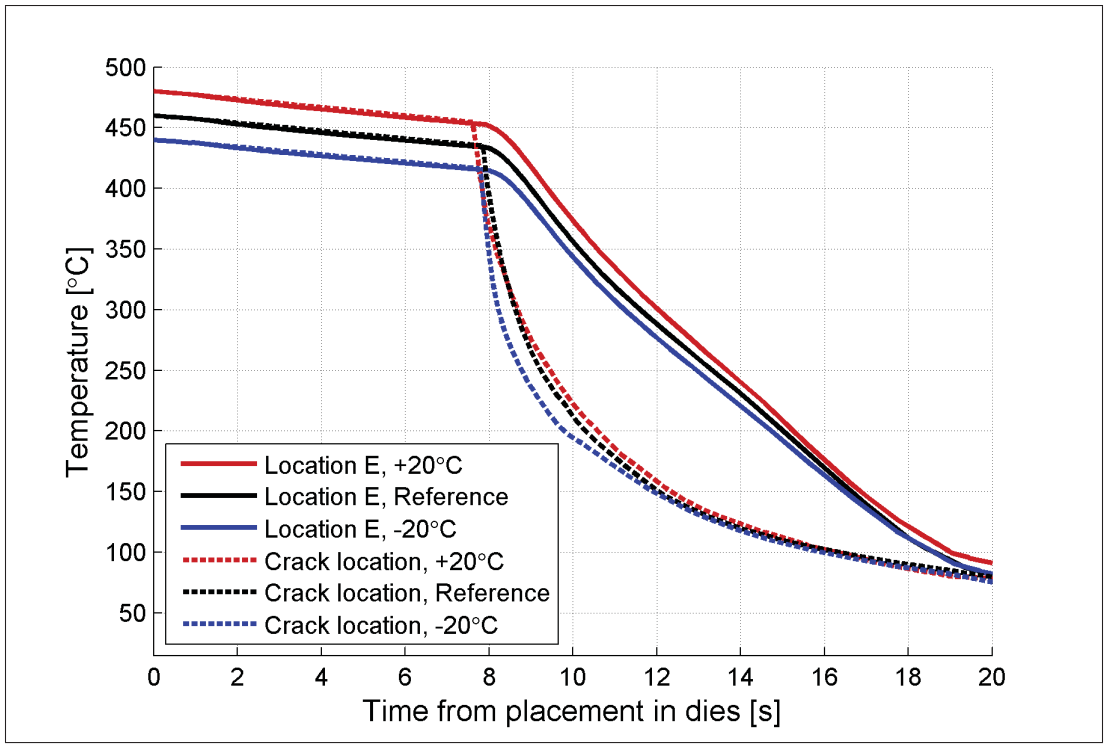

Figure 3.28 Comparison of temperature profiles with different initial temperatures

The only observed difference in strain behaviour is the localization of the necking at the 3D corner. With the +20°*C* initial temperature case, necking was visible higher on the apex of the 3D corner. In the -20°*C* case, the necked section was lower on the side, closer to where the crack tends to appear in the experiments. This would suggest that the initial temperature estimate might benefit from being slightly lowered, although other phenomena discussed later could have caused the same effect.

3.10.3 Effects of Damage Model Addition

The ruptured face seen on the reference in Figure 3.29 is very similar to the one observed at 200°*C* in Figure 3.9. There is a similar 45° angle, surface finish and a small necked region is visible around the crack. This suggests a damage mechanism of grain boundary sliding, different from the void nucleation and growth typical of higher temperatures in AA7075.

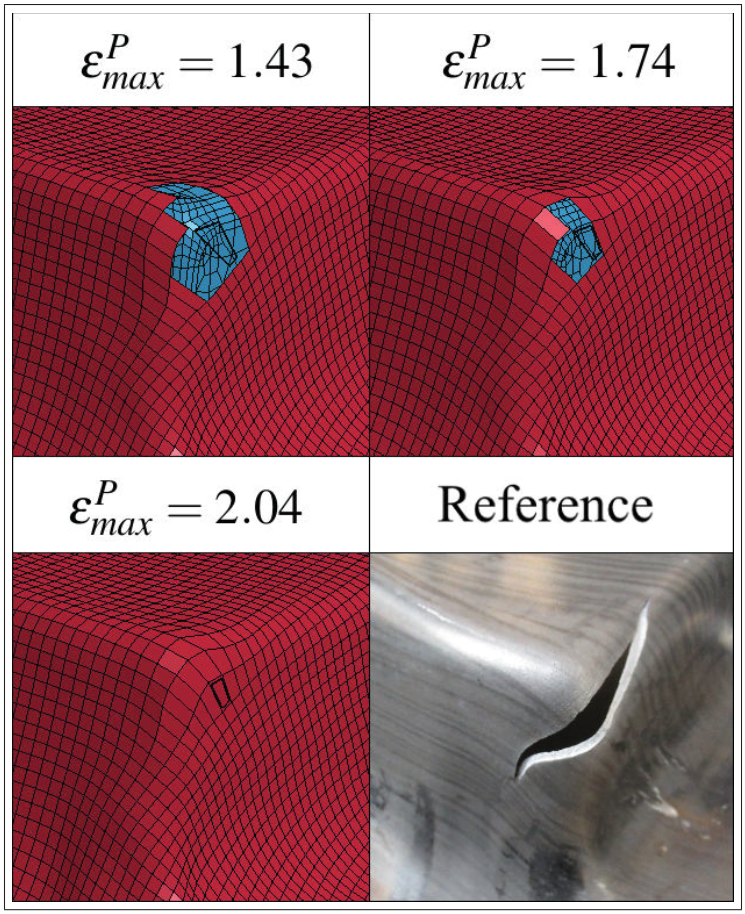

Figure 3.29 Comparison of three different maximum strains at 3D corner

As seen in Figure 3.6, the damage model using the 1.74 maximum strain was able to predict the initial break at a temperature cromulent with the observed fracture surface type. However, all damage models have failed to recreate the crack propagation. The lack of precision beyond the initial break is likely to be caused, at least in part, by the suppression of the elements instead of their separation. Although out of scope for this project, some workarounds can be used such as using multiple shell layers locked together. It should be noted that only the deviatoric strain in the element is used for the evaluation of the damage, eliminating some potential effects of compression by the dies and thermal expansion effects.

It was possible to find the initial damage strain for this particular case but special care should be taken in an eventual predictive application. If used in a predictive fashion to design a process,

Table 3.6 Review of elements status at break

Maximum strain (ε^P_{max})	**1.43**	**1.74**	**2.04**
Time of break [s]	7.96	11.4	No break
σ_{xx} [MPa]	109	327	350 at 17.8 s
σ_{yy} [MPa]	107	269	425 at 18.7 s
ε^P	1.43	1.74	1.86 at 20 s
Thickness [mm]	0.67	0.48	0.42 at 20 s
Temperature [$^\circ C$]	387	161	80 at 20 s

the damage model would have to be applied after a full forming has been simulated to check that no maximum strains have been reached at each of the temperatures. A better methodology would be to use a cumulative damage model that includes the continuous damage added at each increment of plastic strain and temperature as well as any recovery phenomena that could occur.

3.10.4 Effects of an Alternative Material Model

Figure 3.30 was taken at the timestep with the maximum stresses, when the dies are at their closest. There are differences in values at certain locations but also variations in the distribution.

The maximum stresses obtained with the Hill constitutive law are probably due to a smaller expansion of the yield surface. In Figure 3.6, it is possible to see that in cases of equibiaxial stresses, there is greater room before there is an expansion of the yield locus, allowing for a smaller evolution. This would have the effect of limiting equibiaxial strains by keeping them in the elastic domain, spreading the strain over a larger region rather than having a localization. However, the Hill model showed a less accurate prediction of the anisotropic behaviour at the 3D corner, showing an almost equibiaxial strain in the region near the crack.

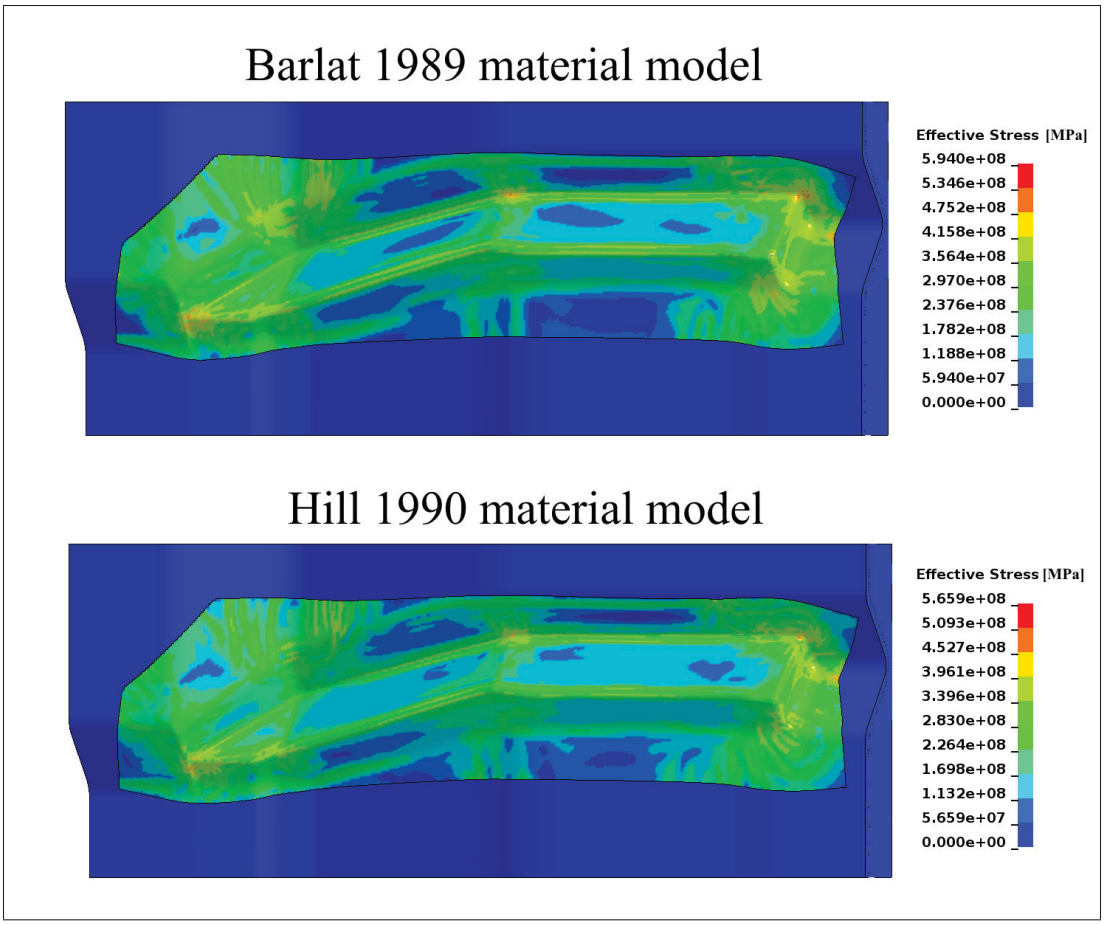

Figure 3.30 Von-Mises stresses at their highest during forming operation

3.10.5 Effects of Different Blank Meshes

Shell elements rely on different physical and mathematical assumptions for their behaviour in their normal axis. Although they provide an invaluable tool for minimizing computational load, they can induce errors. One such error is the lack of normal stresses, especially since contact pressure can be significant in sheet forming operations. This is especially true in some particular cases such as corners with a small radius.

For all comparisons below the 2 mm blank mesh is used as a reference. Different attempts of the same simulation were made with different meshes for the blank. A 1 mm blank mesh proved to be exceptionally computationally expensive and to achieve a comparison at the 3D corner, local mesh biasing from a 2 mm mesh base was used. It should allow for the same boundary

conditions around the inspected region. Figure 3.19 shows great variations along this profile, caused by important strain localixation. It is suspected however that this mesh would be more suitable for a damage model since less material would be lost by element deletion. It would also likely enable a better recreation of the crack propagation and simultaneously reduce strain localization.

A 4 mm mesh reduced the effects of strain localization but came with a different caveat. Due to the size of the elements compared to the corners of the parts, some elements at the apex of fillets had great penetrations in the dies' mesh. These penetrations caused higher than normal contact forces, changing thermal behaviour and drastically increased computation time of the contacts. A contact formulation based on the nodes of the blank and segments of the dies' surfaces instead of segment to segment would help alleviate this issue, however thermal contact would be affected.

It was observed in a discussion of the damage model that an effective plastic strain of 1.74 recreated the best possible crack initiation. Since we can observe that there is too much thinning even in the mesh with damage, it is possible that a correct damage model would predict break at a lower strain with less thinning.

Finally, as suggested in (D'Amours *et al.*, 2007), a layered brick mesh was used. Brick elements were extruded from the 2 mm mesh with two layers of 0.5 mm on each side. Commercial software was unable to use anisotropy coefficients in its material model but hardening curves were the same as for the shells. Even with this method, local over thinning was not avoided and its location was again much too near to the apex of the radius compared to experimental data. That, plus the impossibility of using anisotropy parameters made the brick mesh a non-contender.

CHAPTER 4

DISCUSSION ON IMPROVEMENTS FOR INDUSTRIAL APPLICATIONS

In this chapter, several improvements are suggested for the production process. The most realist and practical ones are then implemented in a simulation to assess their effects.

4.1 Tooling Changes

In the context of an industrial production, the cycle does not allow for a full cooling of the dies between each operation. The process is optimized with higher die temperatures in mind. The BS part in this project was made 9 minutes after the last one, allowing for near zero temperature gradients inside the dies. In an industrial setting each stamping, quenching and cooling should be done in approximately 20 s for adequate economic viability. In a steady state production, there should also be a continuous heat evacuation.

To reach maximum efficiency for heat evacuation, cooling channels should be as near the surface as possible without compromising structural integrity. Also, it is now known that heat flux becomes uniform at approximately 15 mm from the center to the surface in the case studied in Figure 3.22. In a steady state case of heat transfer, equivalent conductance through H13 steel is shown as a function of its thickness (Figure 4.1). This graph should be viewed as a rough guide only of the heat exchange as the heat transfer case is transient. Most of the quenching is done via an initial absorption of the heat in the outermost layer of the dies followed by a much slower diffusion of the heat towards the cooling channels.

Still, influence of the depth of the cooling channels is obviously a great contributing factor in slowing the heat evacuation, especially when contact conductance is high due to an important contact pressure.

From there, it follows that an investigation of the minimum depth of cooling channels is in order. This is of importance mostly for the production cycle time, as the quenching is sufficient even with a thicker layer of the dies' material above the channels, provided it has been cooled

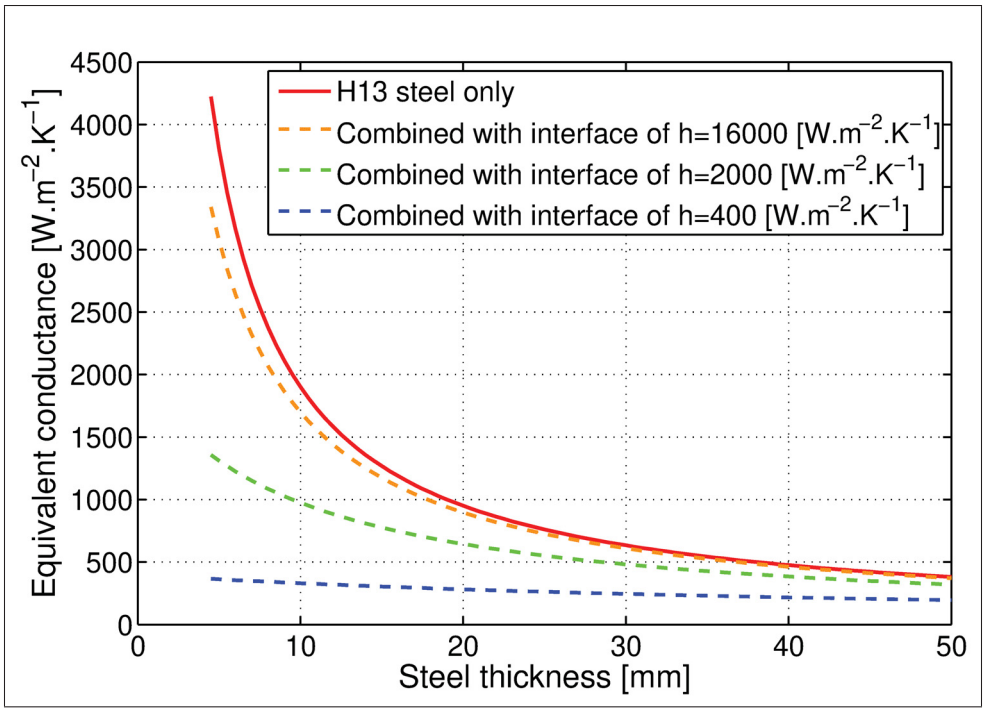

Figure 4.1 Equivalent heat thermal conductance with different die thickness, measured from cooling channels' axis

enough beforehand. Thinning this section will, however, result in a much faster heat evacuation by the coolant due to higher temperature gradients.

Figure 4.2 shows that when the wall is thick enough, there is only a stress concentration at the top and bottom of the channel. At a depth of 6 mm the material between the channel and the die surface acts more like a fixed beam and the location of maximum stress switch to the forming surface directly above the channels. An engineering decision for the depth would probably be made only on the basis of the maximum stress and not on deformation since the maximum deviation of the forming surface above the 6 mm channel is only 0.045 mm, which is much lower than the expected precision of the forming process. This supposes, of course, conditions similar to the assumptions made for this simple model.

Table 4.1 tells us that mechanically speaking, there isn't much to be gained in placing the channels deeper than 10 mm in terms of die mechanical resistance. Indeed, the maximum stress reached around the channel does not decrease significantly when the depth is increased

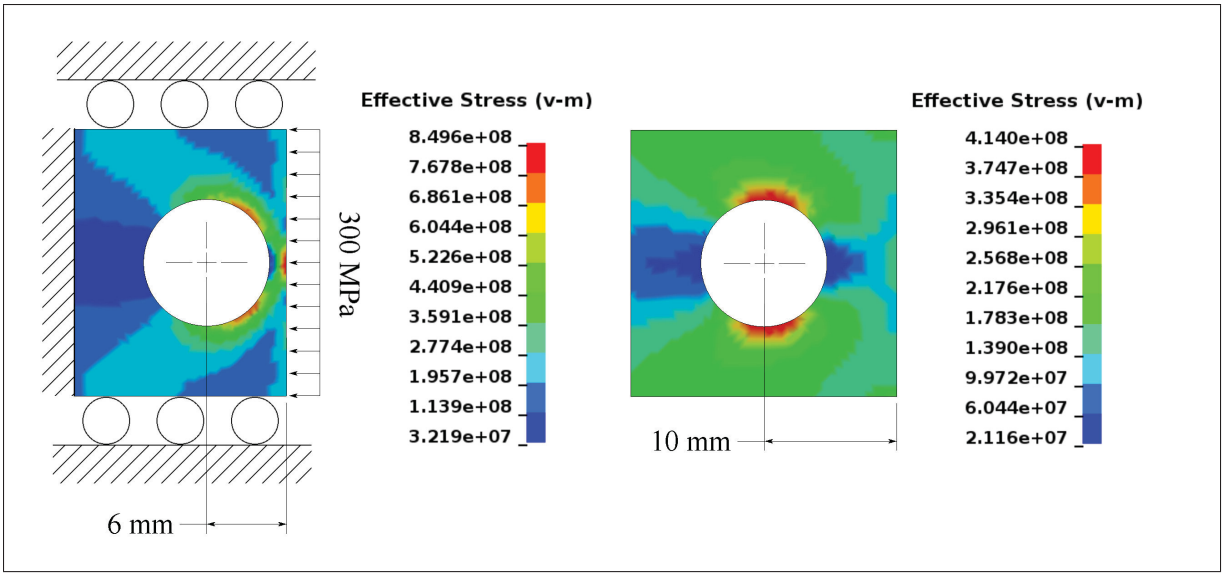

Figure 4.2 Effect of cooling channel depth on stress distribution

above that value. That scenario assumes an infinite medium both in the axis of the channels, a repeated pattern in the transverse direction and a maximum pressure of 300 MPa, which means that it is not necessarily true for all die locations. Also, at this depth, the assumptions of the channels' internal fixed temperature would not necessarily hold true due to the higher temperature gradient. The convection coefficient of the coolant in such a case would have a much higher impact, requiring a more precise evaluation taking into account the type of flow, hydrodynamic entrance regional effects and mass flow.

Table 4.1 Effects of channel depth on maximum stress and its location

Channel depth [mm]	**Maximum Von-Mises stress [MPa]**	**Location of maximum stress**
6	850	Die surface
8	482	Channel
10	414	Channel
12	409	Channel

Another option to improve heat diffusion is to use multiple materials in the construction of the dies. This could be achieved through multiple techniques. For small, deep sections, it is possible to use press fitted inserts of a higher conductivity material such as copper to drain the heat directly to a cooling channel. Also, modern techniques such as cold-spray and additive manufacturing could potentially be used to achieve a sufficiently hard surface on a matrix made of a more conductive material. Such improvements are easier on aluminium hot stamping due to the lower stresses and temperatures than those seen in steel hot stamping.

A last change to the tooling is the displacement and force profile of the hydraulic press. During the stamping of the presented part, quenching happened before the end of the displacement. This was discussed in the analysis of the process simulation but it was also possible to hear a sound similar to cracking indicating part movement due to shrinking in the dies. During later tests when the process was better controlled, those sounds were heard after full die closure, indicating that cooling happened with a better timing. An improved displacement curve would use a fast displacement resulting in a strain rate between 0.1 and 1 s^{-1}, which we know to have the desired hardening effect to help prevent thinning.

4.2 Changes on the Blank

One of the first area to implement improvements would be blank geometry, although it may be hard to accomplish. While there exist many computational optimization tools that can do this step, experienced human judgement can result in a quick reduction of stresses at critical locations. Simple addition or removal of blank material can respectively restrict or ease the flow of material towards the interior of the part and change behaviour. Adding material can also help prevent folds as it becomes too big to form a "S" shape between the dies.

Increased strain rate at high strain locations could help prevent local thinning by a higher yield strength seen at higher strain rates. Such a change, however, will also be influenced by a different cooling profile and formability limits at different strain rates.

Either by a special laminating step or by welding, blanks of variable thickness have been experimented on for steel hot stamping. Further weight reduction could be achieved with this technique although the added complexity might currently make it uneconomical.

A tailored temperature field might be used with the goal of preventing localized thinning in specific cases. Allowing the blank to pass through a curtain of induction heating field or using surface contact on a grip that transfers the blank in the dies would result in uneven temperatures. If appropriately designed, these could prevent thinning at certain cooler locations with a higher yield stress. According to the cooling rates seen in the the sample clamped in the heat transfer rig, this step would not need to last longer than the current transfer time by a robotized arm. Only the clamps would need a redesign to be at the right location with the appropriate internal cooling. Adequate quenching would still be possible due to the cycle time being unaffected, still under 20 s.

4.3 Ideal Production Cycle

A few key changes were made to represent the proposed changes. First, blank geometry was updated to reduce the amount of material in the corner closest to the 3D corner of the part. It was done to help material flow and help feed the area where maximum thinning and cracking was previously observed on the formed part. Other locations could not be improved, as it was observed that folds tend to appear everywhere else blank material is removed.

Before modelling the final solution, an analysis of the effects of subsequent production cycle on initial temperatures is done. Of great interest for industrial application is the number of stampings required to achieve a thermal steady state in the process and the temperature ranges seen on the dies at this moment. A small section of the model was isolated to reduce computation time and was submitted to successive cycles of hot stamping. The leftmost edge of a sample cutaway was locked in its X direction to represent being held by the remainder of the blank during the whole simulation. It was cut at the same location as the die shown in Figure 4.4. This boundary condition was verified by checking nodes in a full simulation, in

which a displacement of less than 2 mm was observed. Since mechanical precision was not of importance, the mechanical implicit solver's tolerances were lowered, once again to speed up simulation. A temperature of $40°C$ was applied to the cooling surface to represent the cooling fluid, initial die temperature was $30°C$ and air temperature for convection was set to $25°C$ with a convection coefficient of 38 $\frac{W}{m^2K}$. Some virtual springs were also added to lift the part when the dies open to let convection act on the dies' surfaces.

A well controlled hydraulic forming press could achieve a consistent speed for almost all its stoke with an accumulator to accelerate quickly and springs to help stop the movement at the end. Although a bit idealized, the movement was set by a simple ramp from $t = 0s$ to $t = 1.65s$. The blank is held for a full 10 s and the die retracts from $t = 11.65s$ to $t = 14.65s$ at its original position, where it stay until $t = 20s$ and the simulation ends. For the cycles, temperatures at all nodes at the end of each cycle were used as initial temperatures for the start of the following cycle. All other conditions such as initial blank temperature, $480°C$, were the same as for the ideal process' simulation.

The above temperature peaks show high variations but this is mostly due to data output during simulation. Fast variations in temperature were only recorded if the timesteps at which they happened were timed with the recorded increments. However, the total heat balance was the same, which is the most important metric in this case. Iterations were stopped when maximum surface temperature was within $5°C$ from initial state. Dies with ideal cooling, i.e. a fixed temperature surface at a depth of 15 mm, showed a stabilization after 5 cycles. For the dies used in the experiment, stabilization was observed only after 9 cycles. Furthermore, maximum initial die surface temperatures showed a difference of $65°C$, enough to influence cooling behaviour. As expected, temperature at 10 mm depth is much lower on ideally cooled dies due to the cooling channels being closer. Figure 4.4 show surface temperature at the end of curves in Figure 4.3.

Maximum temperature is different but so is the distribution. Heat accumulation at the 3D corner is due to having a greater ratio of heated surface to cooled surface than at other location

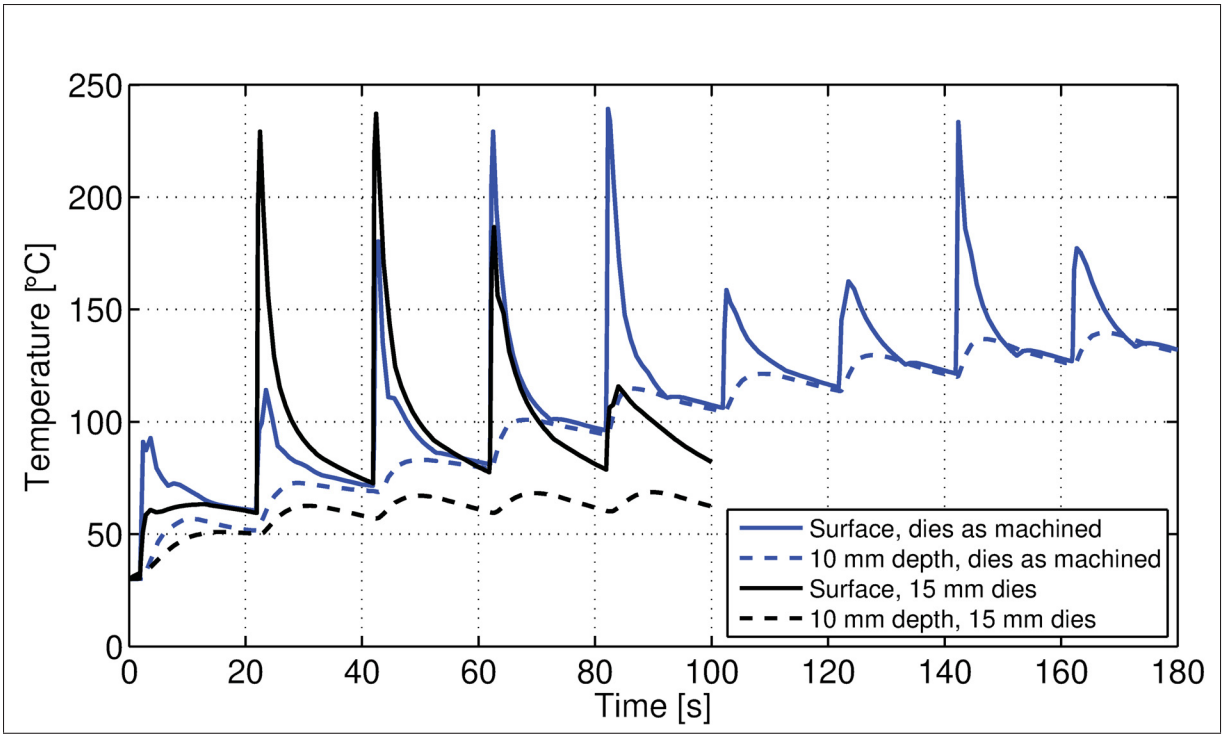

Figure 4.3 Variations of nodal temperature at location B from Figure 3.26

.

in the dies. This effect is minimized in the simulation with and ideal cooling surface and this improvement could be recreated by using cooling baffles that redirect water flow to small locations.

The suggested improved process begins with an initial blank temperature of, again, 480°C to represent a quick transfer from the oven at 490°C. Also, while the blank was previously gravity loaded to recreate the conditions of the experiment, it is now held in the air to represent spring loaded pins or other similar holding apparatus. Dies initial temperature was set to 100°C to represent dies with cooling channels performing halfway between the previously machined dies and the ideally cooled dies used for the cycles study. Dies' closing speed was set to the maximum speed observed in the experimental trials. The same displacement profile as described earlier for the upper die was used. Figure 4.5 below shows the temperature profiles at the same locations as in Figure 3.20.

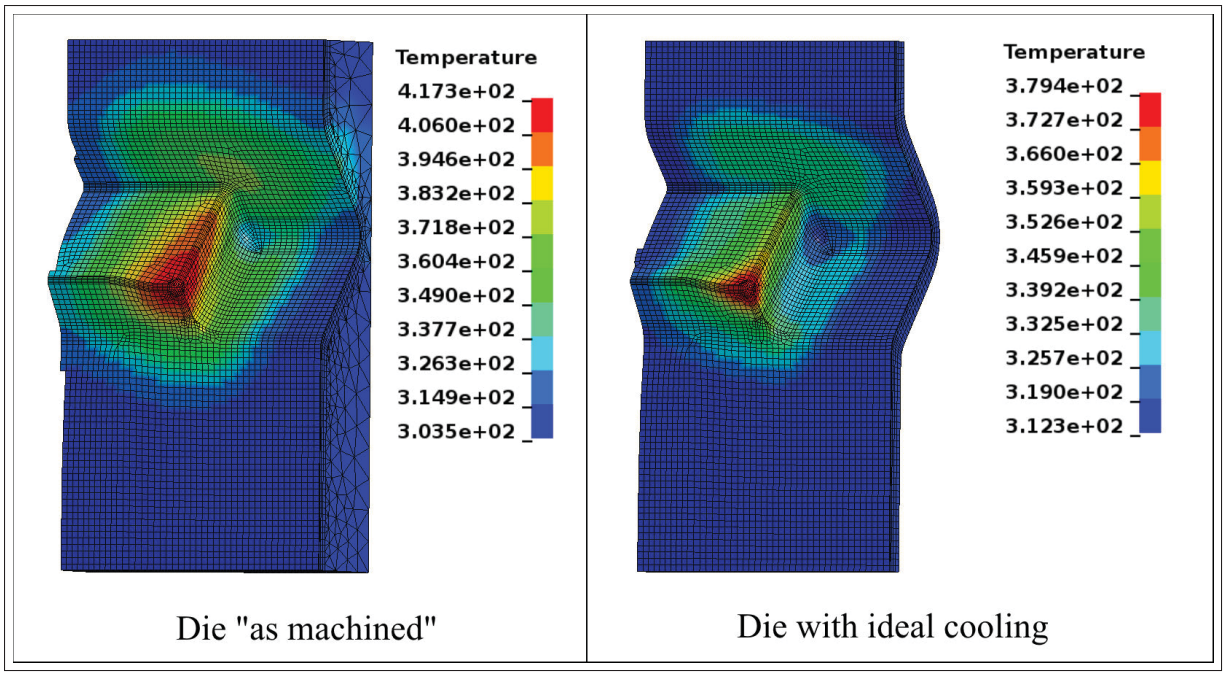

Figure 4.4 Surface temperature of dies at end of last cycle shown by Figure 4.3

.

These results show the importance of a quick transfer to the dies and an improved cooling scheme. Still, this provisory simulation showed that adequate quenching can be achieved in a 20 s production cycle. Blank temperature dipped below the initial dies temperature because the cooling channels had enough time to lower overall die temperature during the simulation.

Stresses reached during forming were similar to those seen in the simulation of the experiment. Howerver, material flow towards the 3D corner was improved, as seen in the "ideal process" curve in Figure 3.19. Material at the extremities of the measured profile near the 3D corner see less thinning than when experiment is simulated. This is also aided by a generally higher strain rate at this location, promoting hardening at locations where there is more strain.

Enough material was left all around the part. Figure 4.6 shows the evolution of the blank throughout all the forming step. It would be possible to remove more blank material, reducing losses and aiding in cooling by reducing the total heat that has to be evacuated by the cooling fluid. However, some locations require added material to prevent folds. A binder system could be added to reduce wrinkles, helping solve this issue and remove more blank material. A design

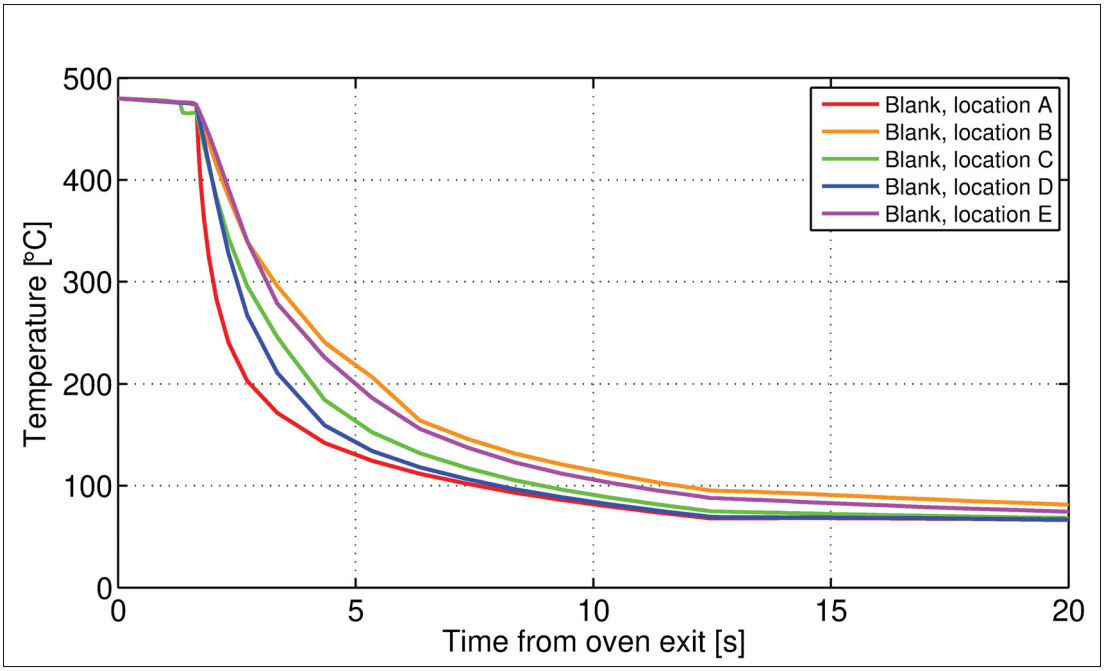

Figure 4.5 Temperature of blank nodes at locations shown in Figure 3.20 for improved process

.

revision of the part would be the most straightforward way to ensure consistent, high-quality production.

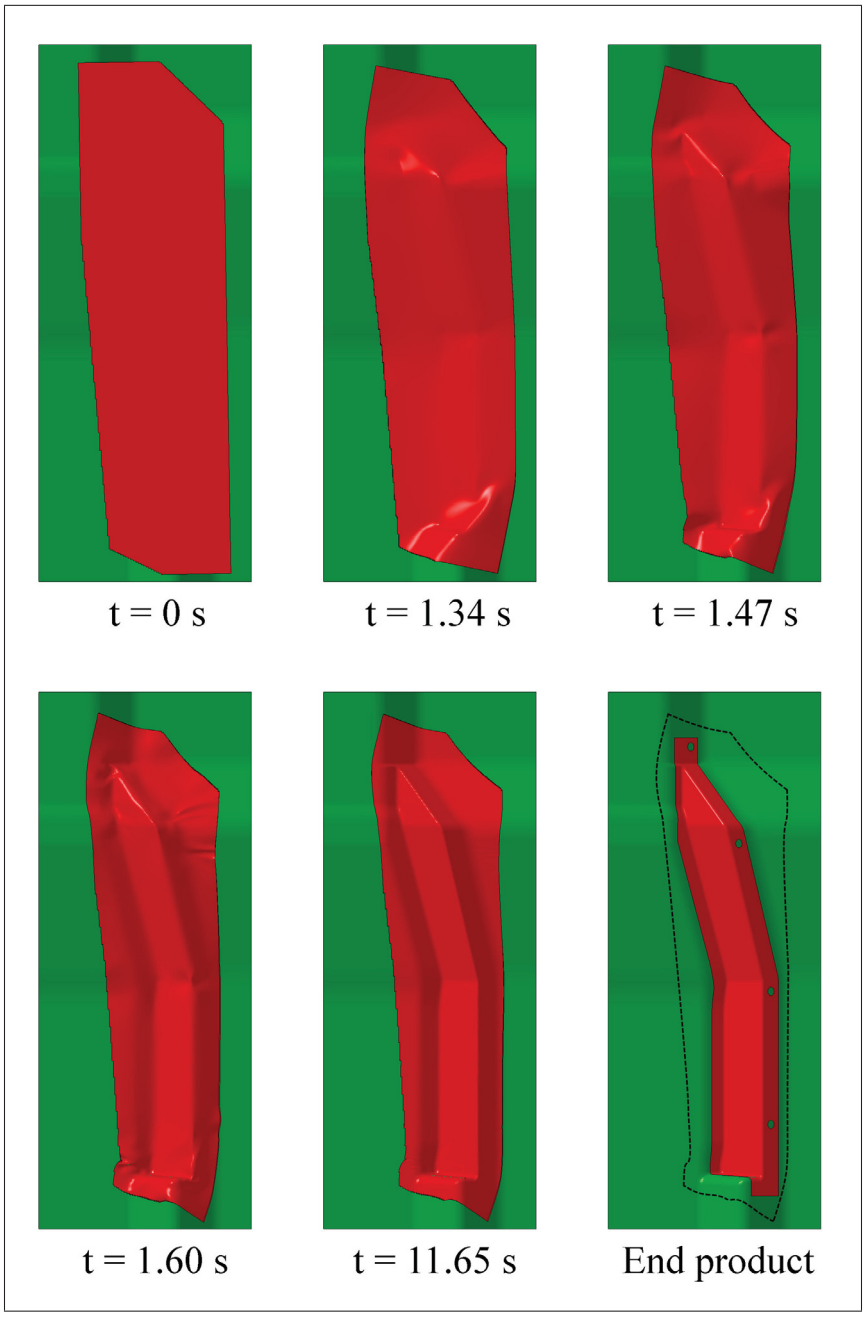

Figure 4.6 Evolution of blank shape throughout ideal forming process

.

CONCLUSION AND RECOMMENDATIONS

This work was done to provide the necessary material parameters and solver deck inputs to accurately simulate the hot stamping process with die quenching. In turn, this simulation showed that this process could be used successfully to make parts suitable for automotive structural applications, although some improvement must be made to the current experimental tooling. The strength to density ratio of AA7075 means that lightweighting is possible for cars by replacing boron steel structural components.

The Barlat 89 material model with 3 parameters provided reasonable accuracy when properties were characterized from uniaxial traction specimens at different orientations from the laminating angle. The aforementioned specimens are cut from different orientations from the sheet's laminating angle and tested at different combinations of strain rates and temperature. Strain anisotropy was measured from samples after being sumbitted to a 20% strain.

A simple test apparatus was used to measure the conductance between the surfaces of a hot aluminium sheet and steel dies. Conductance as a function of pressure was obtained from inverse modelling of these tests. Although the results from the tests showed an important variability, the resulting fitted data curve was similar to the values found in the literature, which tends to show a certain disparity between studies.

A prototype part and its forming dies were used as a basis for a validation of the data obtained. General accuracy was good, although a 3D corner with a crack showed that only crack initiation could be predicted, but not its propagation. Some simulation parameters were changed to evaluate their effects. It was found that a 2 mm shell mesh for the blank provided a good compromise between accuracy and computation speed. Dies were meshed up to their cooling channels, and quench phenomenon was found to be more dependent on surface heat absorptivity while production cycle depended more on the cooling channels' depth.

An improved production cycle spanning 20 s was suggested and simulated. Some improvements were seen in metrics such as thinning and cooling rates. Steady-state surface temperature for this cycle was between 50°C and 150°C for different locations on different types of dies. Even if this part could be produced with some additional process improvements, a design revision is suggested to adapt the part geometry to aluminium hot stamping.

Major improvements in the accuracy could be obtained by using Nakazima and cross-die tests to build a damage model based on more realistic biaxial stresses and loading paths. Limitations of the material model were identified and discussed in the mechanical characterization section. A yield function that uses both the anisotropy in stresses and strains would be preferable to the Barlat 89 model used. A less discussed theme in this project was tribological behaviour. A more precise evaluation of friction and surface finishes on simulation precision is in order.

In terms of characterization experiments, precision could be improved by a better control of the temperature cycle of the samples. An induction heating system could help reproduce the hot stamping conditions on the samples better than reheating after a quench. Also, there is a potential variation of anisotropy as a function of total strain that may have an insignificant effect. Many improvements were suggested to achieve a better interfacial heat conductance characterization, although the wide variations seen in the literature indicates that it might still present a challenge. Also, a more complete campaign of electrical conductivity tests including the effects of age hardening is vital to properly assess thermal precision of the simulations.

Precision of the resulting FEA model is deemed sufficient to allow manufacturers to replace some of the initial tool design iterations for the hot stamping and quenching process. It is able to predict, for example, some of the issues that may be encountered such as folds and veiling patterns in the blank that appear during the process or give an rough idea of the achievable cooling rate.

Although still in its infancy, the use of age hardenable aluminium in automotive structural parts is seen as a viable alternative to commonly used boron steel and able to help in weight reduction.

APPENDIX I

MAIN SIMULATION SOLVER DECK

```
KEYWORD
$
TITLE
PERD, Hot Stamping, year 1
$
$ Date:                December 15, 2017
$ Units:                Primary:  m, kg, s / secondary:  Pa
$ Author:                Benoit Theriault
$
$ All data tables and curves with more than 10 line are omitted for clarity
$
$---+----1----+----2----+----3----+----4----+----5----+----6----+----7----+----8
$
$ General control Cards
$
$---+----1----+----2----+----3----+----4----+----5----+----6----+----7----+----8
$
PARAMETER
R     endt     20.00
$ &endt appears in multiple loading curves
$
CONTROL_TERMINATION
$   ENDTIM    ENDCYC     DTMIN    ENDNEG    ENDMAS
     &endt         0
$
CONTROL_TIMESTEP
$   dtinit    tssfac      isdo    tslimt     dt2ms      lctm     erode     msist
      0.10       1.0
$
CONTROL_SHELL
$   WRPANG    ITRIST     IRNXX    ISTUPD    THEORY       BWC     MITER
    20.000         0        -1         1         2         1         2
$                                         TSHELL
                                              1
$
CONTROL_CONTACT
$   SLSFAC    RWPNAL    ISLCHK    SHLTHK    PENOPT    THKCHG     ORIEN
     0.100     1.000         2         2         1         0         1
$   USRSTR    USRFAC     NSBCS    INTERM    XPENEN
         0         0        10         0   1.0E+01
$

$

$                                                                 THOFF
```

```
                                                                      1
$
CONTROL_ENERGY
$     HGEN      RWEN    SLNTEN     RYLEN
         2         2         1         1
$
CONTROL_HOURGLASS
$      IHQ        QH
         5      0.10
$
$---+----1----+----2----+----3----+----4----+----5----+----6----+----7----+----8
$
$ Thermal Solver
$
$---+----1----+----2----+----3----+----4----+----5----+----6----+----7----+----8
$
CONTROL_SOLUTION
$     SOLN
         2
$
CONTROL_THERMAL_SOLVER
$---+----1----+----2----+----3----+----4----+----5----+----6----+----7----+----8
$    ATYPE     PTYPE    SOLVER     CGTOL       GTP    EQHEAT     FWORK       SBC
         1         1         3    1.0e-3         0       1.0       0.8 -5.67e-08
$
CONTROL_THERMAL_TIMESTEP
$---+----1----+----2----+----3----+----4----+----5----+----6----+----7----+----8
$       TS       TIP       ITS      TMIN      TMAX     DTEMP      TSCP      LCTS
         1         1      1.00   1.0e-10       1.0        20       0.5
$
$---+----1----+----2----+----3----+----4----+----5----+----6----+----7----+----8
$
$ Mechanical Solver
$
$---+----1----+----2----+----3----+----4----+----5----+----6----+----7----+----8
$
CONTROL_IMPLICIT_GENERAL
$   imflag       dt0      iefs
         1    1.0e-3         2
$
CONTROL_IMPLICIT_SOLUTION
$  nlsolvr    ilimit    maxref     dctol     ectol     rctol     lstol    abstol
         2         2        25   3.0E-04   3.0E-04   1.0E-03      1.00   1.0E-08
$    dnorm   divflag   inistif   nlprint    nlnorm
         2         1         1         1         2
$
CONTROL_IMPLICIT_SOLVER
$   LSOLVR    LPRINT     NEGEV     ORDER      DRCM    DRCPRM   AUTOSPC   AUTOTOL
         6         0         1         0         1
$   LCPACK
         2
$
```

```
CONTROL_IMPLICIT_AUTO
$    iauto    iteopt    itewin     dtmin     dtmax     dtexp
         1        15         0   1.0E-08       1.0
$
CONTROL_IMPLICIT_DYNAMICS
$    IMASS     GAMMA      BETA    TDYBIR    TDYDTH    TDYBUR     IRATE
         1       0.6       0.3       0.0      20.0                 0
$
$
$---+----1----+----2----+----3----+----4----+----5----+----6----+----7----+----8
$
$ Database options
$
$---+----1----+----2----+----3----+----4----+----5----+----6----+----7----+----8
$
DATABASE_GLSTAT
$       DT
   5.0e-02
$
DATABASE_RCFORC
$       DT
   5.0e-02
$
DATABASE_BINARY_D3PLOT
$  DT/CYCL      LCDT    NOBEAM
   5.0e-02
$
DATABASE_EXTENT_BINARY
$    NEIPH     NEIPS    MAXINT    STRFLG    SIGFLG    EPSFLG    RLTFLG    ENGFLG
        20        20         9       111         1         1         1         1
$   CMPFLG    IEVERP    BEAMIP     DCOMP      SHGE     STSSZ
         1         1         0         2         0         0
$
DATABASE_BINARY_INTFOR
$  DT/CYCL      LCDT    NOBEAM
   5.0e-02
$
DATABASE_EXTENT_INTFOR
$    nglbv     nvelo    npresu    nshear     nforc     ngapc     nfail    ieverf
         1         0         1        -1        -1         0         0         1

$
$
$---+----1----+----2----+----3----+----4----+----5----+----6----+----7----+----8
$
$ Mesh
$
$---+----1----+----2----+----3----+----4----+----5----+----6----+----7----+----8
$
DEFINE_TRANSFORM
$   TRANID
         1
```

```
$   OPTION        XO        YO        ZO
     SCALE      1e-3      1e-3      1e-3
$
INCLUDE_TRANSFORM
$ FILENAME
Part_Tesla_1_2_3mm_shells_p1_E1_N1_renum.k
$   IDNOFF    IDEOFF    IDPOFF    IDMOFF    IDSOFF    IDFOFF    IDDOFF

$   IDROFF

$   FCTMAS                                INCOUT1

$   TRANID
         1
$
$---+----1----+----2----+----3----+----4----+----5----+----6----+----7----+----8
$
DEFINE_TRANSFORM
$   TRANID
         2
$   OPTION        XO        YO        ZO
     SCALE      1e-3      1e-3      1e-3
$   OPTION        XO        YO        ZO
    ROTATE     0.000     0.000     1.000                                   -90.0
$
INCLUDE_TRANSFORM
$ FILENAME
matrice_lower_10mmThickBiased_p2_sid1_nid201.k
$matrice_lower_10mmThickBiased_p2_sid1_V01.k
$   IDNOFF    IDEOFF    IDPOFF    IDMOFF    IDSOFF    IDFOFF    IDDOFF

$   IDROFF

$   FCTMAS                                INCOUT1

$   TRANID
         2
$
$---+----1----+----2----+----3----+----4----+----5----+----6----+----7----+----8
$
DEFINE_TRANSFORM
$   TRANID
         6
$   OPTION        XO        YO        ZO
     SCALE      1e-3      1e-3      1e-3
$   OPTION        XO        YO        ZO
    ROTATE     0.000     0.000     1.000                                   -90.0
$   Die opening
$   OPTION        XO        YO        ZO
    TRANSL    0.0000    0.0000   0.19818
$
$
```

```
INCLUDE_TRANSFORM
$ FILENAME
matrice_upper_10mmThickBiased_p6_sid5_nid601.k
$
$   IDNOFF    IDEOFF    IDPOFF    IDMOFF    IDSOFF    IDFOFF    IDDOFF

$   IDROFF

$   FCTMAS                                  INCOUT1

$   TRANID
         6
$
$---+----1----+----2----+----3----+----4----+----5----+----6----+----7----+----8
$
$ Thermal dilatation
PARAMETER
R  THSCALE    1.0123
$
DEFINE_TRANSFORM
$   TRANID
        11
$   OPTION        XO        YO        ZO
     SCALE      1e-3      1e-3      1e-3
$   OPTION        XO        YO        ZO
     SCALE  &THSCALE  &THSCALE  &THSCALE
$   OPTION        XO        YO        ZO
    ROTATE     0.000     0.000     1.000                                    0.95
$   OPTION        XO        YO        ZO
    TRANSL   -0.0130   -0.0290   0.00060
$
INCLUDE_TRANSFORM
$ FILENAME
mesh_blank_810x232_angle100mm_p11_sid11-12_2mm.k
$   IDNOFF    IDEOFF    IDPOFF    IDMOFF    IDSOFF    IDFOFF    IDDOFF

$   IDROFF

$   FCTMAS                                  INCOUT1

$   TRANID
        11
$
INCLUDE
segments_blank_810x232_angle100mm_p11_sid11-12_2mm.k
$
$
$---+----1----+----2----+----3----+----4----+----5----+----6----+----7----+----8
$
$ Material
$
$---+----1----+----2----+----3----+----4----+----5----+----6----+----7----+----8
```

```
$
$
MAT_036
$      MID        RO         E        PR        HR        P1        P2      ITER
         2      2810  21.0E+09      0.33         9       0.0       0.0       0.0
$        M       R00       R45       R90      LCID        E0       SP1        P3
       8.0    -76300    -76345    -76390    999000       0.0       0.0       0.0
$     AOPT
       0.0
$                                    A1        A2        A3
                                    0.0       0.0       0.0
$       V1        V2        V3        D1        D2        D3      BETA
       0.0       0.0      -1.0       0.0       0.0       0.0       0.0
$
$
$ Thermal expansion coefficients from MPDB
MAT_ADD_THERMAL_EXPANSION
$---+----1----+----2----+----3----+----4----+----5----+----6----+----7----+----8
$      PID      LCID      MULT     LCIDY     MULTY     LCIDZ     MULTZ
        11       171       1.0       171       1.0       171       1.0
$
$ Rigid for upper die (free z axis)
MAT_RIGID
$      MID        RO         E        PR         N    COUPLE         M     ALIAS
         4  7.89E+03  210.0E+9      0.29
$      CMO      CON1      CON2
         1         4         7
$      LCO        A2        A3        V1        V2        V3

$
$ Rigid for lower die (fixed)
MAT_RIGID
$      MID        RO         E        PR         N    COUPLE         M     ALIAS
         7  7.89E+03  210.0E+9      0.29
$      CMO      CON1      CON2
         1         7         7
$      LCO        A2        A3        V1        V2        V3

$
$ AA7075
MAT_THERMAL_ISOTROPIC_TD
$     TMID       TRO     TGRLC    TGMULT
         2  2.810+03         0         0
$       T1        T2        T3        T4        T5        T6        T7        T8
 -1000.000   273.000   373.000   473.000   573.000   673.000   773.000  1873.000
$       C1        C2        C3        C4        C5        C6        C7        C8
 8.2392e+2 8.2392e+2 8.9980e+2 9.6371e+2 1.0414e+3 1.1418e+3 1.1721e+3 1.1721e+3
$       K1        K2        K3        K4        K5        K6        K7        K8
 1.1985e+2 1.1985e+2 1.3894e+2 1.6937e+2 1.7634e+2 1.7092e+2 1.6753e+2 1.6753e+2
$
$ H13
MAT_THERMAL_ISOTROPIC_TD
```

```
$     TMID       TRO     TGRLC    TGMULT
         1  7.800+03         0         0
$       T1        T2        T3        T4        T5        T6        T7        T8
 -1000.000   273.000   373.000   473.000   573.000   673.000   773.000  1873.000
$       C1        C2        C3        C4        C5        C6        C7        C8
 4.6000e+2 4.6000e+2 4.6328e+2 4.7397e+2 4.9198e+2 5.1733e+2 5.5000e+2 5.9000e+2
$       K1        K2        K3        K4        K5        K6        K7        K8
 1.7289e+1 1.7289e+1 2.0721e+1 2.3328e+1 2.4561e+1 2.5027e+1 2.5332e+1 2.6084e+1
$
$
$---+----1----+----2----+----3----+----4----+----5----+----6----+----7----+----8
$
$ Parts
$
$---+----1----+----2----+----3----+----4----+----5----+----6----+----7----+----8
$
PART
 Final Part shells
$      PID     SECID       MID     EOSID      HGID      GRAV    ADPOPT      TMID
         1         2         7         0
$
PART
 Lower die solids
$      PID     SECID       MID     EOSID      HGID      GRAV    ADPOPT      TMID
         2         1         7         0                                       1
$
PART
 Upper die solids
$      PID     SECID       MID     EOSID      HGID      GRAV    ADPOPT      TMID
         6         1         4         0                                       1
$
PART
 Blank shells
$      PID     SECID       MID     EOSID      HGID      GRAV    ADPOPT      TMID
        11         2         2         0                                       2
$
$
$---+----1----+----2----+----3----+----4----+----5----+----6----+----7----+----8
$
$ Section
$
$---+----1----+----2----+----3----+----4----+----5----+----6----+----7----+----8
$
SECTION_SOLID
$      SID    ELFORM
         1         1
$
SECTION_SHELL_THERMAL
$      SID    ELFORM      SHRF       NIP     PROPT   QR/IRID     ICOMP
         2        16     0.833       7.0       0.0       0.0         0
$       T1        T2        T3        T4      NLOC
  2.055E-3  2.055E-3  2.055E-3  2.055E-3         0
```

```
$       TH
         2
$
$
$---+----1----+----2----+----3----+----4----+----5----+----6----+----7----+----8
$
$ Contact
$
$---+----1----+----2----+----3----+----4----+----5----+----6----+----7----+----8
$
PARAMETER
  R    H0M       400
  R   LMIN  0.188E-4
  R   LMAX    0.0100
$
$ Sheet to Lower
CONTACT_SURFACE_TO_SURFACE_THERMAL_FRICTION
$     SSID      MSID     SSTYP     MSTYP    SBOXID    MBOXID       SPR       MPR
        12       251         0         0         0         0         1         1
$       FS        FD        DC        VC       VDC    PENCHK        BT        DT
     0.110     0.110       1.0       0.0        10         1       0.0     100.0

$      SFS       SFM       SST       MST      SFST      SFMT       FSF       VSF
       1.0       1.0       0.0       0.0       1.0       1.0       1.0       1.0
$        K      FRAD        H0      LMIN      LMAX      CHLM    BC_FLG      ALGO
     0.075  4.19E-08      &H0M     &LMIN     &LMAX       1.0         1         0
$    LCFST     LCFDT    FORMUA         A
                             1         3
$     SOFT    SOFSCL    LCIDAB    MAXPAR     SBOPT     DEPTH     BSORT    FRCFRQ

$   PENMAX    THKOPT    SHLTHK     SHLOG      ISYM     I2D3D    SLDTHK    SLDSTF

$     IGAP    IGNODPRFAC/MPADTSTIF/MPAR2   UNUSED     UNUSED    FLANGL   CID_-
RCF
         2
$
$ Sheet to Upper
CONTACT_SURFACE_TO_SURFACE_THERMAL_FRICTION
$     SSID      MSID     SSTYP     MSTYP    SBOXID    MBOXID       SPR       MPR
        11       651         0         0         0         0         1         1
$       FS        FD        DC        VC       VDC    PENCHK        BT        DT
     0.110     0.110       1.0       0.0        10         1       0.0     100.0

$      SFS       SFM       SST       MST      SFST      SFMT       FSF       VSF
       1.0       1.0       0.0       0.0       1.0       1.0       1.0       1.0
$        K      FRAD        H0      LMIN      LMAX      CHLM    BC_FLG      ALGO
     0.075  4.19E-08      &H0M     &LMIN     &LMAX       1.0         1         0
$    LCFST     LCFDT    FORMUA         A
                             1         3
$     SOFT    SOFSCL    LCIDAB    MAXPAR     SBOPT     DEPTH     BSORT    FRCFRQ

$   PENMAX    THKOPT    SHLTHK     SHLOG      ISYM     I2D3D    SLDTHK    SLDSTF
```

```
$     IGAP    IGNODPRFAC/MPADTSTIF/MPAR2   UNUSED     UNUSED    FLANGL   CID_-
RCF
         2
$
DEFINE_CURVE
$     LCID      SIDR      SCLA      SCLO      OFFA      OFFO
         3                 1.0       1.0       0.0       0.0
$           PRESSURE         CONDUCTANCE
               0.0E6               400.0
               0.1E6              2400.0
               1.0E6             16000.0
              1.0E12             16000.0
$
$
$---+----1----+----2----+----3----+----4----+----5----+----6----+----7----+----8
$
$ Displacements
$
$---+----1----+----2----+----3----+----4----+----5----+----6----+----7----+----8
$
INCLUDE
Disp_Upper_Die.k
$ Displacement load curve 6001
$
BOUNDARY_PRESCRIBED_MOTION_NODE
$     NSID       DOF       VAD      LCID        SF       VID     DEATH     BIRTH
   6000000         3         2      6001     -1.00
$
LOAD_GRAVITY_PART
$      PID       DOF        LC     ACCEL      LCDR      STGA      STGR
        11         3        21      9.81
$
DEFINE_CURVE
$     LCID      SIDR      SCLA      SCLO      OFFA      OFFO
        21                 1.0       1.0       0.0       0.0
$               TIME             GRAVITY
                0.00                1.00
                6.00                1.00
               &endt                0.00
$
DAMPING_GLOBAL
$     LCID    VALDMP       STX       STY       STZ       SRX       SRY       SRZ
        22
$
DEFINE_CURVE
$     LCID      SIDR      SCLA      SCLO      OFFA      OFFO
        22                 1.0       1.0       0.0       0.0
                0.00               30.00
                6.00               30.00
                7.00                0.00
               &endt                0.00
```

```
$
$---+----1----+----2----+----3----+----4----+----5----+----6----+----7----+----8
$
$ Initial temperature
$
$---+----1----+----2----+----3----+----4----+----5----+----6----+----7----+----8
$
BOUNDARY_TEMPERATURE_SET
$  NID/SID     TLCID     TMULT       LOC
       201         0       291
$
BOUNDARY_TEMPERATURE_SET
$  NID/SID     TLCID     TMULT       LOC
       601         0       291
$
PARAMETER_EXPRESSION
$---+----1----+----2
R     TEMP   460+273
$
$ Dies
SET_NODE_GENERAL
$#     sid       da1
         7
$# option         e1        e2        e3
PART              1         2         6
$
INITIAL_TEMPERATURE_SET
         7     291.0
$
$ Blank
SET_NODE_GENERAL
$#     sid       da1
        12
$# option         e1
PART             11
$
INITIAL_TEMPERATURE_SET
        12     &TEMP
$
$
$---+----1----+----2----+----3----+----4----+----5----+----6----+----7----+----8
$
$ Thermal Convection
$
$---+----1----+----2----+----3----+----4----+----5----+----6----+----7----+----8
$
$ Air temperature
DEFINE_CURVE
$     LCID      SIDR      SCLA      SCLO      OFFA      OFFO
         7         0      1.00      1.00      0.00      0.00
$                ABS                ORD
                 0.0             291.0
```

```
               30.0               291.0
$
$ Convection coefficient
DEFINE_CURVE
$     LCID      SIDR      SCLA      SCLO      OFFA      OFFO
         8         0      1.00      1.00      0.00      0.00
$                ABS                ORD
                 0.0               25.0
                30.0               25.0
$
$ Dies
$BOUNDARY_CONVECTION_SET
$     SSID
$       251
$    HLCID     HMULT     TLCID     TMULT       LOC
$         8       1.0         7       1.0
$
$ Dies
$BOUNDARY_CONVECTION_SET
$     SSID
$       651
$    HLCID     HMULT     TLCID     TMULT       LOC
$         8       1.0         7       1.0
$
$ Blank
BOUNDARY_CONVECTION_SET
$     SSID
        11
$    HLCID     HMULT     TLCID     TMULT       LOC
         8       1.0         7       1.0         1
$
$ Blank
BOUNDARY_CONVECTION_SET
$     SSID
        12
$    HLCID     HMULT     TLCID     TMULT       LOC
         8       1.0         7       1.0         1
$
$
$---+----1----+----2----+----3----+----4----+----5----+----6----+----7----+----8
$
$ Dynain
$
$---+----1----+----2----+----3----+----4----+----5----+----6----+----7----+----8
$
SET_PART_LIST
$      SID
      2001
$     PID1
        11
$
INTERFACE_SPRINGBACK_LSDYNA
```

```
$     PSID
      2001
$
END
```

BIBLIOGRAPHY

Abedrabbo, N., Pourboghrat, F. & Carsley, J. (2006). Forming of aluminum alloys at elevated temperatures–part 1: Material characterization. *International journal of plasticity*, 22(2), 314–341.

Aspacher, J. (2008). Forming hardening concepts. *First international conference on hot sheet metal forming of high performance steel*, pp. 77–81.

ASTM. (2001). *Standard Practice for Heat Treatment of Wrought Aluminum Alloys*. ASTM B918-01. West Conshohocken, PA, United States of America: ASTM. Consulted at https://doi.org/10.1520/B0918-01.

Banabic, D., Vulcan, M. & Siegert, K. (2005). Bulge testing under constant and variable strain rates of superplastic aluminium alloys. *Cirp annals-manufacturing technology*, 54(1), 205–208.

Banabic, D. (2000). *Formability of metallic materials: plastic anisotropy, formability testing, forming limits*. Springer Science & Business Media.

Bardelcik, A., Salisbury, C. P., Winkler, S., Wells, M. A. & Worswick, M. J. (2010). Effect of cooling rate on the high strain rate properties of boron steel. *International journal of impact engineering*, 37(6), 694–702.

Bariani, P. F., Bruschi, S., Ghiotti, A. & Michieletto, F. (2013). Hot stamping of AA5083 aluminium alloy sheets. *CIRP annals-manufacturing technology*, 62(1), 251–254.

Barlat, F. & Lian, K. (1989). Plastic behavior and stretchability of sheet metals. part I: A yield function for orthotropic sheets under plane stress conditions. *International journal of plasticity*, 5(1), 51 - 66. doi: https://doi.org/10.1016/0749-6419(89)90019-3.

Barlat, F., Brem, J., Yoon, J., Chung, K., Dick, R., Lege, D., Pourboghrat, F., Choi, S.-H. & Chu, E. (2003). Plane stress yield function for aluminum alloy sheets—part I: theory. *International journal of plasticity*, 19(9), 1297–1319.

Barlat, F., Lege, D. J. & Brem, J. C. (1991). A six-component yield function for anisotropic materials. *International journal of plasticity*, 7(7), 693–712.

Bergman, T. L., Incropera, F. P., DeWitt, D. P. & Lavine, A. S. (2011). *Fundamentals of heat and mass transfer*. John Wiley & Sons.

Callister, W. D., Rethwisch, D. G. et al. (2007). *Materials science and engineering: an introduction*. Wiley New York.

Caraher, S., Polmear, I. & Ringer, S. (1998). Effects of Cu and Ag on precipitation in Al–4Zn–3Mg (wt.%). *Proc. 6th intl. conf. aluminium alloys (ICAA6)*, pp. 5–10.

Chang, H., Schoenig, F. & Soules, J. A. (1996). Non-destructive residual stress measurement using eddy current. *Conf proc: ICSP-6*, pp. 356–384.

Chu, E. (1995). Generalization of hill's 1979 anisotropic yield criteria. *Journal of materials processing technology*, 50(1-4), 207–215.

D'Amours, G., Rahem, A., Williams, B., Worswick, M. & Mayer, R. (2007). Crashworthiness of aluminium tubes; part 1: Hydroforming at different corner-fill radii and end feeding levels. *Aip conference proceedings*, 908(1), 787–792.

Deb, K., Pratap, A., Agarwal, S. & Meyarivan, T. (2002). A fast and elitist multiobjective genetic algorithm: NSGA-II. *IEEE transactions on evolutionary computation*, 6(2), 182–197.

Deformacije, D. (2016, October, 15). Nakajima test [Webpage]. Consulted at http://www.3d-deformacije.com/nakajima-flc-Fld-test.

Dumanowski, B. (1997). *Simulation de traitements thermomecaniques de l'alliage de titane ti-6al-4v dans le domaine biphase alpha-beta*. (Ph. D. thesis, INP GRENOBLE).

Elfakir, O. (2015). Studies on the solution heat treatment, forming and in-die quenching process in the production of lightweight alloy components.

Futaba Industrial. (2016, December, 15). Technology information [webpage]. Consulted at http://www.futabasangyo.com/en/products/technical/output/.

Garcia, D., Orteu, J. & Penazzi, L. (2002). A combined temporal tracking and stereo-correlation technique for accurate measurement of 3d displacements: application to sheet metal forming. *Journal of materials processing technology*, 125, 736–742.

Gourdet, S. & Montheillet, F. (2000). An experimental study of the recrystallization mechanism during hot deformation of aluminium. *Materials science and engineering: A*, 283(1), 274–288.

Hill, R. (1979). Theoretical plasticity of textured aggregates. *Mathematical proceedings of the cambridge philosophical society*, 85(1), 179–191.

Hill, R. (1990). Constitutive modelling of orthotropic plasticity in sheet metals. *Journal of the mechanics and physics of solids*, 38(3), 405 - 417. doi: https://doi.org/10.1016/0022-5096(90)90006-P.

Hill, R. (1993). A user-friendly theory of orthotropic plasticity in sheet metals. *International journal of mechanical sciences*, 35(1), 19–25.

Hosford, W. (1972). A generalized isotropic yield criterion. *Journal of applied mechanics*, 39(2), 607–609.

Hosford, W. F. & Caddell, R. M. (2011). *Metal forming: mechanics and metallurgy*. Cambridge University Press.

Lewis, D. & Perkins, H. (1968). Heat transfer at the interface of stainless steel and aluminum—the influence of surface conditions on the directional effect. *International journal of heat and mass transfer*, 11(9), 1371–1383.

Lim, S. T., Eun, I. S. & Nam, S. W. (2003). Control of equilibrium phases (m, t, s) in the modified aluminum alloy 7175 for thick forging applications. *Materials transactions*, 44(1), 181–187.

Livermore Software Technology Corporation (LSTC). (2016). *LS-DYNA keyword user's manual, volume I* [r6319]. Consulted at http://www.lstc.com/download/manuals.

Lucks, C. & Deem, H. (1958). Thermal properties of thirteen metals. In *Thermal Properties of Thirteen Metals*. ASTM International.

MatWeb. (2016, October, 15). Material property data [Website]. Consulted at www.matweb.com.

Menezes, P. L., Kailas, S. V. et al. (2009). Influence of surface texture and roughness parameters on friction and transfer layer formation during sliding of aluminium pin on steel plate. *Wear*, 267(9), 1534–1549.

Mises, R. v. (1928). Mechanik der plastischen formänderung von kristallen. *Zamm-journal of applied mathematics and mechanics/zeitschrift für angewandte mathematik und mechanik*, 8(3), 161–185.

Miyamoto K, N. S. (2011). *Patent n°8 058 584*. United States of America: United States Patent and Trademark Office.

Mohamed, M. S., Foster, A. D., Lin, J., Balint, D. S. & Dean, T. A. (2012). Investigation of deformation and failure features in hot stamping of aa6082: experimentation and modelling. *International journal of machine tools and manufacture*, 53(1), 27–38.

Mohamed, M. S. K. (2010). An investigation of hot forming quench process for AA6082 aluminium alloys.

MPDB. (1999). JAHM Software, Inc. Material Property Database) (Version 6.32) [Software]. http://www.jahm.com.

National Physical Laboratory. (2010, November, 15). Calculated Mg–Zn phase diagram [Webpage]. Consulted at http://resource.npl.co.uk/mtdata/phdiagrams/mgzn.htm.

Nemat-Nasser, S., Guo, W. & Cheng, J. (1999). Mechanical properties and deformation mechanisms of a commercially pure titanium. *Acta materialia*, 47(13), 3705–3720.

Pardee, R. J. (1987). *Publications of the national bureau of standards, 1986 catalog*. US Dept. of Commerce, National Bureau of Standards.

Pearce, R. (1968). Some aspects of anisotropic plasticity in sheet metals. *International journal of mechanical sciences*, 10(12), 995–1004.

Pellegrini, D. (2011). Study on thermal and rheological parameters of high strength steels in hot forming conditions.

Ringer, S. & Hono, K. (2000). Microstructural evolution and age hardening in aluminium alloys: atom probe field-ion microscopy and transmission electron microscopy studies. *Materials characterization*, 44(1), 101–131.

Rodriguez, P. (1984). Serrated plastic flow. *Bulletin of materials science*, 6(4), 653–663.

Sachet, J., Laval, J., Lepoutre, F. & Boccara, A. (1990). Thermal behaviour of grain boundaries in aluminium nitride ceramics. *Le journal de physique colloques*, 51(C1), C1–617.

Samekto, H. & Roll, K. (2003). Finite element analysis of superplastic forming process using LS-DYNA. 4-th european LS-DYNA user's conference. *Ulm, germany*.

Sato, Y. S., Kokawa, H., Enomoto, M. & Jogan, S. (1999). Microstructural evolution of 6063 aluminum during friction-stir welding. *Metallurgical and materials transactions A*, 30(9), 2429–2437.

Smith, D. K. (1986). International tables for crystallography; volume a-space group symmetry, brief teaching edition: Edited by T. Hahn. D. Reidel Publ. Co., 3300 AZ Dordrecht, The Netherlands (1985), viii+ 119 pp. ISBN 90-277-1964-0. Pergamon.

Soare, S., Yoon, J. W. & Cazacu, O. (2008). On the use of homogeneous polynomials to develop anisotropic yield functions with applications to sheet forming. *International journal of plasticity*, 24(6), 915–944.

Sotirov, N., Simon, P., Waltenberger, T., Uffelmann, D. & Melzer, C. (2010). Towards high strength 7xxx aluminium sheet components through warm forming. *Proceedings of the 12th international conference on aluminium alloys, Yokohama, Japan*.

Staley, J. (1974). Aging kinetics of aluminum alloy 7050. *Metallurgical transactions*, 5(4), 929–932.

US Department of Defense. (1991). *Heat Treatment of Aluminium Alloys*. MIL-H-6088G. Standardization Documents Order Desk, Building 4D, 700 Robbins Avenue, PA, 19111-5094: US Department of Defense.

Watanabe, K., Matsuda, K., Ikeno, S., Yoshida, T. & Murakami, S. (2015). Tem observation of precipitate structures in Al-Zn-Mg alloys with additions of Cu/Ag. *Archives of metallurgy and materials*, 60(2), 977–979.

Wilkes, G. (1954). *Total normal emissivities and solar absorptivities of materials*. Wright Air Development Division, Air Research and Development Command, United States Air Force.

Woodthorpe, J. & Pearce, R. (1970). The anomalous behaviour of aluminium sheet under balanced biaxial tension. *International journal of mechanical sciences*, 12(4), 341–347.

Ying, L., Gao, T., Dai, M. & Hu, P. (2017). Investigation of interfacial heat transfer mechanism for 7075-t6 aluminum alloy in hfq hot forming process. *Applied thermal engineering*, 118, 266–282.

Zhou, J., Wang, B., Lin, J. & Fu, L. (2013). Optimization of an aluminum alloy anti-collision side beam hot stamping process using a multi-objective genetic algorithm. *archives of civil and mechanical engineering*, 13(3), 401–411.